Superconducting Resonator with Composite Film and Circuit Layout Design for Quantum Information

by

Yongchao Tang

A thesis
presented to the University of Waterloo
in fulfillment of the
thesis requirement for the degree of
Doctor of Philosophy
in
Electrical and Computer Engineering (Quantum Information)

Waterloo, Ontario, Canada, 2017

Examining Committee Membership

The following served on the Examining Committee for this thesis. The decision of the Examining Committee is by majority vote.

External Examiner	NAME	Yi Zhou
	Title	Professor
Supervisor(s)	NAME	Guo-Xing Miao
	Title	Assistant Professor
Co-Supervisor(s)	NAME	David G. Cory
	Title	Professor
Internal Member	NAME	Bo Cui
	Title	Associate Professor
Internal Member	NAME	Zbigniew Wasilewski
	Title	Professor
Internal-external Member	NAME	Adam Wei Tsen
	Title	Assistant Professor

Author’s Declaration

This thesis consists of material all of which I authored or co-authored: see Statement of Contributions included in the thesis. This is a true copy of the thesis, including any required final revisions, as accepted by my examiners.

I understand that my thesis may be made electronically available to the public.

Statement of Contributions

Section 4 of Chapter 2 and Chapter 3 have been incorporated within a paper that has been published. Yong-Chao Tang, O. Benningshof, Hamid R. Mohebbi, David G. Cory, Guo-Xing Miao, Evaluation of quality factors in superconductor microresonators with proximity enhancement, in *14th IEEE International Conference on Nanotechnology*. (IEEE, Toronto, 2014), pp. 347-351, available online: http://ieeexplore.ieee.org/abstract/document/6968001/. Y-C.T. and G-X.M. proposed the materials system; H.R.M. and D.G.C. designed the device layout; Y-C.T. grew and characterized the materials, and fabricated the devices; O. Benningshof and Y-C.T. measured the Q values of resonators; Y-C.T. analyzed the data; Y-C.T., D.G.C., and G-X.M. participated in writing the manuscript.

Chapter 4 of this thesis consists of a paper that has been published. Yong-Chao Tang, Hui Zhang, Kwon Sangil, Hamid R. Mohebbi, David G. Cory, Li-Cong Peng, Lin Gu Hai-Zhong Guo, Kui-Juan Jin, Guo-Xing Miao, Superconducting Resonators Based on TiN/Tapering/NbN/Tapering/TiN Heterostructures. *Advanced Engineering Materials* **18,** 1816-1822 (2016), available online: http://onlinelibrary.wiley.com/doi/10.1002/adem.201600226/full. Y-C.T. and G-X.M. proposed the materials system; H.R.M. and D.G.C. designed the device layout; Y-C.T. grew the materials, and fabricated the devices; Y-C.T., H.Z., L-C.P., L. G., H-Z.G., K-J.J., characterized the materials. S.K. and Y-C.T. measured the Q values of resonators; Y-C.T. analyzed the data; Y-C.T., D.G.C., and G-X.M. participated in writing the manuscript.

Chapter 5 of this thesis consists of a paper that has been published. Yong-Chao Tang, Sangil Kwon, Hamid R. Mohebbi, David G. Cory, Guo-Xing Miao, phonon engineering in proximity enhanced superconductor heterostructures. *Scientific Reports* **7**, 4282 (2017), available online: https://www.nature.com/articles/s41598-017-04057-1?WT.feed_name=subjects_physics. Y-C.T. and G-X.M. proposed the materials system; H.R.M. and D.G.C. designed the device layout; Y-C.T. grew and characterized the materials, and fabricated the devices; S.K. and Y-C.T. measured the Q values of resonators; Y-C.T. analyzed the data; all authors participated in writing the manuscript.

Chapter 6 of this thesis consists of a paper that has been published. Yong-Chao Tang, Guo-Xing Miao, Robust surface code topology against sparse fabrication defects in a superconducting-qubit

array. *Physical Review A* **93**, 032322 (2016), available online: https://journals.aps.org/pra/abstract/10.1103/PhysRevA.93.032322.

Section 2 of Chapter 7 of this thesis consists of a paper that is intended to be submitted for publication. Yong-Chao Tang, Guo-Xing Miao, 2D implementation of quantum annealing algorisms for fourth order binary optimization problems. *arXiv preprint arXiv:1605.03887*, (2016).

Section 3 of Chapter 7 of this thesis consists of a paper that is intended to be submitted for publication. Yong-Chao Tang, Guo-Xing Miao, Quantum annealing against runtime errors through stabilizer codes.

Abstract

The full manipulation of a quantum system can endow us with the power of computing in exponentially increased state space without exponential growth of physical resources. High-quality, innovative superconducting films plays a key role in the next stage of development of large-scale superconducting quantum computing protected by error correction. The further development of quantum error correction theory should also be tailored to the devices' limitations brought by modern nanofabrication. Neither hardware nor software shall be absented for realizing efficient quantum information processor. In this thesis, we are dedicated to the development in the material of superconducting devices and its application in future large-scale quantum computation with error correction methods.

For the hardware, we developed composite superconducting films for resonators in the application of low-temperature pulsed-ESR for quantum information processing making use of proximity effect. The superconducting resonator is also the key element in superconducting circuits for quantum storage and quantum bus. We compared the performance of superconducting resonators made from single Nb film with those of composite films, including Nb/NbN/Nb, TiN/tapering/NbN/tapering/TiN, and Al/Nb/Al. We found that the quality factor of resonators from Al/Nb/Al surpasses the previous best results from single Nb film under 0.35 T magnetic field. A formula was established for evaluating the surface impedance of composite superconducting film. It has been proved that adjusting phonon density of states in superconducting films can tailor the recombination time of Cooper pairs in thin films and hence affect the coherence time of qubits and Q values of resonators. For the software, we improved the surface code theory to make it resistant to sparse fabrication defects. A physically faulted qubit can be replaced with a working physical qubit near the defective one. Thereby sparse fabrication errors can be collected into one sacrificial layer and isolated from the working layers by turning off their controllable couplers. We proposed a two-dimensional quantum annealing architecture to solve the 4^{th} order binary optimization problem by encoding four-qubit interactions within the coupled local fields acting on a set of physical qubits. We also designed a layout to implement quantum annealing with error correction through stabilizer codes. The stabilizers are realized with weak measurements for real-time, in-run monitoring of spins, to minimize or control the back-action.

Acknowledgements

First and foremost, I would like to express my sincere gratitude to my advisors, Professor Guo-Xing Miao and Professor David G. Cory, for their constant support throughout the years of my Ph.D. studies. It is indeed my great honor and privilege to be their student. I deeply appreciate all of their guidance and discussions, which tremendously motivated me to do the best that I could in the world of research.

I am also grateful to have Prof. Jonathan Baugh, Prof. Bo Cui, and Prof. Zbigniew Wasilewski as members of my Ph.D. committee, all of whom contributed insightful feedback to my research.

Also, I am grateful to be a part of the wonderful research team at the Institute for Quantum Computing (IQC). I would like to thank our previous and current lab members, Dr. Qiang Li, Yuantao Ji, Zhiwei Gao, Dr. Hui Zhang, Lin Li, Dr. Yin Liu, Xiaodong Ma, for their tremendous help in my research projects. My sincere gratitude also goes to Dr. Sangil Kwon, for his help in the measurements using dilution fridge. I would like to thank Dr. Hamid R. Mohebbi and Troy Borneman. The discussions with them were very helpful for my project about superconducting resonators. I would like to thank Dr. Deler Langenberg and Alex Mitrovic, for their hardworking on maintaining Omicron systems and in the machine shop. I would also like to thank QNC fab staff, including Vito Logiudice, Brian Goddard, Nathan Nelson-Fitzpatrick, Rodello Salandanan and Matt Scott, for their help and advice on my fabrication processes.

Yongchao Tang, Waterloo, MAY 2017.

Dedication

I dedicate my dissertation work to my family and many friends. No words can fully express how grateful I am to you, my dear parents, for constantly supporting me throughout this special research journey. You set a role model for me to follow, and your love and spiritual support are my driving force to work hard. A special feeling of gratitude to my wife, Shu Wang whose words of encouragement and push for tenacity ring in my ears.

Table of Contents

List of Figures

List of Tables

Chapter 1
Introduction

1.1 Motivation

The full manipulation of a quantum system can endow us with the power of computing in exponentially increased state space without exponential growth of physical resources. While quantum computing could bring us a potential revolution for the computation in the future, it does require strict abilities to control quantum system. Since Feynman proposed the idea of computing with a quantum system, quantum computing has been developed for almost three decades. Spin resonance, ion trap, quantum dot, and superconducting circuits all show their advantages over controlling microscopic quantum system and their potentials in quantum computing. With tremendous efforts over the last few decades, the size of the quantum system which researchers can achieve has also grown from one or two qubits to dozens of qubits. Some of the most promising candidates for realizing scalable quantum computation is based on superconducting devices [1-4]. The developments in superconducting devices and layout design have played important roles in the future application of large-scale quantum computation with universal quantum circuit model and quantum optimization method.

Because of their extremely low loss in microwave frequencies, superconducting resonators are of vital importance for quantum computation [4, 5], manipulating multiple remote qubits [6, 7], storing arbitrary quantum states [8], and implementing quantum algorithm [9, 10]. They are also widely used in studying the strong-coupling regime of cavity quantum electrodynamics in electrical circuits [4, 11], microwave kinetic inductance photon detectors (MKID) [12, 13], probing the microscopic mechanism of two-level systems [14], and manipulation of ensemble spin systems [15]. The microwave resonator is a device in which microwave can oscillate in resonance at some frequency with greater amplitudes than at others. The transmitted microwaves at resonant frequency will bounce back and forth between the sides of resonators and reinforce each other to create a pattern of standing microwaves in the resonator. The resonant frequency at which the device will exhibit resonant behavior is also called normal mode. A transmission line resonator is composed of a transmission line segment. A microwave transmission line is the structure that

allows the transmission of microwaves. Sudden changes to the impedance in a microwave transmission line causes the reflection of transmitted signal. The impedance changes can be resulted from open and short ends of the structure. If a transmission line has two such open or short ends, standing waves may be evoked in the device between two ends. Therefore, the transmission line segment can act as a one-dimensional resonator. The resonance frequency is determined by many factors such as the length of segment and the effective inductance and capacitance met by microwaves. Most commonly used planar resonators in quantum information processing are employed for superconducting coplanar and microstrip transmission lines. The planar superconducting resonators are widely used devices in superconducting circuits due to their compact size and much lower losses than normal conductor resonators. The quality factor of a resonator is a dimensionless parameter which describes how fast the energy stored in a resonator will decay. Because the quality factor Q is defined as $Q \propto X_S / R_S$ ($\mathrm{R_s}$ and $\mathrm{X_s}$ are surface resistance and the corresponding reactance), studying surface impedance for resonators plays a major role in the development of future quantum technology.

The spin ensemble is an important physical system for future quantum computing because of its longer coherence time than superconducting qubits. Pulsed electron spin resonance (pulsed-ESR) spectroscopy [16, 17] proceeds by probing an ensemble of spins coupled to a microwave resonator of frequency ω_0 and quality factor Q with sequences of microwave pulses which can perform successive spin rotations. The readout information about the number and properties of paramagnetic species is contained within the amplitude and shape of a microwave signal called a spin-echo. The emission of spin-echo signal is triggered by sequences of microwave pulses. The sensitivity of pulsed-ESR method is conveniently quantified by the minimal number of detectable spins N_{min}. Conventional pulsed-ESR method use 3-D resonators with moderate quality factors in which spins are only weakly coupled to the microwave photons, and therefore $N_{min} \approx 1\times10^{13}$ spins are obtained at $T = 300$ K and X-band frequencies ($\omega_0 / 2\pi \approx 9-10$ GHz). The minimal number of detectable spins depends on the photon frequency ν according to:

$$N_{\min} = \frac{k_1 V}{Q_0 k_f \nu^2 P^{1/2}}, \tag{1.1}$$

where k_1 is a constant, V is the sample's volume, Q_0 is the unloaded quality factor of the microwave cavity (sample chamber), k_f is the cavity filling coefficient, and P is the microwave power in the spectrometer cavity. Eq. (1.1) shows that smaller mode volume can increase k_f which further leads to smaller sample's volume V. Hence, N_{min} is decreased as we expect. Planar superconducting transmission line resonator can provide much smaller mode volume than a 3-D resonator, resulting in larger spin-microwave coupling [18, 19]. Combined with operation at $T = 4$ K and the use of low-noise cryogenic amplifiers and superconducting high-Q thin-film resonators, sensitivities up to $N_{min} \approx 1\times10^7$ spins have been reported [20-22]. Further improvements in the sensitivity of pulsed-ESR spectroscopy can be achieved by cooling the sample and resonator down to millikelvin temperatures that satisfy $T \ll \hbar\omega_0 / k_B$ at X-band frequencies. As a result, both the spins and the microwave field reach their quantum ground state, which is the optimal situation for magnetic resonance because the spins are fully polarized and thermal noise is suppressed. For the bismuth-doped ^{28}Si (^{28}Si:Bi) sample with Al microwave resonator with a loaded quality factor $Q = 3\times10^5$ for resonator frequency $\omega_0 / 2\pi = 7.24$ GHz, the sensitivity of 1.7×10^3 spins/Hz$^{1/2}$ given the 1 Hz repetition rate has been obtained [23]. The required external magnetic field is only around 10 mT corresponding to the resonant frequency of around 7.4 GHz between the ground state and the low excited states of the electron-nuclear low energy states in the ^{28}Si:Bi system.

Our ultimate goal is to make use of low loss superconductor resonators in pulsed-ESR, in order to implement scalable quantum information processor with hybrid nuclear-electron spins [24], as shown in Figure 1.1. Pulsed-ESR spectroscopy can be used for quantum computing [25]. A distributed, multimode scheme has been proposed for scalable QIP which can be applied to hybrid solid-state nuclear-electronic spin system [24, 26-31]. The requirement for such a scheme is that it needs to define an array of disjoint quantum processors with communication between local processors provided by a coupling between nodes. This requirement can be satisfied by the hybrid solid-state nuclear-electronic spin system with magnetic resonance technique. Thus, the hybrid system with magnetic resonance is applicable for scalable spin quantum computer in the near future.

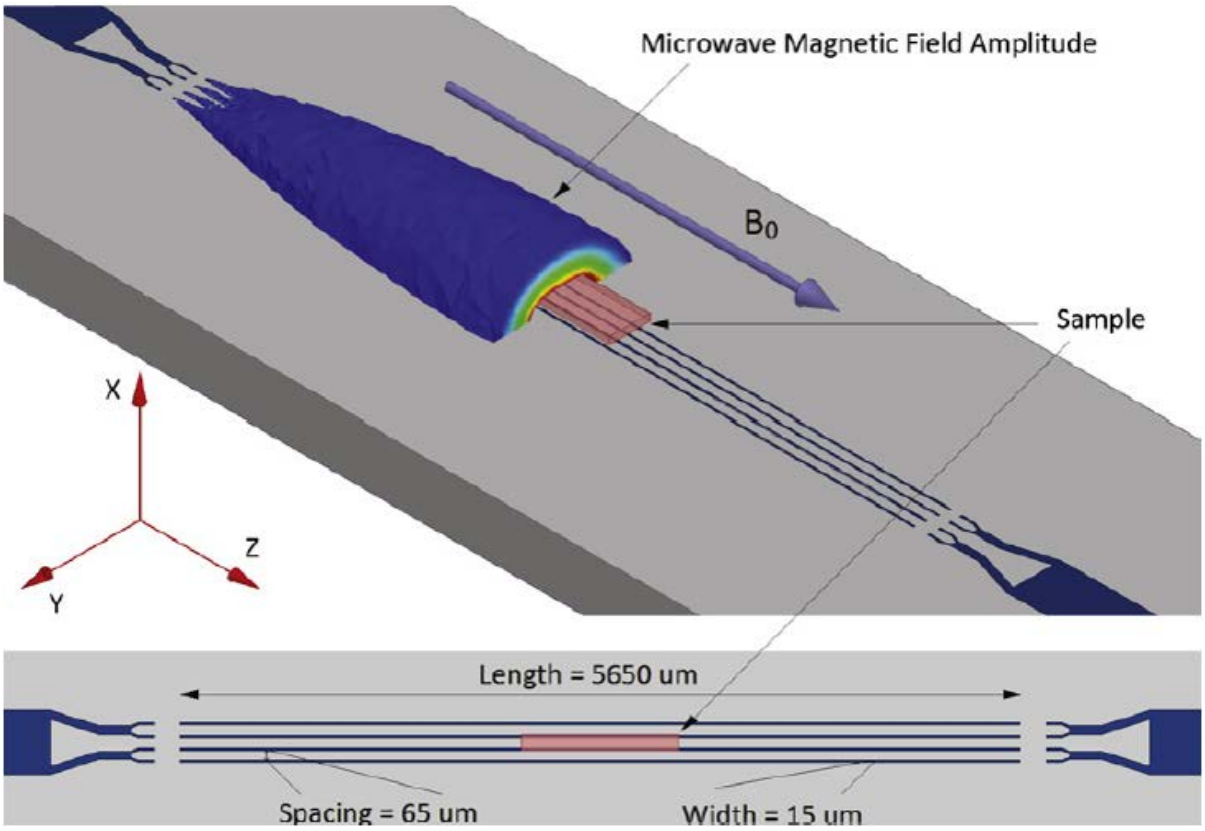

Figure 1.1: Superconducting microstrip resonator for pulsed ESR of thin films [22]

Low microwave loss, also manifested as a high resonance quality factor (Q), is essential for high-sensitivity measurement and enables cavity cooling of ensemble spin systems [32]. Eq. (1.1) shows that larger Q value will also decrease N_{min}. For our targeted pulsed-ESR experiments, the required magnetic field is around 0.35 T, corresponding to a g=2 electron resonant frequency of 9.8 GHz, and the field drastically reduces the quality factor of superconducting resonators. Thus, a higher Q of a resonator under such a strong magnetic field can be reached, better performance for quantum information processing is desired. Q will be limited by magnetic flux trapped in thin films in the form of vortices [33] which physically oscillate in microwave driving currents and induce losses. Vortex starts to be generated in aluminum (Al) thin film when a magnetic field is greater than a threshold B_{th} (for example, $B_{th} = 0.3$ Gauss for 150 nm Al [34]). One requirement is a small reduced-field, the ratio of the applied magnetic field to the critical field of the superconductor

($H/H_{C2}(0) \leq 0.1$). With the desired external magnetic field of 0.35T, there are only a few superconductors, such as niobium (Nb), that can be used to fabricate a high-Q resonator for low temperature pulsed ESR applications. The bulk critical field of Nb ($H_{C2}(0) \sim 0.5$ T and $H_{C2}(4.2) \sim 0.3$ T) [35] is however not sufficiently large compared to the applied magnetic field B_0 (~0.35 T). Though the critical field can be enhanced by using thin films [36] with the film plane kept parallel to the external magnetic field B_0 [37], we are seeking more options to increase the Q values of superconductors under strong magnetic field (~0.35 T). In this thesis, we explored several ways to improve the performance of superconducting planar resonators for pulsed-ESR which can withstand high magnetic field.

From the material aspects, there are two important considerations for improving the performance of a resonator placed in a magnetic field: the choice of materials and the quality of materials. The former depends on the intrinsic properties of the superconductor materials. The most popular material for superconducting resonators are aluminum (Al) [38], niobium (Nb) [39, 40], tantalum (Ta) [41], rhenium (Re) [42] and titanium nitride (TiN) [43] which all have low internal loss (δ_i), and therefore high internal quality factors ($Q_i = 1/\delta_i$) under zero magnetic field [44]. Nevertheless, a large magnetic field (~0.35 T) required by pulsed-ESR may destroy the superconducting states of most superconductors. Another important factor affecting the performance of a resonator is the material quality. Epitaxial films, free from structural defects, with smooth and clean surfaces/interfaces, are most desired for the application of superconducting resonators [44].

Furthermore, we can make use of the proximity effect to enhance the upper critical field of superconductors. In a trilayer structure, the core layer can improve the critical field and critical temperature of the coating layers through the proximity effect when both parameters of the core layer are significantly higher. Due to the skin effect of microwave propagation, the amplitude of the electromagnetic waves will decay exponentially inside the superconductors with a length scale of the penetration depth. So the main contribution to the microwave losses comes from the surfaces of the superconducting films as the significant amount of currents flow here [39]. Proximity effect will induce higher critical field, thereby suppressing the generation of vortices in the coating layers and reduce losses on the surfaces; also, higher induced critical temperatures exponentially reduce the population of quasiparticles, which also reduces losses in these layers.

Besides the improvement of superconducting devices, layout design is also important for large-scale quantum computation. Two computing schemes are the current research interests: implementing quantum circuit model with high-threshold error correction methods such as surface codes, and quantum optimization through the annealing method. Surface code error correction tops other error correction methods by its experimentally accessible per step error threshold. While it is successfully demonstrated in experiments, it still requires thousands of physical qubits for an errorless logical qubit. Such a large qubits array will inevitably have some fabrication faults, which the original surface code theory cannot deal with. The other promising application of large scale computation with the quantum system is quantum optimization. The goal of quantum optimization is to find a solution to some optimization problem by using quantum adiabatic evolution. Two of the biggest problems facing the development of quantum optimization is how to express many-body product terms beyond two-body interactions and how to implement error correction in such a computing scheme.

1.2 Hybrid nuclear-electronic system for electron spin resonance

The magnetic resonance is a well-developed technique for quantum information processing (QIP). The nuclear magnetic resonance (NMR) using the nuclear spins of an ensemble of molecules in solution at room temperature was one of the first experimental schemes for QIP [45, 46]. The liquid-state NMR has some cons such as small thermal spin polarization due to the small amount of energy separating two computational qubit states [47], decreased detected signals [48] and vanishing entanglement of system [49] when the number of qubits in the system is increased. Cory et al. outlined many advantages of solid-state NMR to liquid-state NMR [50]. The solid-state NMR QIP have: (a) stronger coupling between spins, (b) longer coherence times, (c) higher susceptibility to polarization and (d) ability to dynamically reset the qubits.

Solid-state electron magnetic resonance (ESR) can also be used for QIP where the qubit is associated with the electron spin. Solid-state nuclear and electron spin-based QIP have their own pros and cons. Nuclear spin has longer coherence times than electron spin, but it is manipulated and measured much more slowly. On the contrary, the electron spin interacts more strongly with its environment than nuclear spin. Thus, the electron spin can be measured and manipulated at a rapid rate, while it will lose its coherence very quickly. It is straightforward to propose a hybrid

solid-state nuclear-electronic spin system for QIP. The nuclear spin is used as storage while the electron spin is used for manipulation and measurement.

The most common nuclear-electronic spin systems for QIP with magnetic resonance are group V doped silicon such as phosphorus-doped silicon (Si:P) and bismuth-doped silicon (Si:Bi), and endohedral fullerenes on silicon surfaces with a scanning-tunnel-microscope tip [51].

The best-known hybrid nuclear-electronic spin system with phosphorus-doped silicon (Si:P) for QIP was proposed by Bruce Kane in 1998 [27]. The phosphorus is used as a localized donor nuclear spin which is coupled to a localized donor electron spin by the hyperfine interaction. Each localized nuclear-electronic spin system can be considered as two coupled qubits. In 2003, Schofield *et al.* showed the controlled incorporation of P dopant atoms in Si(001) by using STM H lithography [52]. In the same year, Tyryshkin *et al.* presented spin echo measurements of isotopically purified ^{28}Si:P which showed transverse relaxation times 14 ms at 7 K [53]. Tyryshkin *et al.* measured the spin coherence in Si:P in 2006 [54]. They applied bang-bang decoupling of ^{31}P nuclear spin using controlled flips of electron spin. Both electrons bound to donors and the donor nuclei exhibited low decoherence under the right circumstances. Morton *et al.* demonstrated the coherent transfer of a superposition state in an electron-spin qubit to a nuclear-spin qubit in 2008 [55]. They applied a combination of microwave and radio-frequency pulses to ^{31}P donors in an isotopically pure ^{28}Si crystal using pulsed electron paramagnetic resonance (EPR). In 2009, McCamey *et al.* demonstrated a method for obtaining more than 68% negative nuclear polarization of phosphorus donors in silicon by white light irradiation [56]. In 2010, Morley *et al.* showed that bismuth in silicon (Si:Bi) has electron spin coherence times at least as long as Si:P at comparable temperatures and ^{29}Si concentrations [57]. In 2011, Simmons *et al.* reported the on-demand generation of entanglement between and ensemble of electron and nuclear spins in isotopically engineered Si:P [58]. They combined high-field, low-temperature ESR with hyperpolarization of the ^{31}P nuclear spin to obtain an initial state of sufficient purity to create a non-classical state. In 2013, Morley *et al.* investigated 'hybrid nuclear-electronic' qubits using Si:Bi with pulsed magnetic resonance technique [59]. The large nuclear spin and hyperfine coupling of Si:Bi brought about the entanglement of the nuclear and electronic spin degrees of freedom in the magnetic field region smaller than 0.6 T.

The concept of quantum computation using endohedral fullerenes as spin-qubits were first proposed by Harneit [60], Suter and Lim [61], and Twamley [29]. Each molecule spin site consists of a nuclear spin coupled via a Hyperfine interaction to an electron spin. The quantum information is encoded on the nuclear spins while using the electron spins as a local bus. A thorough introduction on the synthesis of endohedral fullerenes and the concepts of spin quantum computing can be referred to the book edited by Alexey A. Popov [62].

1.3 Thesis outline

In Chapter 1, the motivation for the overall research projects is described. Chapter 2 presents a brief introduction to the theories of superconductors and the development of the theories of proximity effect. The way to evaluate the surface impedance for composite superconducting films through extended Zimmermann formula is also included. In Chapter 3, we compare Nb/NbN/Nb trilayer structures with Nb single layer structures for their performance as superconductor resonators. Chapter 4 covers the performance of the resonators with TiN/tapering/NbN/tapering/TiN on c-cut sapphire substrates grown by reactive magnetron sputtering. Detailed film characterizations with different methods are included. A gradually-changed tapering layer which eliminates the distinct boundaries between TiN and NbN is adopted to make the wavefunction change smoothly between NbN and TiN. Chapter 5 examines a model system of proximity-enhanced Al/Nb/Al heterostructures, and we consider the size effect of the ultrathin Al cladding layers. The two Al layers are thin enough such that the size effect of thin films becomes appreciable. The measured Q in 5/50/5 nm and 10/50/10 nm Al/Nb/Al heterostructures are compared. In Chapter 6, we propose a defect-tolerant surface code topology which is resistant to sparse fabrication defects. The circuit layout is a two-dimensional array of unit cells which is equivalent to a disk folded into N layers. Chapter 7 demonstrates a two-dimensional quantum annealing architecture to solve the 4^{th} order binary optimization problem by encoding four-qubit interactions within the coupled local fields acting on a set of physical qubits. It also covers a method to implement quantum annealing with error correction through stabilizer codes. The stabilizers are realized with weak measurements for real-time, in-run monitoring of spins, to minimize or control the back-action.

Chapter 2
Theoretical concepts

2.1 Introduction of superconductor theory

The Bardeen-Cooper-Schrieffer (BCS) theory [63, 64] has become the essential physical theory that clarifies how a coherent superconducting state can be formed by the condensation of the Cooper pairs. As a self-consistent, mean field treatment, it applies only to clean and homogeneous systems in three dimensions. To account for inhomogeneous systems, such as multilayer systems of superconductor-insulators, Bogoliubov [65], and de-Gennes [66], independently derived a system of coupled equations between electrons and holes that give the solutions for the fermionic quasiparticles above the superconducting condensate. The energies of the quasiparticles are separated from the condensate by Δ which is the superconducting energy gap.

Before the BCS microscopic theory, Ginzburg and Landau had developed a theory to explain superconductivity based on the Landau theory of second order phase transitions. The result is the celebrated Ginzburg–Landau (GL) theory of superconductivity [67]. The complex order parameter in the system of superconductivity is represented by the system's free energy. Later, this theory was rigorously derived from the microscopic BCS theory near the phase transition temperature of the system T_c by Gorkov [68].

Gorkov developed a powerful method to study the superconductivity by writing down a closed set of equations of motion with the Green's functions [69]. Green functions carry the information of the transport probabilities of single particles. They describe how particles propagate through the system under the consideration of all kinds of interactions. The solutions to the set of equations yield all the results of the BCS theory. Furthermore, this methodology can be readily used to describe not only dirty systems with impurities, but also deal with dynamics of non-linearities. Hence, type-II superconductors can be studied.

Although Gorkov Green's functions can be used in many cases that BCS theory does not apply to, the functions are hard to solve. Eilenberger [70], as well as Larkin and Ovchinnikov [71],

independently applied the quasiclassical approximation to the Gorkov equations and developed an energy-integrated version of the Gorkov Green's functions. A method to take into account the interaction between electrons and random impurities has been developed by Abrikosov and Gor'kov [72]. It has been considered that physical properties of superconductors incorporating a significant amount of random impurities can be obtained by averaging over realizations of the disordered impurity potentials.

2.2 Usadel equation

Usadel rewrote the Eilenberger equations as a fully isotropic one by averaging over momentum directions [73]. The Usadel diffusion equation is much simpler than the original Eilenberger equations and amenable to numerical implementations, enabling realistic experimental geometries and situations to be analyzed.

Eilenberger introduces the functions $g(\omega,\vec{r},\vec{v})$ and $f(\omega,\vec{r},\vec{v})$ which are closely related to the Green's functions of a superconductor [70]. These two quantities are the impurity-averaged Green's functions integrated over the energy variable. Usadel considers only the superconductors with spherical Fermi surfaces. $\vec{v}$ denotes the Fermi velocity. It is assumed that $\omega=(2n+1)\pi T>0$. For a dirty superconductor, one expects that the functions $g(\omega,\vec{r},\vec{v})$ and $f(\omega,\vec{r},\vec{v})$ become nearly isotropic on $\vec{v}$ and can be expanded as:

$$f(\omega,\vec{r},\vec{v})=F(\omega,\vec{r})+\hat{v}\cdot\vec{F}(\omega,\vec{r}), \tag{2.1}$$

$$g(\omega,\vec{r},\vec{v})=G(\omega,\vec{r})+\hat{v}\cdot\vec{G}(\omega,\vec{r}), \tag{2.2}$$

where Usadel neglects higher order terms, and $\hat{v}=\vec{v}/|\vec{v}|$. $G(\omega,\vec{r})$ is defined by

$$G(\omega,\vec{r})=\sqrt{1-|F(\omega,\vec{r})|^2}\,. \tag{2.3}$$

By eliminating the currents $\vec{F}(\omega,\vec{r})$, $\vec{G}(\omega,\vec{r})$, and keeping the densities $F(\omega,\vec{r})$, $G(\omega,\vec{r})$, De Gennes's diffusion equation is generalized by Usadel to arbitrary values of Δ which is only valid in the dirty limit:

$$2\omega F(\omega,\vec{r})-D\hat{\partial}\left[G(\omega,\vec{r})\hat{\partial}F(\omega,\vec{r})+\frac{1}{2}\frac{F(\omega,\vec{r})}{G(\omega,\vec{r})}\vec{\partial}|F(\omega,\vec{r})|^2\right]=2\Delta(\vec{r})G(\omega,\vec{r}), \tag{2.4}$$

where D is defined as the diffusion coefficient, $\Delta(\vec{r})$ is an order parameter. Hence, the self-consistency conditions in terms of $F(\omega,\vec{r})$ for the order parameter Δ is,

$$\Delta(\vec{r})\ln\frac{T}{T_C}+2\pi T\sum_{\omega>0}\left[\frac{\Delta(\vec{r})}{\omega}-F(\omega,\vec{r})\right]=0. \tag{2.5}$$

For superconducting multilayer films, it is considered that the i_{th} superconducting film S_i in which the dirty limit condition $l_{S_i}\le\xi_{S_i}$ is fulfilled. Here l_{S_i} is the electronic mean free path. The coherence length ξ_{S_i} is related to the diffusion coefficient D_{S_i} by the relation $\xi_{S_i}=\sqrt{D_{S_i}/2\pi T_{C,S_i}}$. The x-axis is defined as perpendicular to the film surface. Golubov *et al.* rewrite the Usadel equations as follows [74]:

$$\Phi_{S_i}=\Delta_{S_i}+(\xi^*_{S_i})^2\frac{\pi T_{C_i}}{\omega G_{S_i}}[G^2_{S_i}\Phi'_{S_i}]', \tag{2.6}$$

$$\Delta_{S_i}\ln(T/T_{C_i})+2\pi T\sum_{\omega>0}\left[(\Delta_{S_i}-\Phi_{S_i}G_{S_i})/\omega\right]=0, \tag{2.7}$$

where $G_{S_i}=\omega/(\omega^2+\Phi^2_{S_i})^{1/2}$. Also, $\Phi_{S_i}=\omega F_{S_i}/G_{S_i}$, $F_{S_i}=\Phi_{S_i}/(\omega^2+\Phi^2_{S_i})^{1/2}$. Δ_{S_i} is the order parameter for the i_{th} superconducting layer. ω is the Matsubara frequency [75], $\omega_n=\pi T(2n+1)$ $(n=0,1,2,\ldots)$, and the prime denotes differentiation with respect to the coordinate x. Let $G_{S_i}=\cos\theta_{S_i}(x)$ and $F_{S_i}=\sin\theta_{S_i}(x)$, Eq. (2.6) and (2.7) can be rewritten as [76]:

$$\xi^2_{S_i}\theta''_{S_i}(x)+i\varepsilon\sin\theta_{S_i}(x)+\Delta_{S_i}(x)\cos\theta_{S_i}(x)=0, \tag{2.8}$$

$$\Delta_{S_i}(s)\ln\frac{T}{T_{C,S_i}}+2\frac{T}{T_{C,S_i}}\sum_{\omega_n}\left[\frac{\Delta_{S_i}(x)}{\omega_n}-\sin\theta_{S_i}(i\omega_n,x)\right]=0. \tag{2.9}$$

Here, the function θ_{S_i} has been introduced as a unique Green's function which defines the quasiparticle density of states N_{S_i}:

$$N_{S_i}(\varepsilon,x)/N_{S_i}(0)=\mathrm{Re}\left[\cos\theta_{S_i}(\varepsilon,x)\right], \tag{2.10}$$

where $N_{S_i}(0)$ is the electronic density of states in the normal state at the Fermi surface. By using the appropriate boundary conditions, the Usadel equations Eq. (2.8) and (2.9) can be solved in each layer for a multi-layer structure.

2.3 Proximity effect

2.3.1 Development of theories for proximity effect

Superconducting proximity effect refers to the situation that when a superconductor is placed in contact with a normal metal (or another kind of superconductor with lower critical temperature), weak superconductivity is observed in the normal material over a certain distances or the critical temperature of one layer of superconductor is increased while that of another layer is suppressed. The proximity effect occurs at the interface between a superconductor and normal metal or between two superconductors with different critical temperatures. The proximity effect is first discovered by R. Holm and W. Meissner in 1932, but it is not understood as the proximity effect until R. Holm's work in 1960 [77].

The electrons have different electron orders in normal conductors and superconductors. In a superconductor, there exist the well-known Cooper pairs of electrons which are called superconductor order. Moreover, the energy of electrons in a normal conductor are filled up to the Fermi level without a gap, which is referred to another electron order. The reason why proximity effect happens is that the wave function of electrons at the interface between two layers of material cannot change abruptly because of the non-locality of the electrons in materials. The Cooper pairs in the superconducting film are carried to the normal conductor over a certain distance (which is called the coherence length) and then are destroyed by scattering events. In contrary, the normal electrons in one side can travel into the superconductor and find other electrons to be paired. Therefore, the gap energy of the superconductor is suppressed near the interface.

Since the discovery of the superconducting proximity effect, the corresponding theories for the transport properties of superconductors have been attracted with intensive interest. Several kinds of theories are summarized in Figure 2.1.

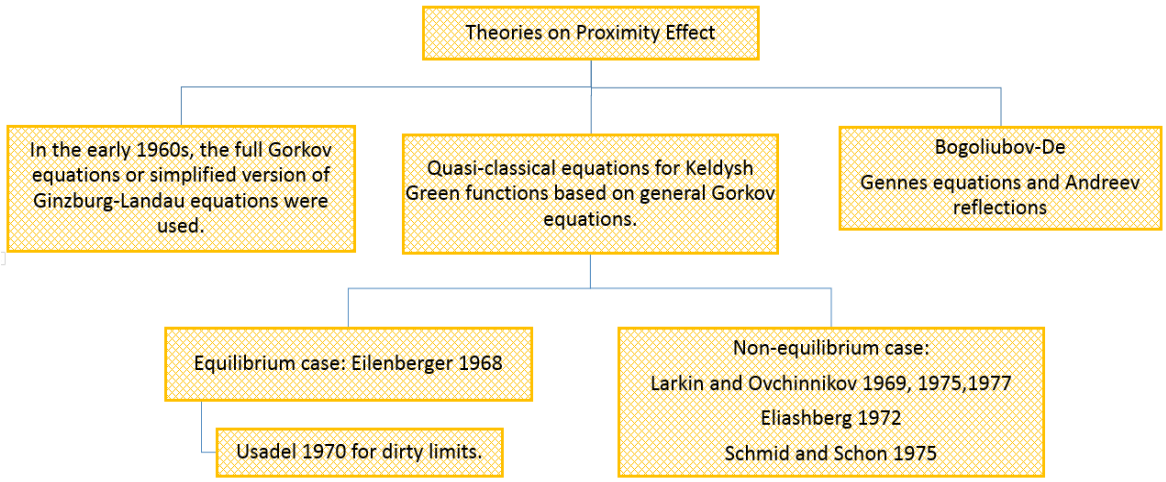

Figure 2.1: Three main methods that can be applied to calculate the properties of proximity effects. Each reference has been listed in the context.

First, in the early 1960s, the proximity effect was analyzed with the full Gor'kov equations or simplified version of Ginzburg-Landau first equation [78] which is only valid close to critical temperature.

Second, quasi-classical equations which are supplemented by suitable boundary conditions were developed with Keldysh Green functions based on Gor'kov equations [79, 80]. Of which, the stationary and equilibrium case was first derived by Eilenberger [70] in 1968. In 1970, Usadel simplified the equations of Eilenberger further [73] by assuming that the system is dirty and impurity-averaged Green's functions can be defined; this approach came to its full maturity in the early 1970s by considering the non-equilibrium cases. Many people had contributed much to its progress, including Larkin and Ovchinnikov [71, 81, 82], Eliashberg [83], and Schmid *et al.* [84].

Although many experimental problems can be studied with the help of the quasi-classical equations, some problems, in particular, those where ballistic electron transport can be assumed, can be understood more readily by using the Bogoliubov-De Gennes equations and using the concept of Andreev reflection [85]. That is the third theory on the proximity effect focusing on the Andreev reflections perspective [86]. The understanding of the proximity effect is based on the

following aspects. Andreev reflection is known to occur at the boundary between a superconductor and a normal metal. During the reflection process, electrons moving towards the interface above the Fermi level in the normal metal are converted into holes below the Fermi level and reflected backward, while a Cooper pair is formed inside the superconductor. This is one of the critical stages in the proximity effect and describes how the two electronic reservoirs are exchanging at the boundary itself. Another stage in the process of Andreev reflection is the electron-hole pair loses its correlated properties in the normal metal. The electron and the hole form phase-conjugated pairs, a property which will be lost at a certain distance from the interface. Therefore, the proximity effect is understood as such a process that the incident electrons propagate coherently and how this coherence is lost due to dephasing processes in the normal metal.

2.3.2 Proximity effect in S_1/S_2

Consider a simple case of two superconductors [78]. The two kinds of superconductors with slightly different critical temperatures (T_{cn} and T_{cs}) are placed in good contact. We let $T_{cs} > T_{cn}$, $T_{cs} - T_{cn} \ll T_{cn}$, and then one of the layers with the critical temperature T_{cn} is in the normal state when the temperature is at $T_{cn} < T < T_{cs}$. The flat interface coincides with the plane $x = 0$, and therefore we do not consider the inelastic scattering due to the rough interface. The superconductor occupies the semi-space $x > 0$, and the normal metal is at $x < 0$.

The order parameter in the S region $(x > 0)$ can be calculated by the first GL equation:

$$-\xi^2 (\frac{d\psi}{dx})^2 - \psi^2 + \frac{1}{2}\psi^4 = C, \tag{2.11}$$

where C is the integration constant, ξ is a temperature dependent parameter that $\xi^2 = \hbar^2 / (4m|\alpha|)$ ($\hbar$ is the reduced Plank constant, m is the mass of electron, α is the phenomenological expansion coefficient in GL equation which is characteristics of the material), and ψ is the superconductor order in GL equation. Since at $x \to \inf$ we have $(d\psi / dx) \to 0$, and $\psi \to 1$ on the assumption that the two superconductors are both semi-infinite, the integration constant is $C = -1/2$. Substituting this into Eq. (2.11), and carrying out the integration, the result is:

$$\psi = \tanh[(x - x_0)/\sqrt{2}\xi]. \tag{2.12}$$

Here x_0 is the integration constant to be decided from the boundary condition at $x = 0$. In this case, there is:

$$\frac{1}{\psi}\frac{d\psi}{dx} = \frac{1}{b}. \tag{2.13}$$

The value of *b* can be calculated with the microscopic theory. Its geometrical significance is shown in Figure 2.2.

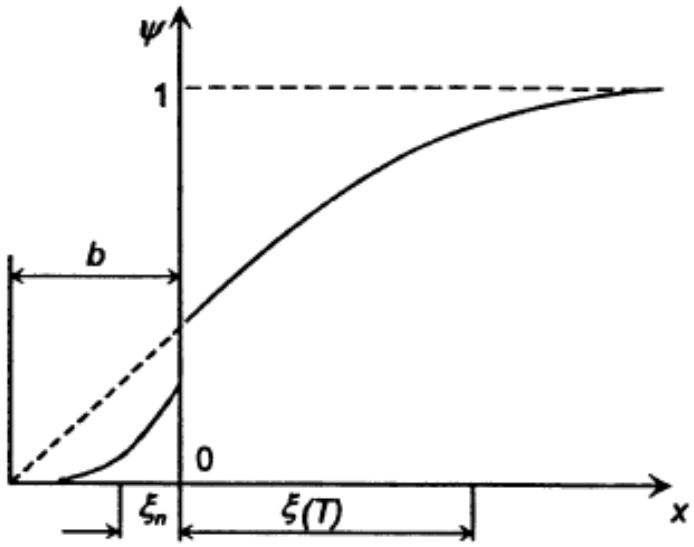

Figure 2.2: Order parameter $\psi(x)$ near the interface between a superconductor (x > 0) and a normal metal (x < 0) [78].

After Eq. (2.12) is substituted into Eq. (2.13), we find the relation between the integration constant x_0 and b:

$$-\sinh(\sqrt{2}\frac{x_0}{\xi}) = \sqrt{2}\frac{b}{\xi}. \tag{2.14}$$

The order parameter ψ in the normal region (x < 0) can also be studied by the first GL equation (see, for example, [87]). The expansion parameter $\alpha_n \propto (T - T_{cn})$ so that $\alpha_n < 0$ at $T < T_{cn}$ and $\alpha > 0$ at $T > T_{cn}$. Hence, for the N region, the first GL equation subject to the condition $T - T_{cn} \ll T_{cn}$ becomes:

$$-\xi_n^2 (\frac{d^2\psi}{dx^2}) + \psi + \psi^3 = 0, \tag{2.15}$$

where $\xi_n^2 = \hbar^2 / 4m\alpha_n$. The order parameter in the normal region is small $(\psi \ll 1)$. Therefore, we neglect the cubic term of ψ:

$$-\xi_n^2 (\frac{d^2\psi}{dx^2}) + \psi = 0. \tag{2.16}$$

Subject to the condition $\psi \to 0$ at $x \to \inf$, the result is:

$$\psi = \psi_0 \exp(-|x|/\xi_n). \tag{2.17}$$

From Eq. (2.17), the order parameter goes into the normal metal region over the depth ξ_n while decaying exponentially over this distance. Since T_{cn} and T_{cs} are close to each other, ψ and $d\psi / dx$ can be considered continuous at the two layers' interface. Then, we have $b = \xi_n$.

2.4 Evaluation of surface impedance for composite superconducting films

2.4.1 Quality factors obtained from EM simulators

The microwave loss of superconducting resonators or transmission lines can be explained by resistive loss from surface impedance [88]. Surface impedance reveals the input impedance per unit area of the whole structure toward the direction of wave propagation. The quality factor is defined as $Q \propto X_S / R_S$ (X_S and R_S are the total reactance and the resistive component of the surface impedance, respectively). However, this definition does not take into account many factors such as structure, lead, and parasitic coupling. Therefore, the best way to obtain the theoretical quality factor is to use the commercial electromagnetic simulator. Two frequently-used software are ANSYS HFSS and Sonnet Software. Using these kinds of simulators, we can extract the scattering matrix from the model with specific excitation which is set to be close the real experiments. The final results file is exported with the extension "s2p", which is just same as the

output file in our experiments with Agilent Technologies N5230A (Now is the Keysight Technologies). Then using the equivalent network in [89] for the transmission type measurement of the Q factor, we can get the loaded and unloaded quality factors from the simulation results.

2.4.2 Cascade model for surface impedance of trilayer structure

Because the field analysis of parallel propagation of a wave along the conductor yields the same solutions and surface impedance as that of the normal incidence scenario [90], transmission lines where the electric field travels along it can be modeled as that a TEM wave is normally incident upon the conductor. This applies to a single layer and trilayer structures. Therefore, the surface impedance of the microstrip superconducting resonator is the same as that of the perpendicular incidence scenario. The surface impedance Z_S of single superconducting layer with thickness d is given by

$$\begin{aligned} Z_S(\omega) &= \frac{k}{\sigma_{sc}}\coth(kd) = R_S + jX_S, \\ k &= \frac{1+j}{\delta}, \quad \delta = \sqrt{\frac{2}{\omega\mu_0\sigma_{sc}}}, \end{aligned} \tag{2.18}$$

where ω and μ_0 are the circular frequency and the permeability of vacuum, respectively.

In the case of multilayers, the structure can be treated as the cascade of many single-layer films. Therefore, the surface impedance Z_m for the m_{th} superconducting layer after $(m-1)_{\text{th}}$ layer can be evaluated through [91]:

$$Z_m = \frac{\gamma_m}{\sigma_m}\frac{e^{\gamma_m t_m} + \frac{\sigma_m Z_{m-1} - \gamma_m}{\sigma_m Z_{m-1} + \gamma_m} e^{-\gamma_m t_m}}{e^{\gamma_m t_m} - \frac{\sigma_m Z_{m-1} - \gamma_m}{\sigma_m Z_{m-1} + \gamma_m} e^{-\gamma_m t_m}} = R_m + jX_m, \tag{2.19}$$

where $j = \sqrt{-1}$, t_m is the m_{th} layer thickness, $\gamma_m = (1+j)/\lambda_m$ is the complex propagation constant of the m_{th} layer, λ_m is the London penetration depth of the layer, σ_m is the complex superconducting conductivity for the frequency ω and can be calculated by the extended Zimmermann formula, μ is the permeability of the layer, Z_{m-1} is the impedance of the load which

yields the input impedance of the total layers before the layer, and equals to 377 Ω which is the characteristic impedance of free space when the layer is exposed to air.

The result above is obtained when the whole trilayer film is represented as a pair of thin conducting sheets. The two-sheet representation is sufficiently accurate when the thickness of the superconducting film t is much larger than its London penetration depth λ_L. In our experiment, λ_L of Nb is 29 nm [92] which is not much thinner than the total thickness of the trilayer film. Therefore, the above two-sheet model has deviations from a real conductor. To correct the discrepancy between the real composite superconducting film and the above two-sheet model, a modified value of surface impedance can be used [91]. Let Z_S be the calculated surface impedance as given by the above formula, and let Z_X be the value of the surface impedance of the conducting sheets which will cause an effective surface impedance of Z_S as seen by an incident wave, as depicted in Figure 2.3.

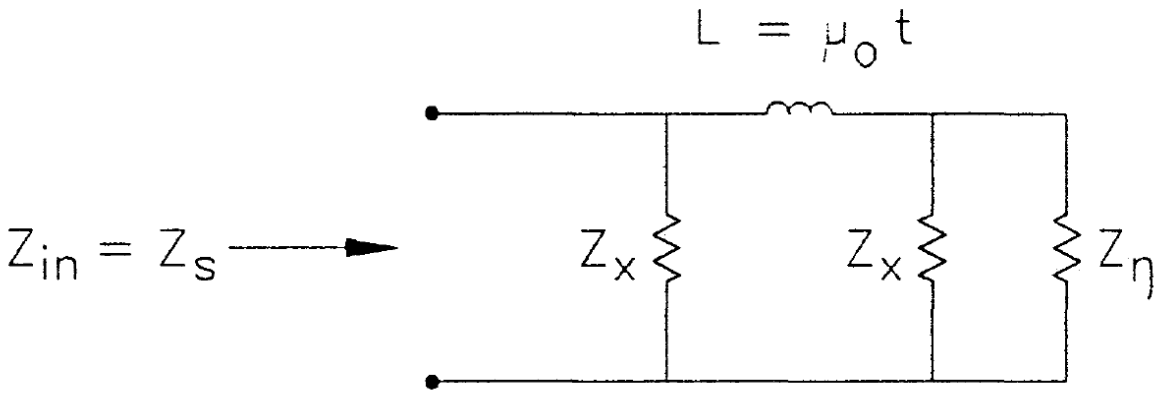

Figure 2.3: Illustration of the modification for the two-sheet model (excerpted from [91]).

In our case, Z_η is large compared with the other circuit elements, and can then be neglected. The analysis of the circuit gives an equation for Z_X whose solution is:

$$Z_X = \frac{1}{2}[(2Z_S - j\omega\mu_0 t) \pm \sqrt{4Z_S^2 + (j\omega\mu_0 t)^2}]. \qquad (2.20)$$

2.4.3 The extended Zimmermann formula

For a real superconductor, the conductivity σ_{sc} is a complex number. To calculate the complex conductivity, $\sigma_{sc}(\omega)=\sigma_1-j\sigma_2$, for a layer of superconductor with arbitrary purity, the Zimmermann formula [93] can offer an easy method when arbitrary mean free path length is considered. The integral of Green functions of energy has been applied to an expression for the complex conductivity of a homogeneous isotropic BCS superconductor with an arbitrary mean free path. By taking into account the gap energy of a BCS superconductor as a complex number, $\Delta=\Delta_1-j\Delta_2$ [94], where Δ_1 and Δ_2 are real numbers, we generalize the Zimmermann expression for the conductivity of a homogeneous isotropic BCS superconductor with complex gap energy which can be applied to the samples with any purity. The explicit expression for the conjugate of the complex conductivity $\sigma_{sc}^{*}(\omega)=\sigma_1+j\sigma_2$ reads:

$$\frac{\sigma_1+j\sigma_2}{\sigma_n}=\frac{j}{2\omega\tau}\times\left(\int_{\Delta}^{\hbar\omega+\Delta}I_1dE+\int_{\Delta}^{\infty}I_2dE\right), \tag{2.21}$$

$$\begin{aligned}I_1=\tanh\frac{E}{2kT}\{&[1-g(E)g(E-\hbar\omega)-f(E)f(E-\hbar\omega)]\frac{1}{P_3+P_2+j\hbar/\tau}\\&-[1+g(E)g(E-\hbar\omega)+f(E)f(E-\hbar\omega)]\frac{1}{P_3-P_2+j\hbar/\tau}\},\end{aligned} \tag{2.22}$$

$$\begin{aligned}I_2=&\tanh\frac{E+\hbar\omega}{2kT}\{[1+g(E)g(E+\hbar\omega)+f(E)f(E+\hbar\omega)]\frac{1}{P_1-P_2+j\hbar/\tau}\\&-[1-g(E)g(E+\hbar\omega)-f(E)f(E+\hbar\omega)]\frac{1}{-P_1-P_2+j\hbar/\tau}\}\\&+\tanh\frac{E}{2kT}\{[1-g(E)g(E+\hbar\omega)-f(E)f(E+\hbar\omega)]\frac{1}{P_1+P_2+j\hbar/\tau}\\&-[1+g(E)g(E+\hbar\omega)+f(E)f(E+\hbar\omega)]\frac{1}{P_1-P_2+j\hbar/\tau}\},\end{aligned} \tag{2.23}$$

where

$$g(E)=-\frac{E}{\sqrt{E^2-\Delta^2}},\quad f(E)=-\frac{\Delta}{\sqrt{E^2-\Delta^2}}, \tag{2.24}$$

$$P_1 = \sqrt{(E+\hbar\omega)^2 - \Delta^2}, \quad P_2 = \sqrt{E^2 - \Delta^2}, \quad P_3 = \sqrt{(E-\hbar\omega)^2 - \Delta^2}, \tag{2.25}$$

σ_n is the normal conductivity of the superconductor before the superconducting transition happens. $g(E)$ and $f(E)$ are the diagonal and off-diagonal components of the quasi-classical 2×2 matrix Green's function [95]. The factors in square brackets depend on the unperturbed propagators g and f. In a compact but not very transparent way, they describe the usual ingredients of a linear response formula, namely the density of initial and final states combined with the energy dependent coherence factors for the coupling of an electromagnetic field to quasiparticles. The factors such as $\frac{1}{P_1 - P_2 + j\hbar/\tau}$ has the information about dynamical properties of quasiparticle excitations like their lifetime. They include the quasiparticle lifetime τ due to impurity scattering. Note here that the integrations of two kernels I_1 and I_2 are both performed along the path running in parallel to the real axis. Furthermore, it is evident that this expression is free from the Fermi distribution function $f(E)$, so there is no need to introduce an effective chemical potential μ^* to the Fermi function [96] which, at most of the time, is difficult to evaluate.

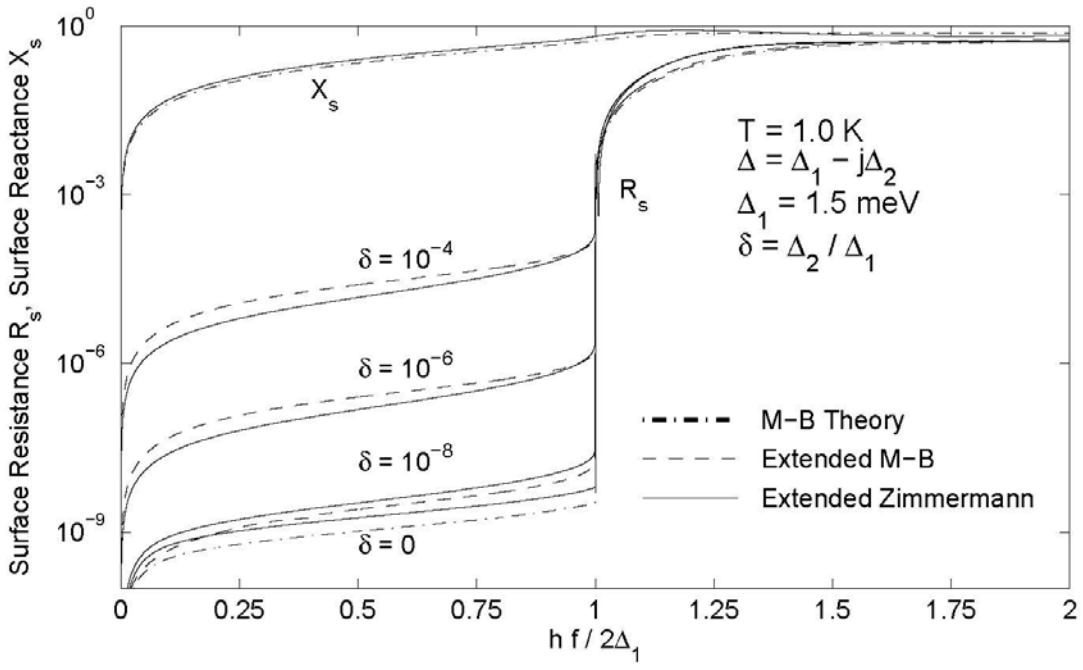

Figure 2.4: Surface resistance of single layer of Nb calculated by using (2.19) and (2.21) at 1.0 K when compared with the extended M-B theory developed by Noguchi *et al.* [97]

For Nb film with a gap energy of $\Delta_1 = 1.5$ meV, the transition temperature of $T_c = 9.2$ K at $T = 1.0\,\mathrm{K}$ $(T/T_c = 0.11)$ and the mean free path $\ell = 5.7$ nm [92], the surface resistances and reactance are calculated with (2.19) as a function of the normalized incident wave frequency for the different magnitude of the imaginary parts $\delta \equiv \Delta_2 / \Delta_1$ and plotted in Figure 2.4. Compared with the results from [97] which uses the same parameters for Nb film except for the consideration of the mean free path, the calculation results of the two kinds of methods match well, and only a small difference exists between the numerical data when $\delta = 10^{-4}$ and $\delta = 10^{-6}$ which is due to the original deviation between Mattis-Bardeen conductivity and Zimmermann conductivity.

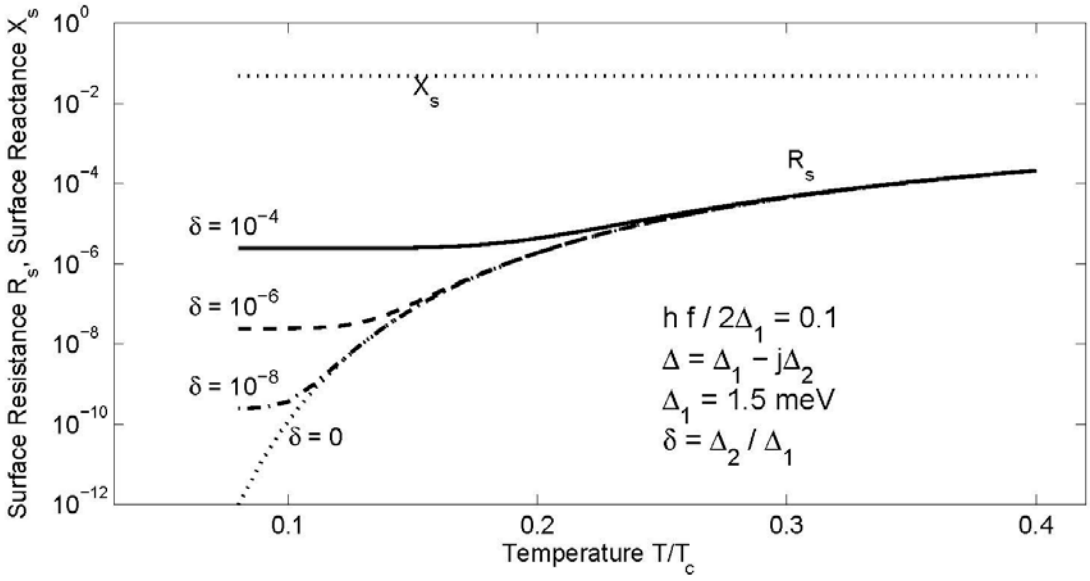

Figure 2.5: Calculated temperature dependence of the surface resistance and reactance as a function of δ

The surface impedance is also plotted in Figure 2.5 with the same parameters being used in Figure 2.4 as a function of normalized temperature T / T_c for different magnitude of the imaginary parts $\delta \equiv \Delta_2 / \Delta_1$. The real part of the gap energy is chosen to be fixed at 1.5 meV, although it should fluctuate as the temperature rises. The reason for this assumption is that the range of the temperature is restricted within only $0.3 \times T_c$, so the change of the real part of the gap energy deviates slightly from its 0K value. The dependence of the resistance and reactance on the temperature are the same as being calculated with the extended M-B theory reported in [97], in which the reactance X_s becomes independent of temperature when below $T_c / 2$ and the surface resistance is saturated at lower temperature regime due to the freeze of the frozen intra-gap quasiparticle density of states.

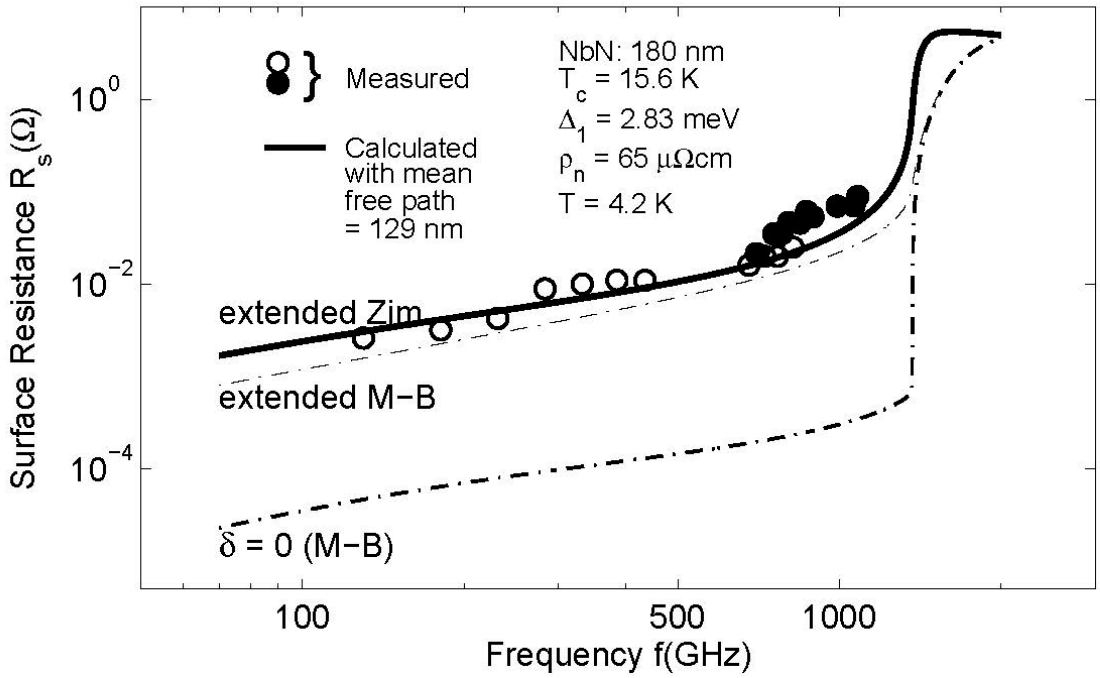

Figure 2.6: Calculated surface resistance compared with the standard and extended M-B theory against the experimental results in [98]

In Figure 2.6, The solid circles show the NbN surface resistance measured using resistively and capacitively shunted junctions with an open stub tuner [99]. The open circles show the surface resistances estimated using the junction with a resonator shown in [98]. The coherence length of NbN is 35 nm [100], and the penetration depth is 375 nm [101]. The ratio of the imaginary part to the real part of the gap energy δ is determined through the procedure as demonstrated in [102] and is set to be 8.1×10^{-3} [97]. The mean free path ℓ is determined from the normal resistivity given in [98]. Therefore, we have matched the extended Zimmermann formula with the experimental data of the strong-coupling superconductor NbN [98], which is in the local ($\lambda \gg \xi_0$) and clean limits ($\ell \gg \xi_0$). The prediction of the standard Mattis-Bardeen theory is also plotted in Figure 2.6 as a function of frequency.

Chapter 3

Superconducting resonators with Nb/NbN/Nb film

3.1 Introduction

The Mattis-Bardeen theory [103] is well-known for the calculation of the complex conductivity for the superconducting state in microwave field which can be used to compute the surface impedance. Recently, the Mattis-Bardeen (M-B) theory has been extended by Takashi, *et al*. [97] to include the contribution of quasiparticles in the subgap states of superconductors. Therefore, the improvement of the extended theory leads to a better approximation of the surface impedance for a homogeneous isotropic BCS superconductor than the standard M-B theory. However, the Mattis-Bardeen conductivity does not take into account the purity of a superconductor which can be expressed by mean free path ℓ. Since the coherence length is directly related to the electron mean free path in a given superconductor, the mean free path should play a major role in the evaluation of the complex conductivity of a given BCS superconductor. Furthermore, the original Mattis-Bardeen conductivity is obtained under the extreme anomalous limit, for which the coherence length of a BCS superconductor should be much larger than its characteristic magnetic field penetration depth ($\xi_0 \gg \lambda_{eff}$) [103]. Under this limit, the Mattis-Bardeen conductivity will give a good approximation for the behavior of the superconductor. Otherwise, the use of the expressions of Mattis-Bardeen conductivity will not be appropriate when the coherence length is comparable or even smaller than the penetration depth.

Two straightforward ways to decrease the surface resistance are to lower the temperature and grow high-quality epitaxial thick films. Here we introduce an alternative method. Due to the skin effect, the amplitude of the electromagnetic waves will decay exponentially inside the superconductors with a length scale of the penetration depth. Thus, the main contribution to the surface resistance comes from the surface of the thin film device. Thus, for Nb/NbN/Nb trilayer structures, the majority of the electromagnetic energy will be wrapped in the surface Nb layer, and only a small portion of the energy will go through into the NbN layer. This way we take benefit

from the intrinsic high-quality factor of Nb films. Because the inner NbN layer has much higher critical temperature T_c and upper critical field H_{c2}, it can enhance the superconductivity of the surface Nb layers through proximity effect. When the critical temperature of the Nb film is raised due to the proximity effect [104], the effective temperature T/T_c is reduced which leads to smaller surface resistance and larger quality factor. The improved H_{c2} also leads to enhanced performance in high magnetic fields which is highly desirable in many practical applications.

3.2 Comparison with the experimental data

The superconducting microwave resonator [17, 105] are four $\lambda/2$ microstrip line resonators in parallel rows which are separated by 65 μm. Each line resonator is 5650 μm long, 15 μm wide, as shown in Figure 3.1. They are deposited on 430 μm thick c-cut sapphire wafers and then patterned with optical lithography followed by reactive ion etching etched in Oxford PlasmaLab 100 ICP380 DRIE system. Figure 3.1 shows the Nb/NbN/Nb heterostructure on the substrate. Their central frequencies are both at 9.9 GHz. The 50-nm single layer Nb films and the 20/50/20 nm Nb/NbN/Nb trilayer films are grown by DC magnetron sputtering system with the base pressure 1×10^{-8} Torr, and the growth is performed at room temperature with Ar pressure of 3×10^{-3} Torr. The NbN layer is grown by reactive sputtering optimized with 7.7% nitrogen mixed in argon gas.

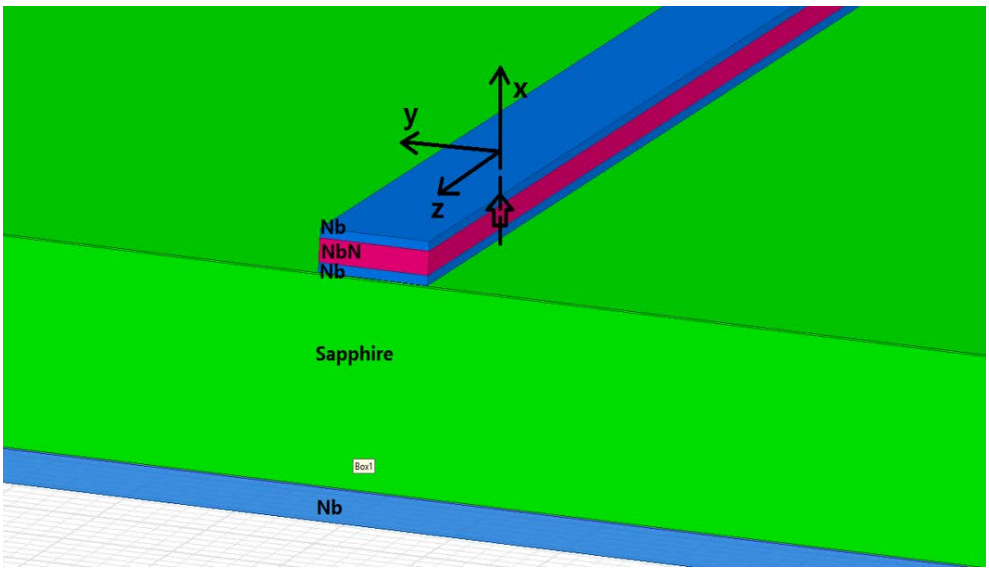

Figure 3.1: The schematic diagram for Nb/NbN/Nb on sapphire, and Nb on the back side.

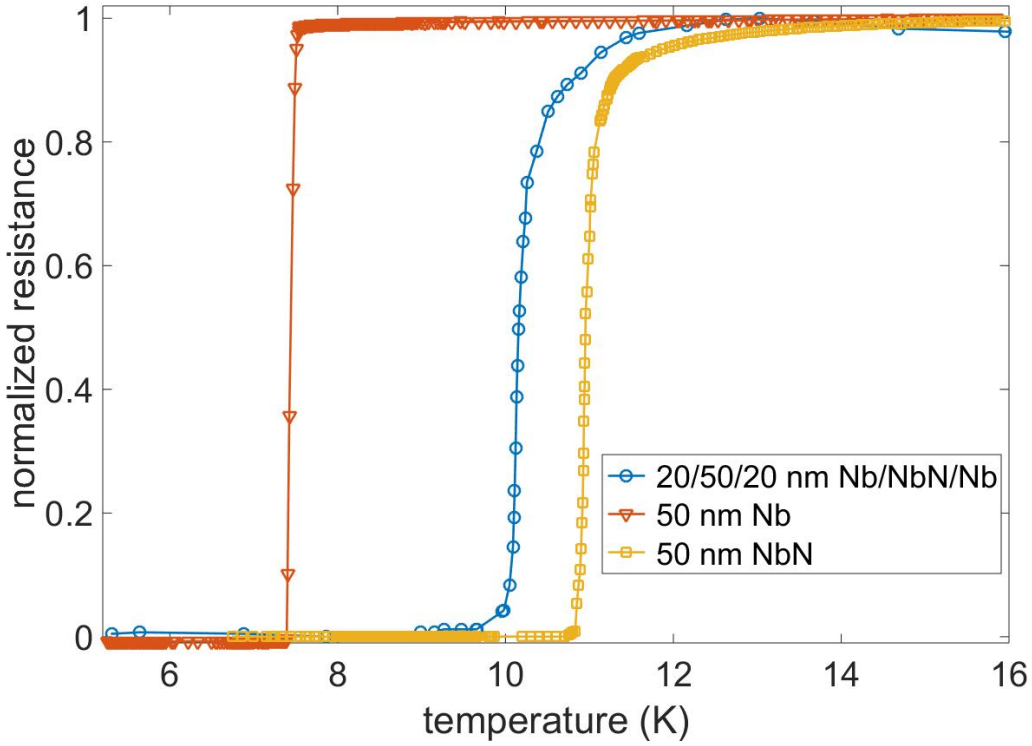

Figure 3.2: R-T curves for the superconducting films on sapphire, 50 nm Nb and 20/50/20 nm Nb/NbN/Nb.

In Figure 3.2, we compare the superconducting transition of the 20/50/20 nm Nb/NbN/Nb composite film with those of a pure 50 nm Nb film and a pure 50 nm NbN film. It is straightforward to expect that the Tc of the composite film falls somewhere higher than 50 nm Nb (7.7K) but lower than 50 nm NbN (11K) due to the proximity effect.

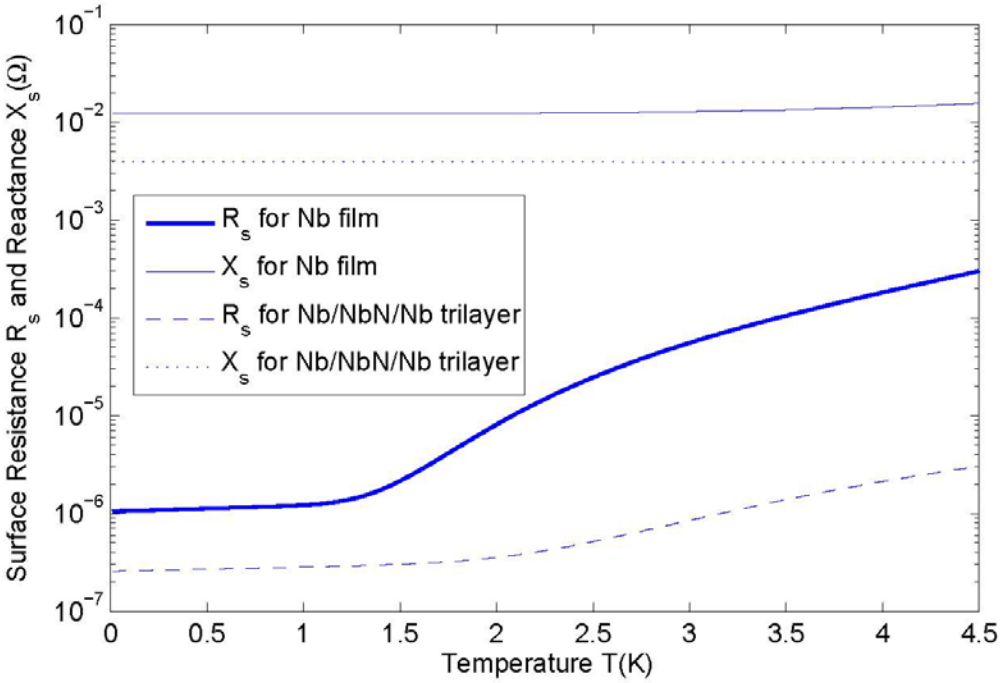

Figure 3.3: The surface impedance for the cases of single Nb film and Nb/NbN/Nb trilayer films

The surface resistance and reactance of the 50 nm Nb film and the Nb/NbN/Nb trilayer films are plotted as a function of temperature in Figure 3.3. The surface impedance of single Nb film is calculated with the extended Zimmermann formula by considering its imaginary part of the gap energy and the material electron mean free path. Since the Nb film is polycrystalline which is determined from X-ray diffraction results, the dirty limit of the parameters of the Nb [92] is considered. For the trilayer films, the coherence length and the penetration depth of NbN layer refer to 35 nm [100] and 375 nm [101], respectively. The real part of NbN gap energy at 0k is 2.105 meV [106]. The T_c of trilayer films is 9.8 K, which is probed by four terminal measurements and should be the T_c for the NbN layer. T_c of 20 nm Nb alone is reduced to 5.5K due to its thinness. The rise of the transition temperature of Nb film due to proximity effect is taken into account by increasing its T_c to 9 K in order to fit the data best.

$\delta \equiv \Delta_2 / \Delta_1$ of all three layers in trilayer films are set to be 9.4×10^{-4}, and that of the single Nb layer is determined to be 1.14×10^{-4}. Both values are separately decided in order to fit the experimental data best. It has been shown that Δ_2 should decrease with decreasing temperature [94]. The ratio of Δ_2 to Δ_1 is set to be dependent on temperature:

$$\delta = \delta_0 exp(\frac{k_B T}{\Delta_0}), \tag{3.1}$$

where δ_0 is the ratio of Δ_2 to Δ_1 at zero temperature, Δ_0 is the real part of the gap energy at zero temperature, k_B and T are the Boltzmann constant and the temperature, respectively.

The surface resistance of both single layer and trilayer films become bigger as the temperature rises, and the trilayer structure shows enhanced Q-factor throughout the whole temperature range. Furthermore, the surface resistance of the trilayer films only begins to increase above 2K while that of the single layer Nb film already does so at 1K.

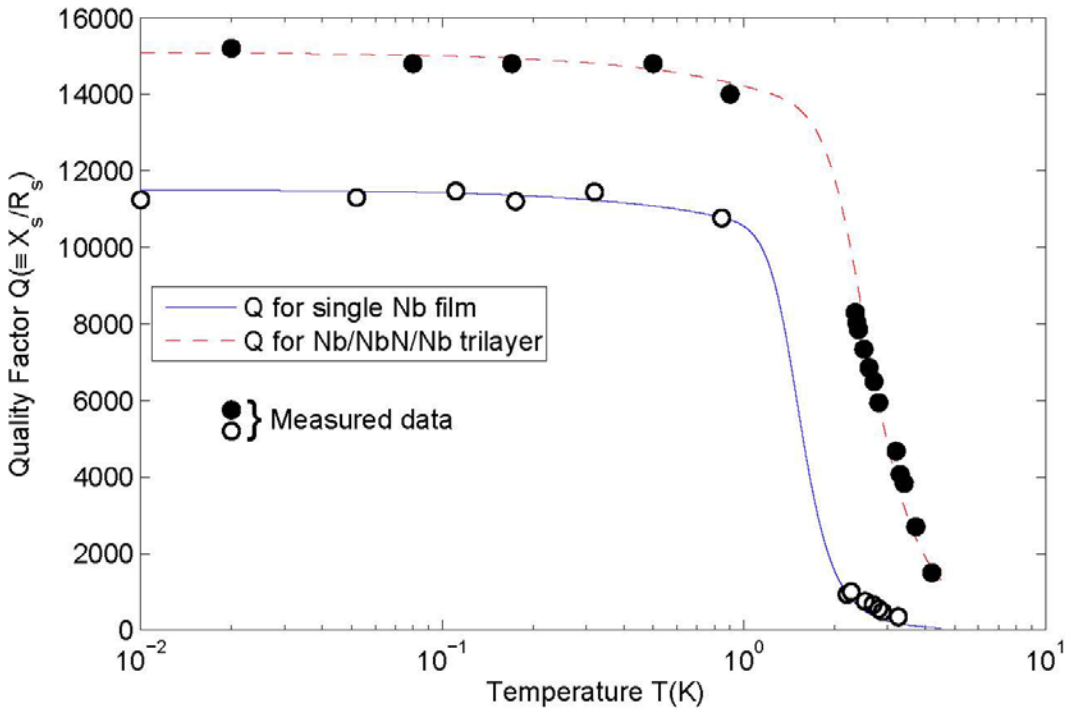

Figure 3.4: The quality factor for the microstrip microresonator with single Nb and Nb/NbN/Nb trilayer

In Figure 3.4, the solid and dotted curves represent the theoretical quality factor for 50 nm single Nb layer and 20/50/20 nm Nb/NbN/Nb trilayer films, respectively. Small circle dots are experimental data for corresponding microresonators. For a 40 nm single Nb layer, we can expect its quality factor to be even lower than the 50 nm thick one due to the reduced T_c. Therefore, with the same total thickness of Nb layer, the proximity effect can improve the quality factor at least by 30%. Note that the imaginary part of the gap energy for Nb and NbN is determined to give the best fit to the measured data.

3.3 Summary

We compare Nb/NbN/Nb trilayer structures with Nb single layer structures for their performance as superconductor resonators. The microwaves are wrapped inside the low loss Nb surface layers due to skin effect, while the superconductivity properties of these surface layers are enhanced through proximity effect from the middle layer. The quality factor of microstrip line resonators made of 20/50/20 nm Nb/NbN/Nb trilayer films has been calculated as microwave transmission through the cascade of three single layers, and in agreement with experimental data. Each layer is evaluated with an explicit extended Zimmermann expression. The formula is generalized from the regular expression by including electron mean free path and the imaginary part of the gap energy of the material. The quality factor of the microresonator consisting of a 50-nm thick single layer Nb film is also calculated by this compact expression and quantitatively agrees with the measured results as well. The quality factor of the microresonator made of trilayer films is shown to be larger than that of the microresonator with only a single Nb film.

Chapter 4
Superconducting resonators based on TiN/Tapering/NbN/Tapering/TiN heterostructures

4.1 Introduction

In this work, niobium nitride (NbN) and titanium nitride (TiN) are chosen as our candidate materials. NbN has an extremely large upper critical field (~15T) [107] which allows it to withstand high magnetic fields, while TiN so far holds the highest record on resonator Q values in zero fields (10^7) [108]. C-cut sapphire wafers were used as the substrate due to its high dielectric constant (~11.5), and its extremely low loss-tangent (~10^{-8} at low temperature) [109] to minimize energy loss into the substrates.

Although TiN is currently one of the best candidates for high-Q superconducting resonators, its performance in magnetic fields is limited by its relatively low critical field. In order to make the performance of the film suitable for use in magnetic fields, we take advantage of the proximity effect [86, 110-112] by inserting a NbN layer between two layers of TiN. The upper critical field Hc2 of bulk NbN is as large as 15 T [107], while the H_{C2} of TiN film (5 T for an 18 nm thick TiN film [113]) is much smaller. When coupled to a layer of superconductor NbN with higher H_{C2}, TiN can stabilize its superconducting state to a larger magnetic field than at its intrinsic H_{C2}.

Moreover, the lattice structure of NbN is also fcc, the same as that of TiN. The lattice constants of NbN and TiN are 4.394 Å and 4.424 Å, respectively, and hence resulting in a lattice mismatch of 3.6%. Thus, stacking NbN on TiN is readily achieved with compatible deposition conditions. As the surface is not perfectly formed, there may be numerous physical anomalies in the core/peripheral interface. These points may increase the concentration of quasiparticles and weaken the pairing correlations. On the contrary, the proximity effect [114] will strengthen the pairing correlations at the surface layers and reduce quasiparticle generation. This effect has often been studied within approaches including an important parameter, the interface transparency parameter T [115, 116]. This parameter takes into account all factors which cause electrons to be reflected rather than transmitted at the interfaces, with the result that proximity effect is somewhat

screened. Interfaces between different materials are never completely transparent, and this may result from interface imperfections, and lattice mismatches [117]. To increase the interface transparency and enhance the proximity effect, we taper the interfaces between TiN and NbN. Tapering is a widely-used technique in waveguides to improve wave propagation (reduce reflection) across impedance mismatched interfaces. The gradual change allows for the propagating waves to distort only very slightly in each step, thus preventing massive reflections at a given boundary. Since NbN and TiN are fully compatible and can be mixed in any proportion, we can gradually vary the heterostructure from pure TiN into pure NbN through an intermediate $(Ti_xNb_{1-x})N$ layer (by varying composition ratio x), and vice versa. This tapering layer eliminates the distinct boundaries between TiN and NbN and makes the wavefunction change smoothly between NbN and TiN. This helps to reduce reflected waves on the interfaces and improves proximity coupling between the layers.

In this work, the composite films consisting of TiN and NbN with tapering interfaces on c-cut sapphire substrates were grown by reactive magnetron sputtering. The crystal quality of the composite films was investigated with X-ray diffraction (XRD), energy-dispersive X-ray spectroscopy (EDS), transmission electron microscopy (TEM), and X-ray photoelectron spectroscopy (XPS). The heterostructures are further patterned into half-wavelength microstrip transmission line resonators for the microwave (~10 GHz) transport measurement from 16 mK to 1 K, and under varying magnetic fields.

4.2 Film growth

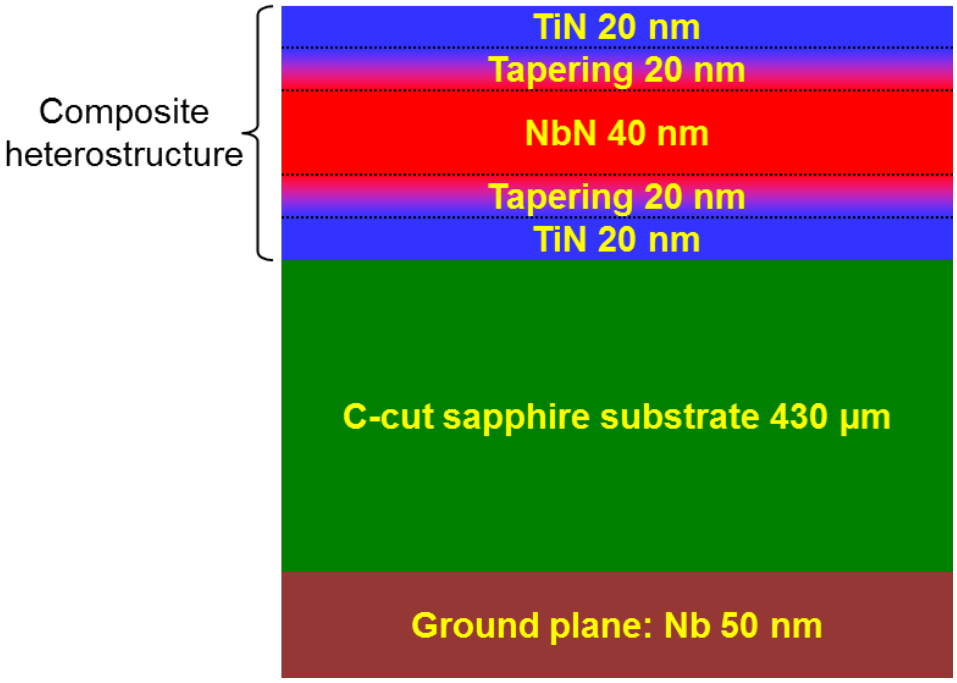

Figure 4.1: Schematic structure of TiN/tapering/NbN/tapering/TiN composite film on a c-cut sapphire. The back side is coated with 50 nm Nb.

The structure of the composite film is TiN/tapering/NbN/tapering/TiN, where the tapering is achieved by continuously varying x in the $(Ti_xNb_{1-x})N$ compound. TiN and NbN films were grown with face-centered-cubic (fcc) structure on the c-cut hexagonal-close-packing (hcp) sapphire wafers. The films were deposited on the front side of a double-side-polished sapphire wafers, while the back side of the wafers was coated with 50 nm pure Nb as the ground plane of the superconducting transmission line resonators. Pure Nb, deposited at room temperature without pre- and post-annealing, was chosen as the ground plane in order to avoid heating damage to the materials already present on the front side. The samples were deposited in a reactive magnetron sputtering system (AJA International, USA) with the base pressure of $1x10^{-8}$ Torr. The substrates were first Ar-sputter cleaned for 5 minutes under substrate bias with 50W RF power, 5 milli-Torr chamber pressure and 30 sccm of Argon flow. Then they were annealed at 700°C for 1 hour, and let it cool down for 7 hours to room temperature in Argon. The annealing time is long enough to

ensure that the final temperature of a substrate is at room temperature. The deposition procedures were as follows. The chamber pressure was maintained at 3 milli-Torr, with the partial pressures of N and Ar being 0.2 and 2.8 milli-Torr, respectively. First, TiN was deposited at room temperature by sputtering 99.95% pure Ti. The sputtering power was 200 W, and the deposition rate of TiN was around 0.7 Å/s. Next, the tapering layers were created by gradually ramping down the power of the Ti target to 20 W over 5 minutes, while gradually increasing the power of two Nb targets from 30 to 100 W. Then, the pure NbN layer was deposited with two Nb targets at 100 W each. Finally, the structure was continued in a reversed order by growing another tapering interfacial layer from NbN to TiN and the top pure TiN layer. The deposited tapering layer does induce a small jump in composition near the starting and finishing sides (a jump of x around 0.1) because 30 W is the minimum power to strike a stable plasma on the sputtering targets in our reactive magnetron sputtering system.

4.3 Characterization of the composite films

4.3.1 X-Ray diffraction characterizations

X-ray diffraction (XRD) was used to study the microstructure of the composite films grown on the c-cut sapphire. The measurement was carried out using a Bruker D8 Discover (Bruker AXS, Germany) system with a Cu Kα source.

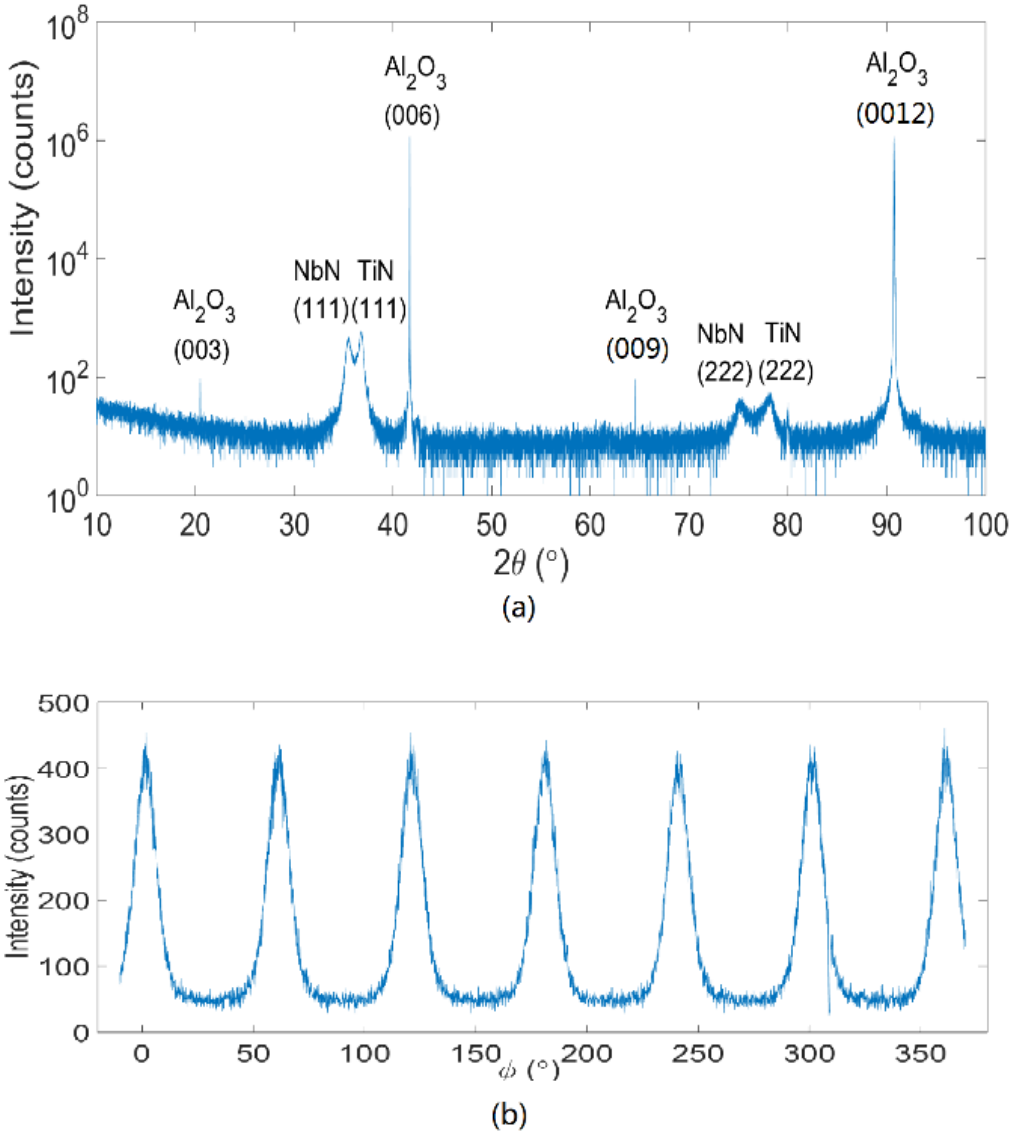

Figure 4.2: (a) High-resolution XRD pattern of TiN/tapering/NbN/tapering/TiN composite film on the c-cut sapphire. (b) Azimuthal XRD data ("φ-scan") reveals the six-fold symmetry of the off-axis (200) reflections from both NbN and TiN.

Figure 4.2(a) shows the high-resolution 2θ-ω scan of the composite film. A 3-bounce monochromator was used in front of the source in addition to a Gobel mirror. There are two extremely sharp and intense peaks located at 41.68° and 90.72° representing diffraction from the

sapphire (006) and (0012) planes, respectively. The other two sharp peaks located at 20.50° and 64.51° are the sapphire (003) and (009) diffractions. Because of destructive interference from structural extinction, these two peaks should be forbidden on the XRD pattern, but they still show up (albeit orders of magnitude weaker) due to imperfections crystal. Besides these peaks from sapphire, there are only (111) peaks from NbN at 35.59° and TiN at 36.67° and their second order diffraction (222) peaks. The appearance of only (111) peaks from the composite films indicates that the TiN and NbN are both in their pure phase and preferentially oriented along the (111) direction. Figure 4.2(b) is the azimuthal XRD data ("φ-scan") from the TiN/tapering/NbN/tapering/TiN composite film by setting psi at 54.7° - the angle between the (111) plane and (200) plane in fcc structures. The detection angle 2θ was set to 41.1° in order to detect the NbN (200) reflections primarily. Since the mismatch of the lattice constants between TiN and NbN is only 3.6%, the TiN (200) reflection is very close to the NbN (200) reflection such that some diffraction from the TiN layers is also included in the φ-scan. Fully epitaxial NbN (111) should display three-fold symmetry in the φ-scan of (200) plane instead of the observed six-fold symmetry. The six peaks indicate two symmetrically equivalent growth orientations (twins) occur in the composite film structure. This is due to the stacking of three-fold symmetric fcc structures onto the six-fold symmetric hcp substrate. In other words, when placing the ABC type stacking (fcc) onto the AB type stacking (hcp), the growth could be either $(ABC)_n$ or $(CBA)_n$ with equal nucleation probabilities. These two twin variants differ by 60° about the [111] axis of NbN, and locally they are epitaxial with the substrate. Stacking faults will show up at the boundary between adjacent domains. We also recorded the 2θ-ω scan by fixing φ at 61.6° corresponding to one of the peaks in Figure 4.2(b). Bragg diffraction in this direction, 41.1° for NbN and 42.6° for TiN, well matches the NbN/TiN (200) reflections, which proves that the six-fold symmetry shown in Figure 4.2(b) indeed originates from off-axis diffraction of NbN (200) and TiN (200) planes. The presence of twins for TiN and NbN on surfaces of hexagonal symmetry have been reported before [118, 119]. From the off-axis XRD result, we can deduce the two twin variants are:

$$\text{Variant 1: } [10\bar{1}]_{\text{TiN, NbN}} \,//\, [10\bar{1}0]_{\text{sapphire}},$$

$$(111)_{\text{TiN, NbN}} \,//\, (0001)_{\text{sapphire}},$$

$$\text{Variant 2: } [1\bar{1}0]_{\text{TiN, NbN}} \,//\, [10\bar{1}0]_{\text{sapphire}},$$

$(111)_{TiN,\ NbN}$ // $(0001)_{sapphire}$.

4.3.2 Energy dispersive X-ray spectroscopy mapping and transmission electron microscope characterizations

To characterize the crystalline structures of the samples, scanning transmission electron microscopy (STEM) techniques with energy dispersive X-ray spectroscopy mapping (EDS) were utilized. The STEM imagines were recorded using an ARM-200F (JEOL, Tokyo, Japan) scanning transmission electron microscope operated at 200 kV with CEOS Cs corrector (CEOS GmbH, Heidelberg, Germany) to cope with the probe-forming objective spherical aberration. EDS spectra were collected simultaneously for mapping the distribution of Ti, Nb, and N throughout the film.

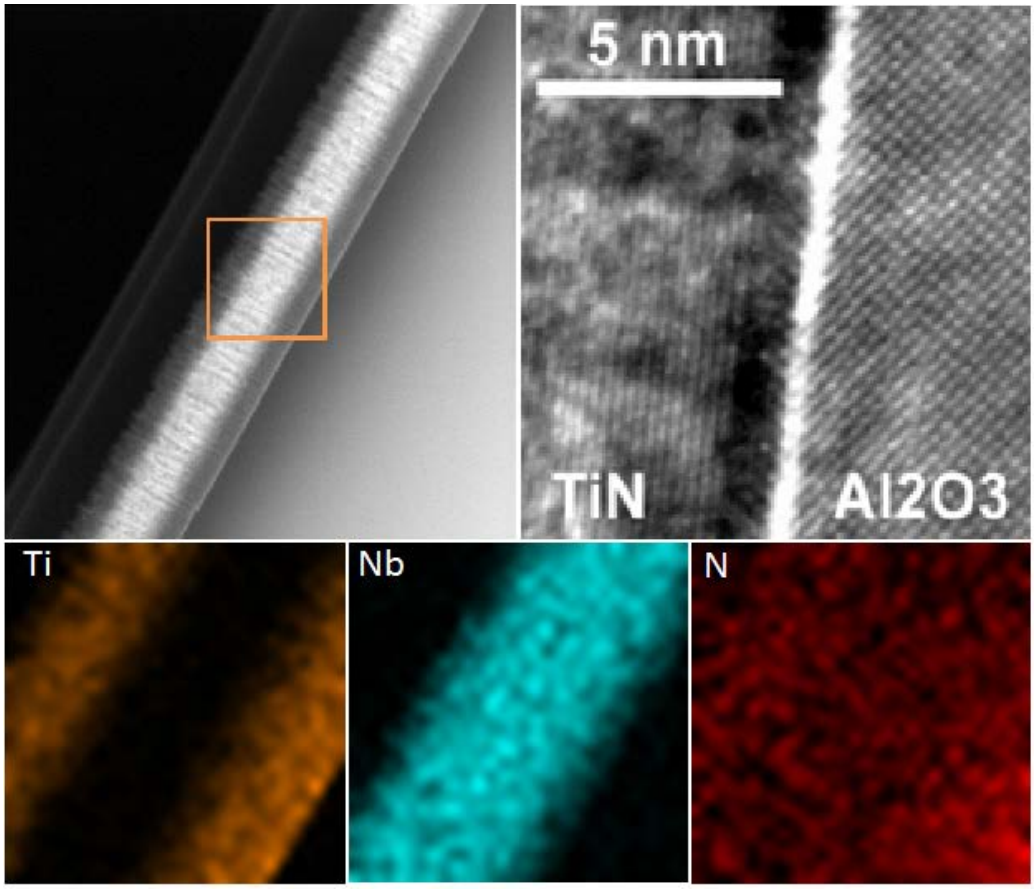

Figure 4.3: (a, upper left) Sample overview by cross-section transmission electron microscopy. (b, upper right) Close up view at the substrate-film interface showing a sharp interface and a clear film growth in the (111) orientation. (c, lower) Elemental distribution in the square area of (a), different colors represent different elements, and the brightness indicates the concentration of these elements.

Figure 4.3(a) is the STEM image of the composite. Periodic white and dark columnar features show up parallel to the growth direction. These lines indicate irregular columnar growth, which further validates the twin variants of the composite film. The STEM picture also presents no clear interface between the TiN and NbN layers because they are intentionally connected through gradually tapered layers. Figure 4.3(b) is a close-up at the substrate-film interface. Clear TiN crystal planes parallel to the interface can be seen in the figure, indicating (111) oriented growth. The twins that we have shown with XRD may cause the absence of long-range ordering in the in-

plane directions. Figure 4.3(c) displays the distribution of Ti, Nb, and N within the square area of Figure 4.3(a) STEM graph. Brown colors in the lower left graph represents Ti, cyan colors in the lower middle graph represents Nb, and red colors in the lower right graph represents N. The distributions of Ti, Nb, and N clearly show that Ti forms the top and bottom layers of the heterostructure, while Nb constitutes the core of the sandwich. The distributions of Ti and Nb overlap at their boundaries corresponding to the tapering, while N is distributed quite evenly across the whole structure as expected.

The brightness in the graph is related to the element concentration as well as material thickness. In Figure 4.3(c), there seems to be more TiN close to the substrate than at the top layer. The different brightness may be attributed to the different thickness of metal layer near the substrate. Most likely, during the cross-sectional TEM sample preparation process with FIB, the sapphire substrate is known to be very robust against etching and tends to stay slightly thicker, which also partially blocks the etching near the substrate, therefore TiN near the substrate tends to be slightly thicker than those further away, creating a higher chemical appearance.

4.3.3 X-ray photoelectron spectroscopy characterizations

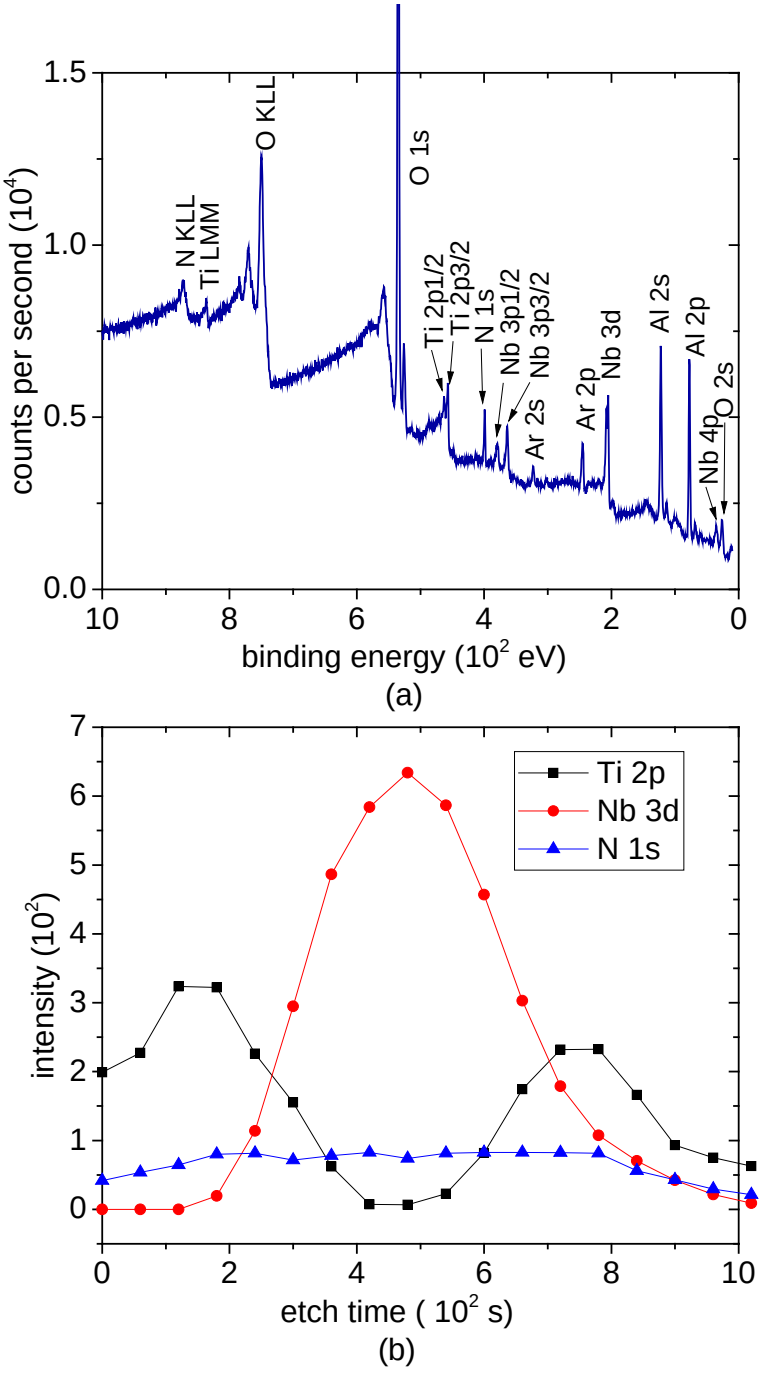

Figure 4.4: (a) XPS spectrum after the composite film was Ar sputtered into one of tapering layers. (b) Depth profile of the whole composite film.

The composite film with tapering interfaces grown on the c-cut sapphire substrate has been analyzed by X-ray Photoelectron Spectroscopy (XPS) using SPHERA II analyzer (Omicron Nanotechnology GmbH, Germany). Mg K_α was used as the X-ray source, and the pass energy was set at 50eV. Figure 4.4(a) shows a spectrum taken within one of the tapering layers between TiN and NbN. This layer was exposed after Ar ion sputtering on a patterned resonator device for 5 minutes. Ti, Nb and N peaks shown in the figure come from the tapering film itself, while the Al and O peaks are from the substrate (exposed area outside the active resonator region). By coupling sputter etching with XPS, the depth profile of the whole composite film is also presented in Figure 4.4(b). Ti and Nb concentrations in the film are consistent with a sandwich-like structure with tapering transitions, while the N condensation remains virtually unchanged throughout the film. It is noted that the condensations of both Ti and N are slightly smaller at the start of the ion milling. This is because the patterned sample surface has many contaminants (C, N, organic compounds, etc.) which lower all of the elements intensities. After sputtering for 120 seconds, the condensations of N and Ti reach their peaks, and this means the surface contaminants on the film are fully removed and the XPS spectrum is purely from the first TiN layer. The long tail of Ti, Nb, N intensity on the substrate side can be attributed to elements being stricken into, instead of being sputtered away from, the substrates.

The nominal sputter rate of Ti is expected to be quite stable under given conditions, but we cannot completely rule out the possibility that the Ti concentration varies slightly during the process. On the other hand, the measured Ti intensity is not a sole function of the intrinsic Ti concentration. For example, when sputtering the top layer, the light Ti element can be readily sputtered into the next layer, causing seemingly more inter-diffusion between Ti and Nb and higher peak of Ti signals, but this is only an artifact caused by the sputter profiling. At the bottom interface, however, Nb is hard to be stricken into the next layer, and a cleaner interface and comparatively weaker signal are seen. As a comparison, the peak of N remains more or less unchanged indicating the sum of Ti and Nb together is roughly a constant.

4.3.4 Transport characterizations

We measured the superconducting transition temperature (Tc) for the 120 nm composite film with a DC four-terminal measurement. We find the Tc for the film is 10K. For bulk TiN and NbN, their

critical temperatures are 5.6K and 16K, respectively, and they both decrease in thin films. In Figure 4.5, we compare the superconducting transition of the composite film with those of a pure 50 nm NbN film, a pure 50 nm TiN film, and a few 50 nm $(Ti_xNb_{1-x})N$ films. It is straightforward to expect that the Tc of the composite film falls somewhere higher than TiN (3.2K) but lower than NbN (11K) due to the proximity effect. The final Tc is loosely equivalent to that of a uniform $(Ti_xNb_{1-x})N$ film with x~1/5. As a comparison, the average concentration of Ti inside the composite film is about 1/2. The superconducting transition width for $(Ti_{0.5}Nb_{0.5})N$ sample is larger than others. This width depends on many factors such as the phase structure and the internal film strain. The Large internal strain may account for the gentle slope of a superconducting transition curve. In $(Ti_{0.5}Nb_{0.5})N$ sample, the mismatch between TiN and NbN results in larger strain than in their single crystal phase. The two critical transitions found in the curve for $(Ti_{0.2}Nb_{0.8})N$ sample may be due to the inhomogeneous growth of the film, since the plasma of a sputtering target in our system may be unstable at very low power.

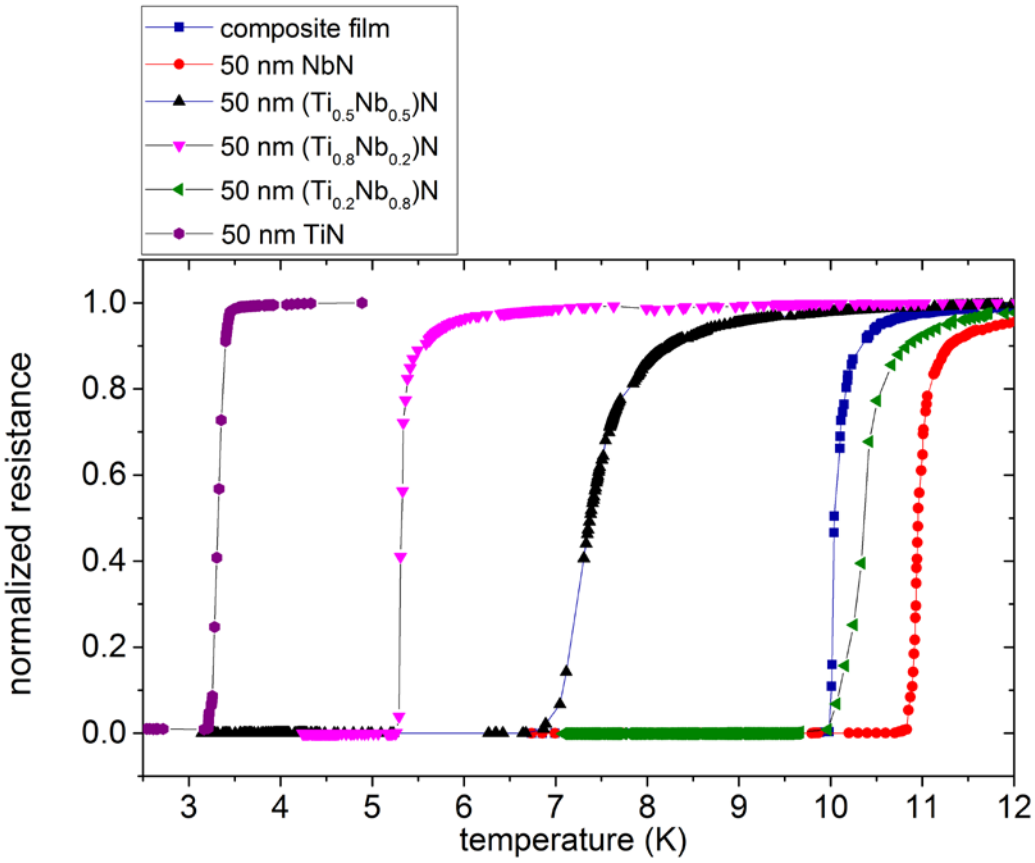

Figure 4.5: R-T curves of the composite film, 50 nm NbN, 50 TiN and 50 nm $(Ti_xNb_{1-x})N$ with varied concentration x (x = 0.2, 0.5, 0.8).

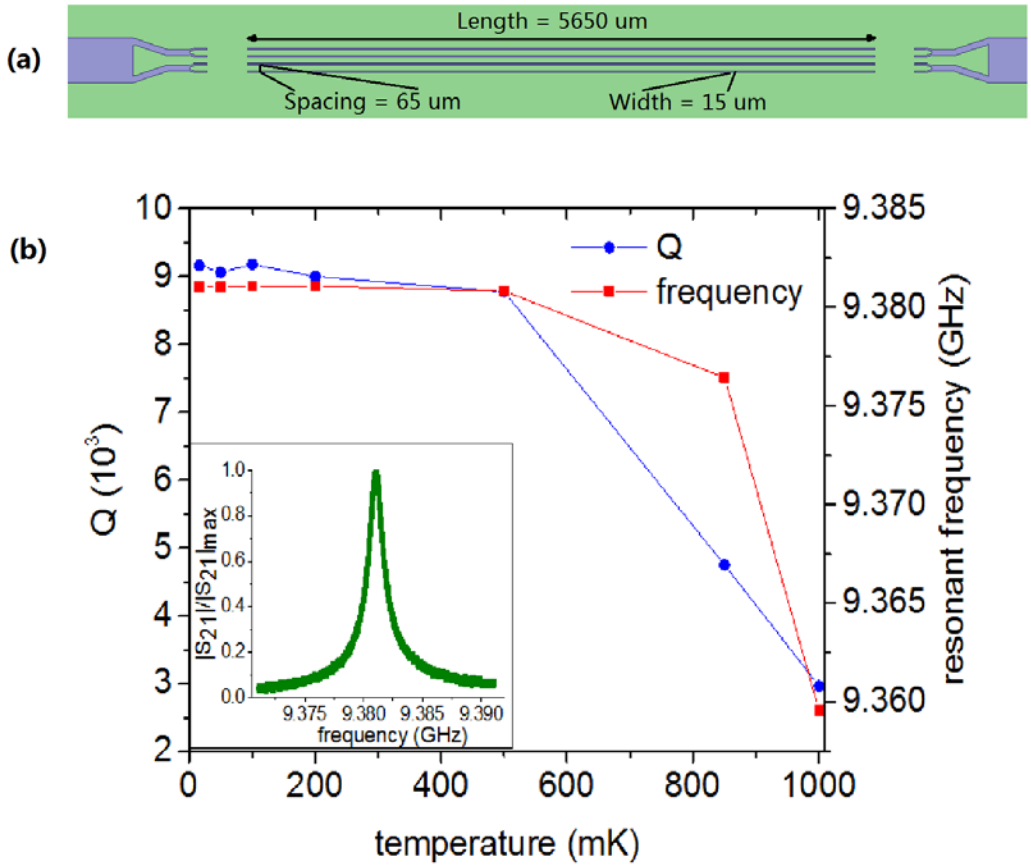

Figure 4.6: (a) The device consists of four parallel λ/2 microstrip line resonators, which are separated by 65 μm. One λ/2-resonator is 5650 μm, 15 μm wide. It is patterned on a 430 μm thick sapphire wafer, which has Nb ground plane on the other side. (b) Quality factor and resonant frequency of a superconducting resonator (in nm: 20 TiN / 20 tapering / 40 NbN / 20 tapering / 20 TiN) versus the temperature. The measurement was performed under zero applied field. Inset, the plot of the normalized scattering matrix S21 around the resonance frequency.

We used optical lithography and reactive ion etching to fabricate half-wavelength microstrip transmission line resonators from the composite films. The superconducting microwave resonator [105] are four λ/2 microstrip line resonators in parallel rows which are separated by 65 μm. Each line resonator is 5650 μm long, 15 μm wide, as shown in Figure 4.6(a). Compared to 3D cavities, or coplanar waveguides (CPW), microstrip line resonators see stronger loss mechanisms and show

lower Q values in general. For example, the dielectric loss, due to the concentrated electric fields passing through the substrate towards the ground plane, and the radiation loss, due to EM fields distributed in the vast open space around the resonator, are much more pronounced in microstrip line resonator structures. On the other hand, they offer small mode volume and uniform magnetic fields at microwave frequency and therefore are better suited for pulsed ESR.

Table 4.1: The comparison of the Q values from the composite film and single Nb films with the same resonator design.

Film	Q value	
	At 0 field	At 0.35 T
TiN/tapering/NbN/tapering/TiN	9162 at 16 mK	5300 at 100 mK
single 40 nm Nb [120]	11240 at 10 mK	–
400 nm Nb [105]	43000 at 21 mK	6000 at 21 mK

The measurement of the resonators was carried out with a CF dilution refrigerator (Leiden Cryogenics BV, BA Leiden, Netherlands). The resulting quality factor and the resonant frequency as a function of temperature are presented in Figure 4.6(b). The resonance frequency shift with temperature is a standard behavior of all superconductors as a result of the temperature dependence of the complex conductivity [121]. The observed quality factor drops with increasing temperature. This can be understood from the temperature dependence of the London penetration depth [122, 123]. As temperature increases, the penetration depths of the materials also increase, and therefore more microwave can leave the surface layer and enter the core region, which induces more loss. In Table 1, the quality factors from the composite film are compared with those from single Nb films reported previously with the same resonator design. The internal quality factor under 16 mK is

over 9000 and comparable to our previous best results on 40nm pure Nb resonators of the same design [120].

The quality factor may be degraded by the strain in the TiN layer and $(Ti_xNb_{1-x})N$ tapering layer. S Ohya *et al.* [124] have argued that in-plane stress of TiN film will negatively affect the quality factor of superconducting coplanar waveguide (SCPW) resonators. Their experiments show that the films with the films with in-plane stress 3.8 GPa correspond to the internal quality factors ranging from 2×10^4 to 5×10^4, while the quality factors are enhanced to the range of 8×10^5 to 5×10^6 by films with 0.15 GPa in-plane stress. We targeted the in-plane stress (Pa) and the corresponding quality factors as two variables and calculated the Spearman's rank correlation coefficient (a perfect Spearman correlation of +1 or −1 occurs when each of the variables is a perfect monotone function of the other) for the data in their paper. The coefficient ρ of the correlation between in-plane stress (Pa) and quality factors is -0.8460, which means a large negative correlation between the film in-plane stress and the quality factors of the resonators fabricated from the film. If we assume that the TiN layer is strained to the mean of the bulk TiN and NbN lattice constants, the strain is 1.8%. By considering that Young's modulus of TiN (111) is 450 GPa [125], it can be easily estimated that the in-plane stress in our TiN film is 8.1 GPa. Therefore, considerable in-plane stress in our sample induced by the mismatch of lattice constants of NbN and TiN may deteriorate the quality factor.

Under a magnetic field of 0.35 T, however, the quality factor dropped to around 5300. This can be attributed to the lower critical field (H_{c1}) of the chosen materials. 0.35T is not large enough to quench superconductivity completely (which requires the upper critical field H_{c2}), but sufficient to nucleate magnetic vortices throughout the device. The vortices vibrate under the microwave driving currents and dissipate energy from the resonator.

In this work, we have made the first significant step towards enhancing Q values in magnetic fields. The top and bottom TiN films play crucial roles in determining the intrinsic Q values. Further optimizations on the structural quality and nitrogen concentration will further reduce the losses from these layers. Also, adjusting the thickness of the TiN layers and the tapering layers can also improve superconducting wavefunction distribution across the system and enhance Q values further. Too thick TiN layer and the tapering layer may lower the robustness against the magnetic field, while too thin layers will have little enhancement on the Q value. Though we have some

qualitative understanding of this system, to fully analyze the superconducting wavefunction in this complicated system turns out to be a formidable task. As discussed in the chapter, a single layer of TiN has already achieved high Q values but only under zero magnetic fields, and the composite system aims to combined the best qualities of TiN and NbN to yield better Q values for magnetic fields performances. We are very confident that the Q values can be significantly improved with continued fine tuning on this material system.

4.4 Summary

We fabricated a type of superconducting heterostructures, TiN/tapering/NbN/tapering/TiN, on c-cut sapphire substrates by reactive magnetron sputtering. The goal is to achieve an x-band resonator that maintains a high Q in modest magnetic fields. We explored the details of the structures with X-ray diffraction (XRD), energy-dispersive X-ray spectroscopy (EDS), transmission electron microscopy (TEM), X-ray photoelectron spectroscopy (XPS) and transport measurements. The structure shows (111) orientation with local epitaxial correlation and global twin variation, because of stacking face-centered-cubic structures on top of hexagonal-close-packing substrates. The artificial tapering layers vary gradually from NbN into TiN and vice versa, creating a smooth transition so that no distinct interface exists. We also measured the quality factor of a transmission line resonator made of the composite film, and Q values over 9000 without field and 5300 under 0.35 T magnetic field were recorded on these devices. The quantum devices with this type of superconducting heterostructures are promising candidates for quantum information processing with hybrid nuclear-electron spins.

Chapter 5
Phonon engineering in proximity enhanced Al/Nb/Al superconductor heterostructures

5.1 Introduction

As superconducting circuits scale up, the quality of superconducting thin films plays a more and more important role in determining the ultimate performance of the superconducting quantum networks. Because of the limited choices of superconductor materials for quantum devices, how to improve the existing superconducting materials becomes a major challenge for the further advancement of superconducting quantum information processing. In the Bardeen–Cooper–Schrieffer (BCS) theory, the electron-phonon coupling is the most fundamental properties of superconductors. Adjusting phonon density of states (DOS) can, therefore, tailor the recombination time of Cooper pairs in superconducting thin films and hence affect the coherence time of qubits and Q values of resonators. Phonon spectra in superconducting thin films undergo considerable modifications as the phonon wave vectors out of the film plane are restricted by the film thickness, which causes phonon DOS to show discontinuities at specific energies. To the best of our knowledge, phonon engineering has not been realized in superconducting resonators since it can only occur in ultra-thin films which will induce significant microwave losses for resonators and decoherence for qubits. In a trilayer heterostructure consisting of one thick core layer and two thin cladding layers, the phonon quantization shows up in the cladding layers due to the local phonon DOS. Such superconductor heterostructure can be readily utilized for improving quantum devices.

In this work, we examine a model system of proximity-enhanced Al/Nb/Al heterostructures, and we consider the size effect of the ultrathin Al cladding layers. The two Al layers are thin enough such that the size effect of thin films becomes appreciable. For thin enough films, the DOS shows discrete steps instead of the smooth curve ($\propto \Omega^2$, where Omega is the phonon frequency) under a low-frequency approximation. When a phonon DOS step coincides with the superconducting gap edge, the size effect manifests as an anomalous peak of Q before it levels off with decreasing temperature. The Q reaches an unusual maximum because the inverse of quasiparticle lifetime is

proportional to the phonon DOS in the low-temperature approximation [126]. The reduction of phonon DOS below certain energies (before each jump on the phonon spectrum) may be utilized to reduce quasiparticles decay rate in thin Al layers for quantum circuits [127, 128].

Furthermore, the proximity effect will enhance the performance of resonators under magnetic fields. In our Al/Nb/Al trilayer structures, the Nb core layer can enhance the critical field and critical temperature of Al films through the proximity effect as Nb [40] is significantly higher on both parameters. Proximity effect will induce higher critical field, thereby suppressing the generation of vortices in the Al layers and reduce losses on the surfaces.

This chapter is organized as follows: A model of Q from the trilayer Al/Nb/Al resonators is introduced first, which considers the size effect of the thin cladding Al layers. The measured Q in 5/50/5 nm and 10/50/10 nm Al/Nb/Al heterostructures are compared in the following section. The Q from the 5/50/5 nm heterostructure has a clear peak at 1.2 K, which is due to the reduced surface losses from suppressed phonon DOS in the thin Al layers. The physical growth of Al/Nb/Al heterostructure and their structural characterization are discussed at last.

5.2 Results and discussion

5.2.1 Microwave losses induced by quasiparticle-lifetime broadening

To employ the suppressed phonon DOS in proximity enhanced Al/Nb/Al trilayer films, we build a model to show how the local phonon DOS in the thin Al layers could affect the resonator Q of the whole structure. The Q values may be affected by quasiparticles losses which are induced by the smearing of quasiparticles states at the gap energy edge. The response of a superconductor, when driven away from equilibrium in microwave frequency, is dependent upon the various electron relaxation times. Central to the relaxation phenomenon is the recombination time τ_R. In order to explain the lifetime-broadened energy gap edge, Dynes *et al.* proposed to add a parameter $j\Gamma_D$ ($j=\sqrt{-1}$) to quasiparticle energy E in the formula of excitation spectrum given by BCS theory $\rho(E,\Gamma_D)=\mathrm{Re}\{(E-j\Gamma_D)/[(E-j\Gamma_D)^2-\Delta^2]^{1/2}\}$ [129]. It was justified by Kaplan *et al.* that the parameter $2\Gamma_D$ could be interpreted as the inverse of the quasiparticle recombination lifetime [126]. Mitrovic *et al.* proposed an alternative form of the excitation spectrum by including a

complex gap energy $\Delta = \Delta_0 - j\Delta_2$ from the first principles [130]. Indeed, $\rho(E,\Gamma)$ is replaced by $\rho(E,\Delta_2) = \mathrm{Re}\{E/[E^2 - (\Delta_0 - j\Delta_2)^2]^{1/2}\}$ and $-2\,\mathrm{Im}\,\Delta(\mathbf{k}, E = \Delta_0)$ is equal to the inverse quasiparticle lifetime with $\mathbf{k}$ on the Fermi surface. It is well known that the imaginary part of the gap energy is nonzero at a finite temperature as a result of quasiparticle damping [131]. Per the modified formula for excitation spectrum, if Δ_2 becomes larger, there will be an increase in the gap smearing as shown in the inset of Figure 5.2(a). Defining $\theta \equiv \Delta_2/\Delta_0$, we plot the quasiparticle DOS at T=0K for $\theta_1 = 6\times10^{-4}$ and $\theta_2 = 10^{-4}$ from the upper curve to the lower curve in the inset, respectively. The values of θ are decided for the purpose of demonstrating the effect of a complex gap energy on the edge smearing. Thus, there is more density of states for quasiparticles inside the gap. The total density of quasiparticles near the gap will be increased, causing more losses.

5.2.2 Quasiparticle decay rate

The decay rate $2\Gamma(\omega)$ of a quasiparticle with energy ω is equal to $2\Gamma_s(\omega) + 2\Gamma_r(\omega)$, where $2\Gamma_s(\omega)$ corresponds to quasiparticle scattering processes with the emission or absorption of a phonon, and $2\Gamma_r(\omega)$ is the recombination rate corresponding to a process in which one quasiparticle recombines with another to form a Cooper pair with the excess energy emitted as a phonon. For quasiparticle scattering processes at low temperatures, the important phonon energies are near zero, not $2\Delta(0)$, so the change of phonon DOS for phonons with energies at gap edge has no impact on the scattering rate. On the other hand, according to the Eliashberg formulation [132], the expression for $2\Gamma_r(\omega)$ is [126]:

$$2\Gamma_r(\omega,T) \propto \frac{1}{1-f(\omega)}\int_{\omega+\Delta}^{\infty} d\Omega\,\alpha^2(\Omega)F(\Omega)\,\mathrm{Re}\left(\frac{\Omega-\omega}{[(\Omega-\omega)^2-\Delta^2]^{1/2}}\right)\left(1+\frac{\Delta^2}{\omega(\Omega-\omega)}\right)[n(\Omega)+1]\,f(\Omega-\omega), \tag{5.1}$$

where Ω is the energy of phonon, $2\Gamma_r(\omega)$ is related to the low-frequency part of the phonon DOS $F(\Omega)$ weighted by the square of the matrix element of the electron-phonon interactions $\alpha^2(\Omega)$, $f(\omega)$ and $n(\Omega)$ are the state occupations for quasiparticles and phonons, respectively. Hence, the

imaginary part Δ_2 of the complex gap energy Δ is obtained by (5.1), which is $\Delta_2 = \Gamma_r$. The proportional parameter in Eq. (5.1) is determined by fitting the calculations with experimental results. $f(\omega)$ is the sum of thermal occupation and an exponentially decaying occupation due to the non-equilibrium quasiparticles, $f(\omega) = 1/(1+e^{\omega/T}) + 1/(1+e^{\omega/T_0})$, where T_0 is a fitting parameter. The total state occupation for quasiparticles is then finite at zero temperature. As was pointed out by Martinis *et al.* [128], non-equilibrium quasiparticles are expected in a superconductor well below the critical temperature and result in finite state occupation $f(\omega)$ of quasiparticles even at very low temperatures. By assuming $\alpha^2(\Omega)$ to be constant in the vicinity of $\Omega = 2\Delta(T=0)$ for Al [126], the transition probability for this relaxation process should be nonzero at any finite temperature and is directly proportional to the phonon DOS at the gap edge.

5.2.3 Local phonon DOS

The local phonon DOS in a thin metal film backed by a semi-infinite metal substrate is close to that of an isolated metal film, except for some smearing on sharp structures [133]. In our case, the core Nb layer is indeed much thicker and heavier than the cladding Al layers. Thus, we can approximate the local DOS of the Al coating layers with that of isolated thin Al films with free boundary conditions. In a thin film, the phonon DOS gains discrete steps at characteristic energies [134]. Here we adopt the equation of motion for elastic vibrations in an anisotropic medium to calculate the local phonon DOS in the Al cladding layer [135],

$$\rho \frac{\partial^2 U_m}{\partial t^2} = \frac{\partial \sigma_{mn}}{\partial x_n} (m, n = 1, 2, 3), \tag{5.2}$$

where $\vec{U}(U_1, U_2, U_3)$ is the displacement vector, ρ is the mass density of the material, σ_{mn} is the elastic stress tensor given by $\sigma_{mn} = c_{mnkj} U_{kj}$. c_{mnkj} is the elastic module, and $U_{kj} = \frac{1}{2}(\frac{\partial U_k}{\partial x_j} + \frac{\partial U_j}{\partial x_k})$ is the strain tensor. We consider that Al layer is uniform along the X_3 axis.

The axis X_3 is assumed to be perpendicular to the superconducting film plane. Considering the Al is highly textured along [111] direction, we can reduce the number of subscript indexes in the

coefficients c_{mkkj}. We can write down the following equalities by adopting the two-index notations according to the prescription:

$$c_{1111} = c_{2222} = c_{11};\ c_{1122} = c_{12};\ c_{1133} = c_{13};$$
$$c_{3333} = c_{33};\ c_{1313} = c_{2323} = c_{44};\ c_{1212} = c_{66}; \tag{5.3}$$

Thus, we could have six independent elastic constants to characterize our highly-textured Al film. The specifics of Al lattice structure can be included in an anisotropic continuum model. We choose (X_1, X_2) as the plane where the three-layered structure is homogeneous, as is shown in Figure 5.1.

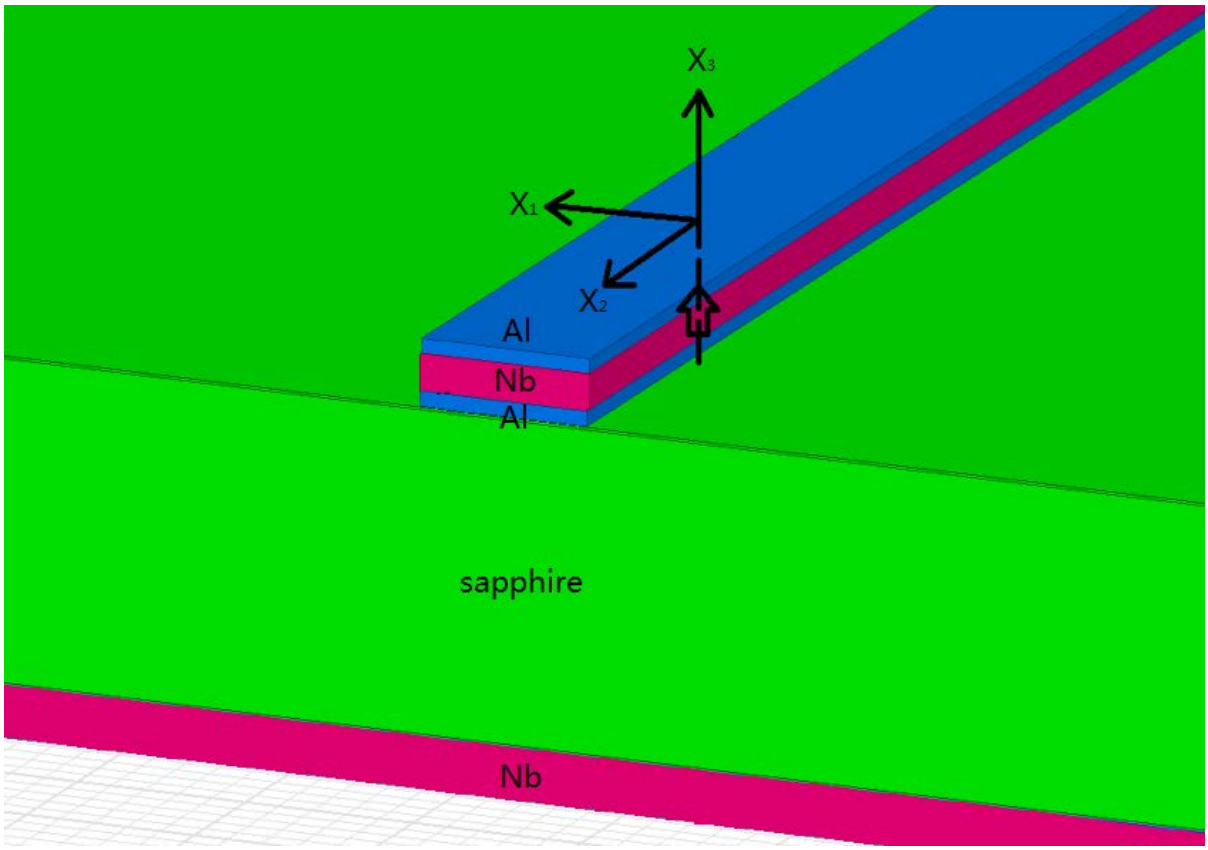

Figure 5.1: The structure of Al/Nb/Al tri-layer film. The coordinate is displayed in the graph.

Since the thickness of the tri-layered structure is approximately equal to the sound wavelength in Al and Nb, the propagation of the most phonons is parallel to the plane of the film. The axis X_1 is

assumed to be along the propagation direction of the acoustic waves. We look for the solution to the (5.2) in the following form

$$U_n(x_1, x_3, t) = u_n(x_3)e^{i(\omega t - kx_1)} \qquad (n = 1, 2, 3), \tag{5.4}$$

where u_n are the amplitudes of the displacement vector components, ω is the phonon frequency, k is the phonon wavevector and i is the imaginary unit. Let the thickness of Al layer be d_1, $x_3 \in [0, d_1]$.

The shear polarization, of which the displacement vector is parallel to the structure surfaces, can be distinguished from the others using the following definition

$$\rho \frac{\partial^2 U_2}{\partial t^2} = \frac{\partial \sigma_{2n}}{\partial x_n}. \tag{5.5}$$

By substituting (5.4) with $n = 2$ to (5.5) and taking into account (5.3), one can turn the partial differential equation (5.5) into an ordinary second order differential equation

$$-\rho\omega^2 u_2(x_3) = -c_{66}k^2 u_2(x_3) + c_{44}\frac{d^2 u_2(x_3)}{dx_3^2} \tag{5.6}$$

For the two other vibrational polarizations (n = 1, 3) with the displacement vector components U_1 and $U_3' = -iU_3$, we can get the system of two interrelated equations using (5.2) and (5.4). These equations are given as follows:

$$-\rho\omega^2 u_1(x_3) = -k^2 c_{11} u_1(x_3) + c_{44}\frac{d^2 u_1(x_3)}{dx_3^2} + k(c_{13} + c_{44})\frac{du_3'(x_3)}{dx_3}, \tag{5.7}$$

$$-\rho\omega^2 u_3'(x_3) = -k^2 c_{44} u_3'(x_3) + c_{33}\frac{d^2 u_3'(x_3)}{dx_3^2} - k(c_{13} + c_{44})\frac{du_1(x_3)}{dx_3}. \tag{5.8}$$

The film we consider is a 5 or 10 nm cladding Al layer. The two surfaces of an isolated Al layer is assumed to be free. As a result, the force components along all coordinate axes are equal to zero, i.e. $P_1 = P_2 = P_3 = 0$ where $P_n = \sigma_{nk} x_k'$ and $\vec{x}'$ is the vector normal to the surfaces of the film $\vec{x}' = (0, 0, x_3)$. The boundary condition for the shear modes is

$$P_2 = \frac{c_{44}}{2}\left(\frac{\partial U_2}{\partial x_3} + \frac{\partial U_3}{\partial x_2}\right) = \frac{c_{44}}{2}\frac{\partial U_2}{\partial x_3} = 0. \tag{5.9}$$

Using (5.4), the following relationship is satisfied

$$\frac{du_2}{dx_3} = 0 . \tag{5.10}$$

The boundary conditions for the two other vibrational modes are given as

$$P_1 = \frac{c_{44}}{2}\left(\frac{\partial U_1}{\partial x_3} + \frac{\partial U_3}{\partial x_1}\right) = 0 , \tag{5.11}$$

$$P_3 = c_{13}\frac{\partial U_1}{\partial x_1} + c_{33}\frac{\partial U_3}{\partial x_3} = 0 . \tag{5.12}$$

The following equations are satisfied for the boundary conditions on the surfaces of an isolated Al layer:

$$\frac{du_1}{dx_3} + ku_3' = 0 , \tag{5.13}$$

$$-kc_{13}u_1 + c_{33}\frac{du_3'}{dx_3} = 0 . \tag{5.14}$$

The equations of motions for elastic vibrations are numerically solved by finite difference method [136]. The total phonon DOS is obtained by summing over all phonon modes, $F(\Omega) = \frac{1}{2\pi}\sum_n k_n(\Omega)\frac{dk_n(\Omega)}{d\Omega}$ (n is the index of phonon modes). The material parameters used in our calculations are taken from the literature [137], and the calculations have considered that the Al layers in our actual heterostructure are oriented in the (111) direction.

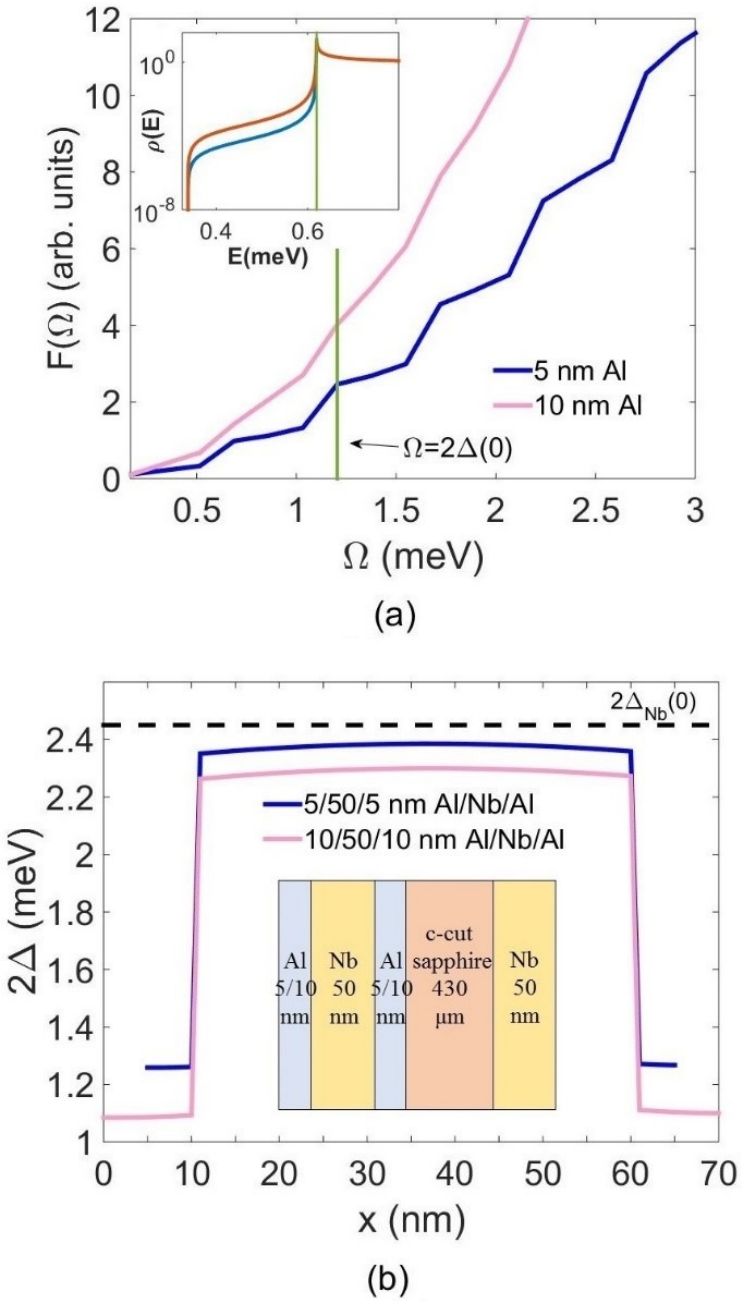

Figure 5.2 (a) Calculated total phonon density of states as a function of phonon energy for 5 nm and 10 nm Al films. The vertical line shows where the gap energy $2\Delta(0)$ for 5 nm Al in the heterostructure is located. The inset illustrates how quasiparticle DOS at T=1.2K broadens when θ varies from 10^{-4} (cyan curve) to 6×10^{-4} (red curve). The vertical line shows where the

quasiparticle energy equaling to $\Delta(0)$ for 5 nm Al in the heterostructure is located. (b) Calculated superconducting pair potential distribution with depth for 5/50/5 and 10/50/10 nm Al/Nb/Al heterostructure. The dashed line is the gap energy for a single 50 nm Nb layer determined from our experiment. The inset is the schematic illustration of the Al/Nb/Al heterostructure on a double-side-polished c-cut sapphire. The back side is coated with 50 nm Nb.

Figure 5.2 (a) shows the calculated phonon DOS for 5 nm and 10 nm Al thin films. In the 10 nm Al film, the phonon DOS shows a nearly smooth dispersion curve, which leads to a gradual increase in losses. On the other hand, the 5nm Al film clearly shows noticeable jumps in the phonon spectra due to the strong size effect. The inset in Figure 5.2(a) illustrates how the increasing theta can increase the sub-gap quasiparticle DOS. The imaginary part is increased from T=1.2K to T=0.2K. Because of a larger imaginary part of gap energy, there exist more quasiparticle DOS inside the gap which causes more losses at the lower temperature.

The pair potential defines the strength of BCS pairing interaction and is spatially dependent. Since the density of states in Al and Nb is modified due to the proximity effect [86, 110], the pair potential experiences strong variations along the thickness of the film. Though the pair potential at Al layer is lifted while the pair potential at Nb layer is lowered by proximity effect, it has a discontinuity at the interface between Al and Nb because the physical presence of interfaces ensures the presence of scattering centers. To clarify the effect of the local phonon DOS on quasiparticle induced losses, we calculate the local pair potential inside the 5 nm cladding Al film from the Usadel equations [73, 76]. The interface parameters between Al and Nb are assumed with literature values [138]. If the interfaces affect several atomic layers of both superconductors, the boundary conditions make the position dependence of pair potential look like steps as in Figure 5.2(b). The pair potential is 1.3 meV for 5 nm Al and 1.1 meV for 10 nm Al in the trilayer structure, which are close to the calculated values reported by Brammertz *et al.* [76] for a similar Al/Nb/Ta structure. The gap energy 1.3 meV matches the second phonon DOS jump in Figure 5.2(a). When the pair potential increases beyond the first phonon DOS jump with decreasing temperatures, the effect of sudden increased phonon DOS is shadowed by the fast reduction of quasiparticle population. As the quasiparticle population begins to level off at lower temperatures, the second

sudden jump of phonon DOS will result in a fast increase in losses when the gap edge falls upon the phonon steps. Therefore, by adjusting the thickness of the cladding Al layers, we can observe phonon induced Q variation with temperature.

5.2.4 Film characterization

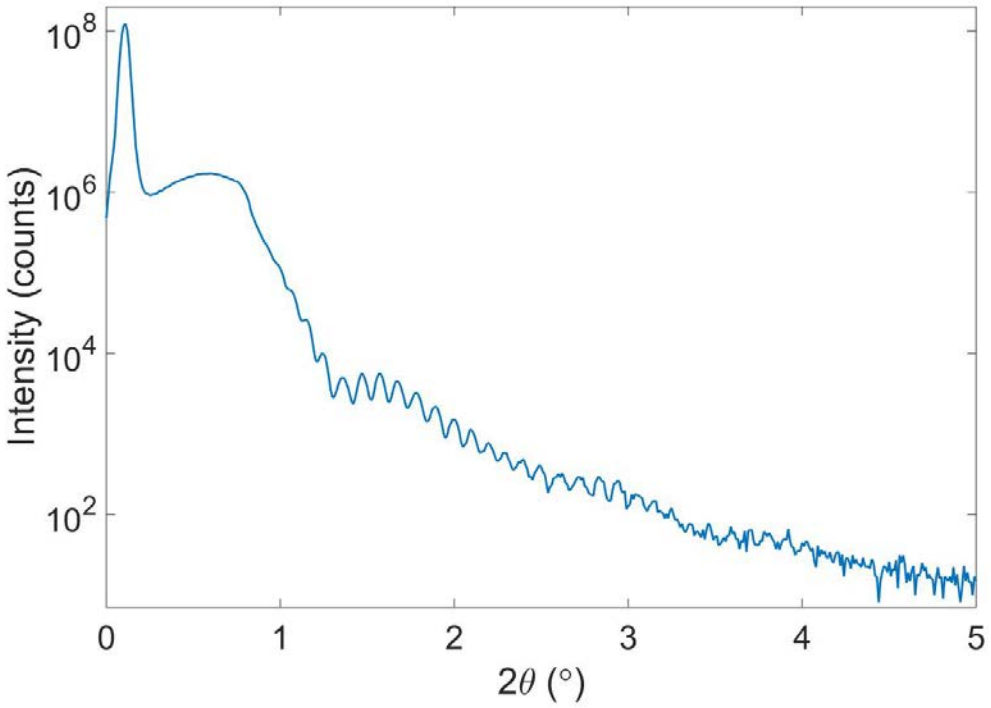

Figure 5.3: X-ray reflectivity (XRR) pattern for the 5/50/5 nm Al/Nb/Al trilayer film on the c-cut sapphire.

The structure of the composite film is based on Al/Nb/Al trilayer, as shown in the inset of Figure 5.2(b). The films were deposited on the front side of a double-side-polished sapphire wafer, while the back side of the wafer was coated with 50 nm pure Nb as the ground plane of the superconducting transmission line resonators. Pure Nb, deposited at room temperature without pre- and post-annealing, was chosen as the ground plane to avoid heating damage to the materials already present on the front side. The samples were deposited in a reactive magnetron sputtering

system (AJA International, USA) with the base pressure of 1×10^{-8} Torr. The substrates were first Ar-sputter cleaned for 5 minutes under substrate bias with 50W RF power, 5 milli-Torr chamber pressure and 30 sccm of Argon flow. Then they were annealed at $700^{\circ}C$ for 1 hour and cooled to room temperature before the actual film growth starts. The thickness of each layer is confirmed by fitting a tri-layer model with the data obtained from X-ray reflectivity pattern, which is shown in Figure 5.3.

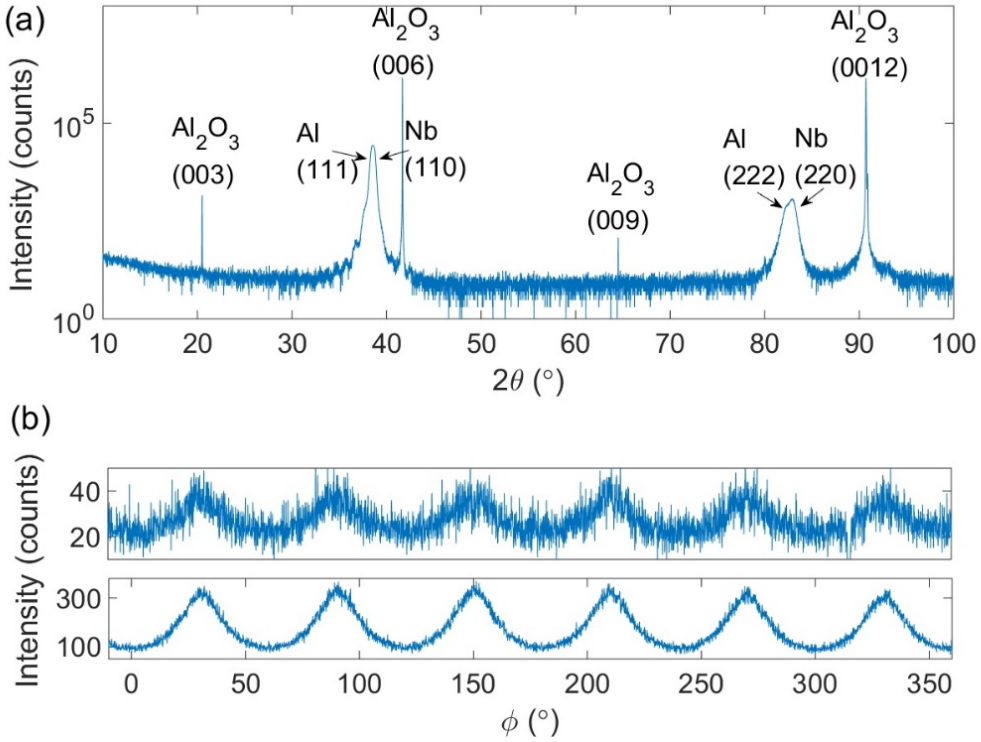

Figure 5.4: (a) High-resolution XRD pattern of the Al/Nb/Al trilayer film on the c-cut sapphire. (b) Azimuthal XRD data ("ϕ-scan") reveals the six-fold symmetry of the off-axis (200) reflections from Al and Nb, respectively.

X-ray diffraction (XRD) was used to study the crystal structures of the composite films grown on the c-cut sapphire. The measurement was carried out using a Bruker D8 Discover (Bruker AXS, Germany) system with a Cu K_α source. Figure 5.4(a) shows the high-resolution $2\theta-\omega$ scan of

the composite film. A 3-bounce monochromator was used in front of the source in addition to a Gobel mirror. Besides four extremely sharp peaks from the sapphire substrate, there are only peaks from Al (111) at 38.47^{o}, Nb (110) at 38.51^{o} and their second order diffractions. Al (111) and Nb (110) are so close that they cannot be well distinguished from each other, but the Al (222) and Nb (220) clearly revealed the presence of both peaks. The appearance of only Al {111} and Nb {110} peaks indicate that Al and Nb are both textured. Figure 5.4(b) is the azimuthal XRD data ("ϕ-scan") from the Al/Nb/Al composite film. The upper panel is the ϕ-scan for Al (200) by setting ψ at 54.7^{o} – the angle between Al (111) plane and Al (200) plane in an fcc structure. The detection angle 2θ was set at 44.74^{o} which is for Al (200) reflections. Fully epitaxial Al (111) should display three-fold symmetry in the ϕ-scan of (200) planes. The appearance of six peaks indicates two symmetrically equivalent growth orientations (twins) occur in the Al layers, as a result of stacking three-fold symmetric fcc structures onto the six-fold symmetric hcp substrate [139]. The lower panel of Figure 5.4(b) is the ϕ-scan for Nb (200) by setting ψ at 45^{o} - the angle between Nb (110) plane and Nb (200) plane in a bcc structure. The six-fold symmetry from Nb (200) can also be attributed to the twin growth of the bottom Al layer.

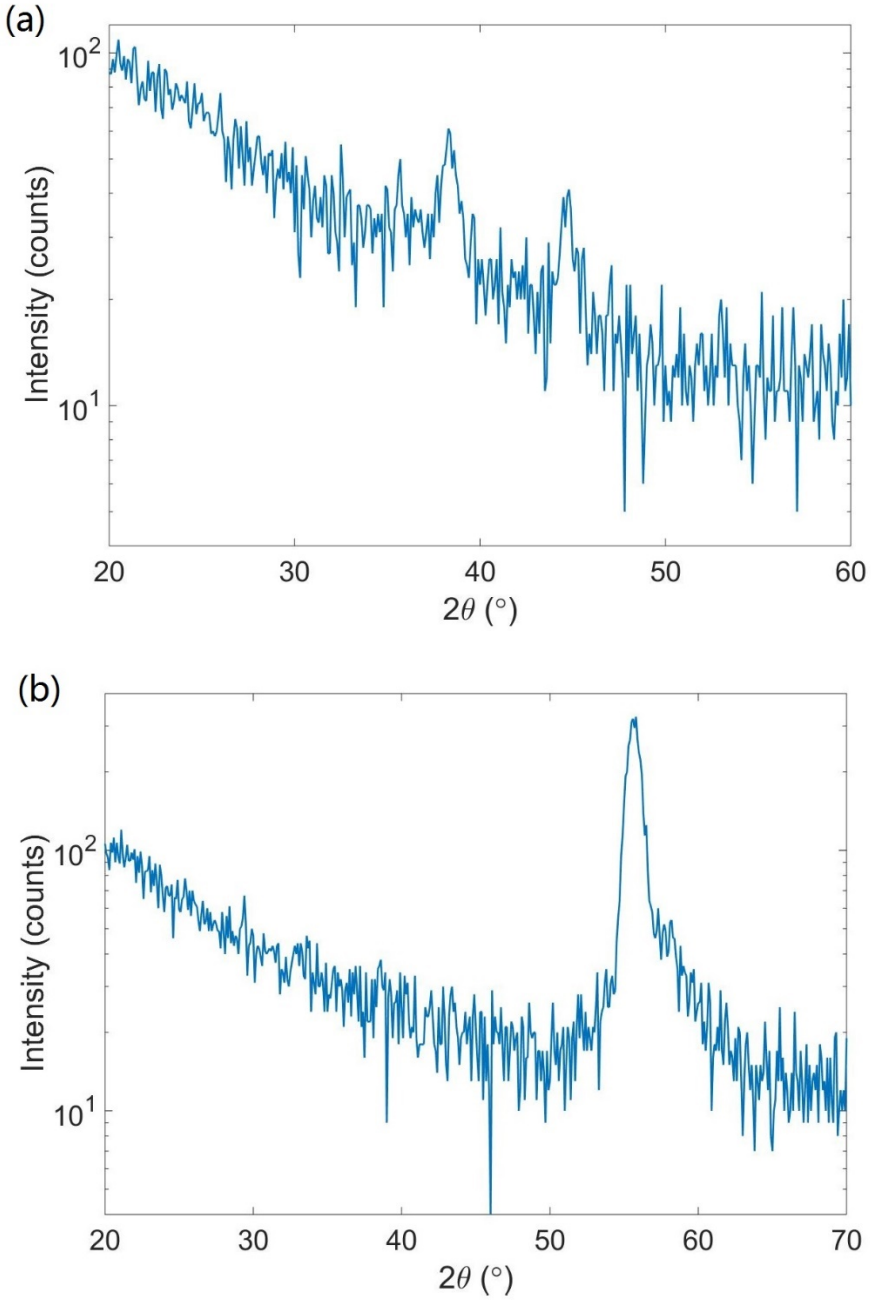

Figure 5.5: $2\theta-\omega$ **scans by fixing** $\phi=30^o$ **for Al/Nb/Al tri-layer film.** (a) $2\theta-\omega$ scans for Al (200) by setting $\psi=54.7^o$. (b) $2\theta-\omega$ scans for Nb (200) by setting $\psi=45^o$.

We also performed $2\theta-\omega$ scans by fixing ϕ at one of the off-axis peaks, such as 30^o in Figure 5.4(b). The results are shown in Figure 5.5. The Bragg diffractions confirmed the ϕ peaks come from 2θ of 44.7^o for Al and 55.5^o for Nb, well matching the Al (200) and Nb (200) reflections. It proves that the six-fold symmetry shown in Figure 5.4(b) indeed originates from the off-axis diffractions from Al (200) and Nb (200) planes. An additional peak at $2\theta = 38.3^o$ is observed in Figure 5.5(a), which corresponds to Al (111) plane. This peak may be explained by the fact that Al layer in the trilayer structure is texture.

5.2.5 Resonator measurement

We used optical lithography and reactive ion etching to fabricate the composite half-wavelength microstrip transmission line resonators [105] from these trilayer structures, as shown in Figure 5.6(a). Compared to 3D cavities, or coplanar waveguides (CPW), microstrip line resonators offer small mode volume and can produce homogeneous magnetic fields above the resonator at microwave frequency, and therefore are better suited for pulsed ESR based quantum circuits.

The resonator measurement was carried out in a closed-flow dilution refrigerator (Leiden Cryogenics BV, BA Leiden, Netherlands) with a vector network analyzer (Agilent N5230A) to record the transmission through our feedline, S_{21}. Every data point was obtained by averaging over measurements. The resulting Q as a function of temperature is presented in Figure 5.6(b). The filled circles and squares represent the Q for 5/50/5 nm and 10/50/10 nm Al/Nb/Al resonators, respectively, without external magnetic field. Both films show similar Q of 22000 at 1.2 K, and it is also the highest Q for the 5/50/5 nm resonator. The two samples behave very differently as the temperature lowers further. The resonator with 5 nm Al cladding layers has its Q slowly dropped to 20800 at 30 mK, while the other one shows gradually increased Q. The different behavior between 5/50/5 nm and 10/50/10 nm resonators can be explained by the size effect of the Al cladding layers. From the earlier discussions, the proximity-enhanced energy gap of the 5 nm Al layers is estimated to be $2\Delta(0) \approx 1.3$ meV. It happens to be right above the second phonon step as shown in Figure 5.2(a). As the temperature rises from 0 K, the gap gradually narrows. At a temperature T (1.2 K in this case), the gap edge moves below the phonon step, and the phonon

density dropped significantly leading to reduced loss and improved Q. As a comparison, the size effect for 10 nm Al layers is negligible. Therefore, the 10/50/10 nm Al/Nb/Al resonator shows continuously decreasing Q as the temperature goes up, while the 5/50/5 nm resonator has an anomalously increased Q around 1.2 K. It is noted that Martinis *et al.* [128] observed an improvement in quasiparticle damping when tuning the temperature for superconducting qubits. The unusual reduction in damping rate is explained with the redistribution of the state occupation $f(\omega)$ for non-equilibrium quasiparticles as temperature decreases. In our experiments, 5/50/5 nm and 10/50/10 nm Al/Nb/Al trilayer films have almost same gap energy and are grown on the same kind of substrates. The resonators with same design were also measured in the same environment. We can further deduce from the Figure 5.6 that the devices suffer from the same non-equilibrium quasiparticle density as the Q values begin to level off at the same temperature T=1.2K. Only by the changes in $f(\omega)$ cannot the experimental results for 10/50/10 nm and 5/50/5 nm resonators be explained at the same time. Indeed, both of $f(\omega)$ and $F(\Omega)$ will affect quasiparticle damping rate. Thus, they may cause the same unusual peak as observed in experiments.

We can more quantitatively model the Q in our resonators with surface impedance calculations [140]. The trilayer structure can be treated as the cascade of three single-layer films, and the total surface impedance can be evaluated by concatenating the surface impedance of each layer through the traditional transmission line theory. The solid lines shown in Figure 5.6(b) are the best fit obtained with this model. Without external magnetic fields applied, resonators with Al cladding showed clearly enhanced performance over resonators with only 50 nm Nb fabricated in the same way ($Q \approx 15000$). Pure Al does have better resonator performance than pure Nb in zero fields, and our Al cladding allows a significant portion of microwaves to transport in the surface Al layers instead of the core Nb layer.

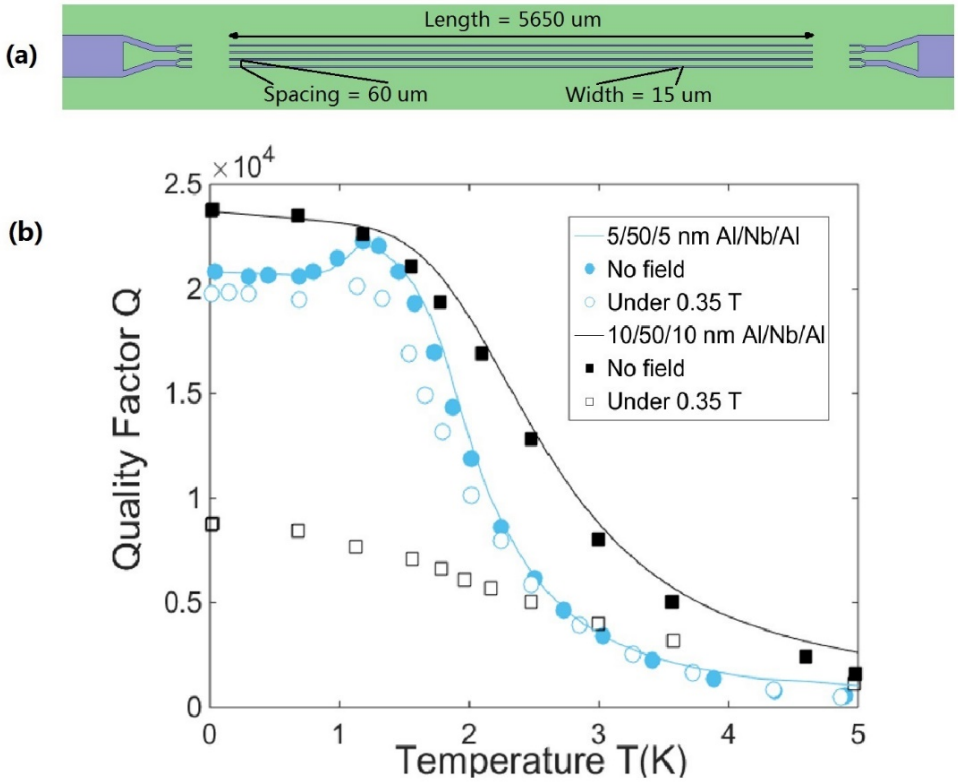

Figure 5.6: (a) Layout of the resonator device. It consists of four parallel $\lambda/2$ microstrip line resonators separated by 60 μm. Each $\lambda/2$-resonator is 5650 μm long, 15 μm wide. (b) The Q values of 5/50/5 nm and 10/50/10 nm Al/Nb/Al trilayer structures. The filled circles and squares are measured values for 5/50/5 and 10/50/10 Al/Nb/Al resonators without external fields; the empty circles and squares are measured values under a 0.35T in-plane field. The solid lines are fitted curves from our model.

When an in-plane magnetic field of $B_0 = 0.35\,\mathrm{T}$ is applied in parallel to the resonator lines, both resonators show lower Q than in the zero-field situation because of weakened pairing. For the 10/50/10 Al/Nb/Al sample, maximum Q significantly drops from 23800 to 8800. The proximity effect between Nb and Al may not be robust enough to enhance the 10 nm Al layers entirely, and thicker Al layers are also more susceptible to vortices formation. Therefore, it performs worse than the device with thinner Al cladding layers. The 5/10/5 Al/Nb/Al device maintains Q as high as

19800 at 15 mK and the maximum Q = 20100 at 1.2 K when a $B = 0.35$ T field is applied. Compared with the case of zero magnetic fields, the Q is only moderately decreased because of a small reduced-field (for 50nm Nb thin film, the reduced-field is $B_0 / B_{c2}(0) \approx 0.1$ [22]). The peak Q at 1.2 K drops slightly larger than the Q at lowest temperatures. This is due to the losses generated by the movement of quasiparticles at a higher temperature (>1K). Nevertheless, this result has surpassed the previously reported best results of 6000 on 400 nm Nb resonators [105] and 15000 on 50 nm Nb resonators under the same magnetic field with the same resonator design.

In this work, we identified the effects of local phonon DOS on the performance of the proximity-enhanced Al/Nb/Al trilayer resonators. We modeled and observed an unusual increase in Q with temperature when the superconductor gap edge moves below a phonon DOS step. Moreover, Q values higher than 20000 were achieved under a 0.35T in-plane magnetic field, making them suitable for operations when magnetic fields are necessary.

5.3 Summary

In this research, we tailor the phonon density of states (DOS) in thin superconducting films to suppress quasiparticle losses. We examine a model system of a proximity-enhanced three-layered Al/Nb/Al heterostructure and show that the local quantized phonon spectrum of the ultrathin Al cladding layers in the heterostructure has a pronounced effect on the superconducting resonator's quality factors. Instead of a monotonic increase of quality factors with decreasing temperatures, we observe the quality factor reaches a maximum at 1.2K in 5/50/5 nm Al/Nb/Al microstrip resonators, because of a quantized phonon ladder. The phonon DOS may be engineered to enhance the performance of quantum devices.

Chapter 6

Robust surface code topology against sparse fabrication defects

6.1 Introduction

Superconducting qubits are becoming the most popular choice in the practical implementation of quantum information processing, especially with quantum error correction [3, 141, 142]. Topological planar codes, in particular, the surface codes [143-145], are some of the most promising approaches to building a universal quantum computer. One advantage of surface codes is their relatively high tolerance to local errors, as first described by Preskill *et al*. [146]. The tolerance of surface codes to errors, with a per-operation error rate as high as 1% [147, 148], is far less stringent than other quantum computational approaches. For example, a theoretical analysis on the error tolerance of the Steane and Bacon-Shor codes, implemented on two-dimensional lattices with nearest-neighbor coupling, found per-operation thresholds of about 2×10^{-5} [149, 150]. Hence their safe operation demands three orders of magnitude lower error rates than the surface codes.

However, the price paid for the high error tolerance is that the implementation of surface codes requires a large number of physical qubits, as do many other approaches of error correction [149, 150]. It takes a minimum of 13 physical qubits to implement a single logical qubit. A reasonably fault-tolerant logical qubit that can be effectively applied in a surface code requires an order of 10^3 to 10^4 physical qubits [151]. As the size of the superconducting qubit array grows larger and larger, some qubits in the large array will inevitably fail in the fabrication processes. For example, the quantum annealing processor composed of 128 superconducting flux qubits ended up with 108 working qubits [152]. To implement the surface codes successfully, failed physical qubits have to be isolated by disconnecting the couplings between faulty qubits and functional ones. For a block of failed physical qubits, we can abandon the whole affected area. However, defective physical qubits that are scattered across the whole two-dimensional (2D) array cannot all be turned off. Although logical qubits in surface codes can be arbitrarily defined in the whole array of qubits, the holes left behind by sporadic failed physical qubits will affect all the steps of the surface codes

implementation. They may reduce the accessible area of the array, disrupt the error correction from existing syndromes, destabilize the logical qubits, limit the scaling of logical qubits, as well as hinder the movement of logical qubits.

In this thesis, we introduce a robust surface code topology which can amend sporadic fabrication defects. The topology is based on a virtual sub-lattice structure which is similar to the leakage-resilient version of the surface-code-based superconducting architecture proposed by Ghosh and Fowler [153]. Our implementation layout is a two-dimensional array of unit cells. Each unit cell is a complete graph K_n consisting of n physical qubits. The 2D array of qubits can be viewed as a folded disk with *n* layers. Scattered defective qubits (density ≤ 1 per unit cell) can be swapped with the spare qubits in the same cell and then cast onto a designated sacrificial layer of the topology. The whole layer full of holes left by defective physical qubits can be readily discarded. In this method, we can maintain a large defect-free surface composed of several layers of workable physical qubits.

The remaining part of the article is organized as follows. In Sec. 6.2, we first analyze the impact of faulty physical qubits on the implementation of surface codes, and then we propose a robust topology for the surface codes error correction, which is resilient to such fabrication errors. The detailed implementation of the proposed topology is described. In Sec. 6.4, we introduce two schemes to realize this topology: an array of flux qubits which can be coupled by ferromagnetic coupling, and an array of Xmon qubits with tunable inductive couplers. For the scheme of Xmon qubits, we propose a modified quantum circuit of the stabilization cycle to realize the robust topology. Next, we calculate and compare the per-operation error thresholds for the two schemes. The realization of the intersecting connections between qubits on the circuit level will also be discussed.

6.2 Robust surface code topology

6.2.1 Impact of a faulty physical lattice

Surface codes are robust against random local errors on physical qubits, but the method is not resistant to fabrication defects or physically failed qubits in many cases.

Firstly, the success of decoding syndromes relies on the fact that an error chain *E* is homotopic to a corrected chain *E'* and they belong to the same element in the fundamental group as shown in the left part of Figure 6.1(a). For an error chain *E* with given measure-*Z* syndromes Syn1 and Syn2, we choose any minimum distance recovery *E'* with $\partial E = \partial E'$. When applying $\hat{X}$'s to all the data qubits on *E'*, the product $D = EE'$ should be $\partial D = 0$, a trivial element of the first homology group or the first co-homology group, which means the 1-cycle or 1-cocycle is homologically equivalent to the null cycle or null cocycle. Since the first homology group and first co-homology group are both isomorphic to the group Z_2, a failed qubit will change a trivial cycle loop into a nontrivial loop as shown in the right part of Figure 6.1(a). Thereby the product *D* acts nontrivially on the code space, with $\partial D \neq 0$, rendering the error correction ineffective.

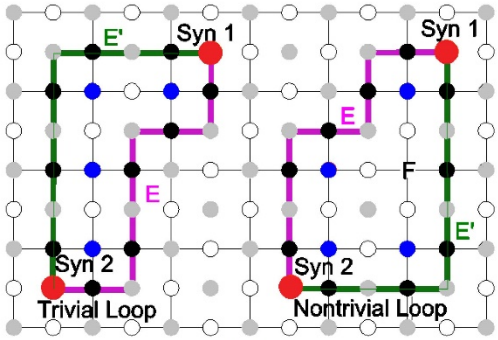
E'
Syn 1
Syn 1
E
E
F
E'
Syn 2
Syn 2
Trivial Loop
Nontrivial Loop

(a)

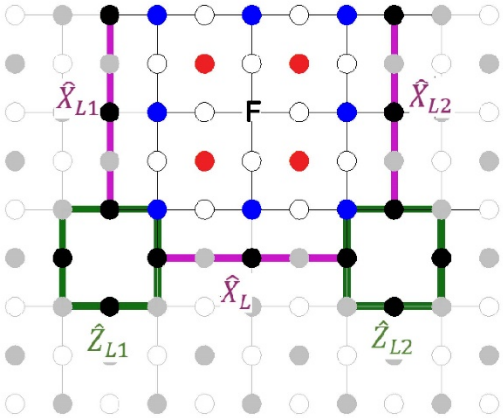
$\hat{X}_{L1}$
F
$\hat{X}_{L2}$
$\hat{X}_L$
$\hat{Z}_{L1}$
$\hat{Z}_{L2}$

(b)

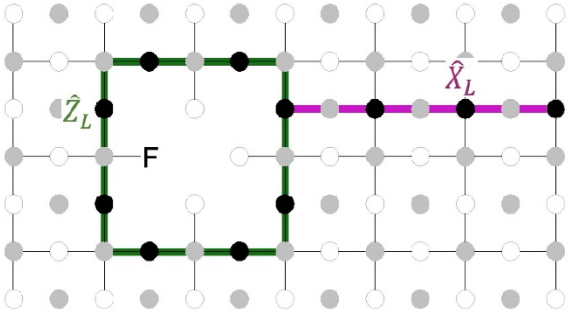
$\hat{Z}_L$
$\hat{X}_L$
F

(c)

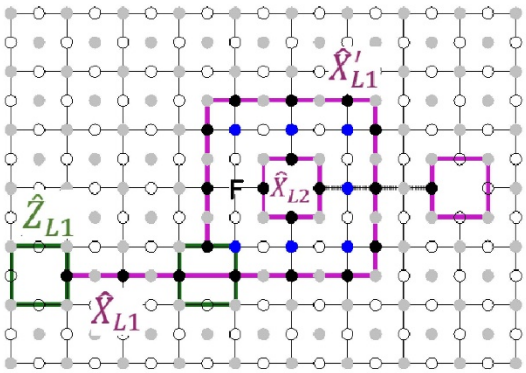
$\hat{X}'_{L1}$
F
$\hat{X}_{L2}$
$\hat{Z}_{L1}$
$\hat{X}_{L1}$

(d)

Figure 6.1: Four cases in which the implementation of surface codes error correction is disrupted by the appearance of faulty physical qubits. For each square unit, circles on the edges represent data qubits, dots on the lattice vertexes stand for measure-*X* qubits, and dots in the plaquettes are measure-*Z* qubits. Capital letter F is a failed physical qubit. (a) A faulty qubit invalidates the decoding and correcting processes for the surface codes. (b) A failed physical qubit makes an $\hat{X}_L$ operator for a double z-cut logical qubit ineffective. (c) A defective physical qubit destroys a z-cut logical qubit with a five-stabilizer hole. (d) A flawed measure-*X* qubit leaves an unacceptable hole in the enclosed stabilized cells and fails a logical controlled-NOT (CNOT) operator.

Secondly, in a defect-based surface code, a logical qubit is composed of one or two cut holes created by turning off a certain number of measure-*Z* qubits and measure-*X* qubits. For a single cut logical qubit, a defective physical qubit may induce unwanted degrees of freedom so that the desired logical qubit is no longer stabilized. For a double cut logical qubit, the logical operator $\hat{X}_L$ or $\hat{Z}_L$ cannot manipulate the two-qubit holes in a correlated fashion in the presence of any dysfunctional measure qubits. For example, in Figure 6.1(b), the logical $\hat{X}_L$ for a double z-cut qubit is the operator chain linking the internal $\hat{X}$ boundary of the left qubit to the internal $\hat{X}$ boundary of the right qubit. It replaces the operator $\hat{X}_{L1}\hat{X}_{L2}$ which is the product of the logical operators for each single z-cut logical qubit. The product $\hat{X}_L\hat{X}_{L1}\hat{X}_{L2}$ is equal to the product of all the $\hat{X}$ stabilizers enclosed by these three operators [these stabilizers are represented by blue circles in Figure 6.1(b)]. If some of the measure qubits fail, the product $\hat{X}_L\hat{X}_{L1}\hat{X}_{L2}$ is no longer equal to the product of all the stabilizers in the enclosed array and $\hat{X}_L$ is not equivalent to $\hat{X}_{L1}\hat{X}_{L2}$ within ± 1. Thereby the logical operator $\hat{X}_L$ is not accurately established.

Thirdly, the internal data qubits in a multi-cell hole of a logical qubit have to be measured for error tracking during the logical qubit operations. A Z-cut qubit with a five-stabilizer hole is shown in Figure 6.1(c). Failed physical qubits may cause failure of the error correction of the logical qubits and affect the size of the multi-cell hole in the logical qubit.

Fourthly, moving the hole of a fist logical qubit around another hole of a second logical qubit on the 2D array to entangle them is an essential functionality of the surface codes. This operation is called braiding. On the path of the movement, the measurement qubits have to be turned off and on sequentially, thereby no failed qubit is allowed on the path for a successful movement. In addition, a braid is equivalent to a CNOT operator in the sense that it can transform all the 16 possible two-qubit operator combinations correctly, such as $\hat{X}_{L1} \otimes \hat{I}_{L2} \rightarrow \hat{X}_{L1} \otimes \hat{X}_{L2}$. If a flawed measure qubit appears within the area enclosed by the motion trail, the expected logical gate operator will fail. For example, a braid of a Z-cut logical qubit around another X-cut qubit is shown in Figure 6.1(d). The original $\hat{X}_{L1}$ operator is extended in length to $\hat{X}'_{L1}$ along the moving trail. $\hat{X}'_{L1}$ includes the original chain linking the two-qubit holes plus a closed loop of operators. The loop part of the operator $\hat{X}'_{L1}$ should be moved through the enclosed stabilized cells by $\hat{X}$ operators. The loop of $\hat{X}$ data qubit operators is equivalent to a $\hat{X}_{L2}$ on the second qubit. The appearance of a flawed measure-X qubit denoted by 'F' will leave a hole among the enclosed stabilized cells and fail the expected logical operation. Furthermore, faulty physical qubits may induce decoherence onto its neighboring qubits if no isolation circuits are adopted.

6.2.2 Implementation of the robust topology

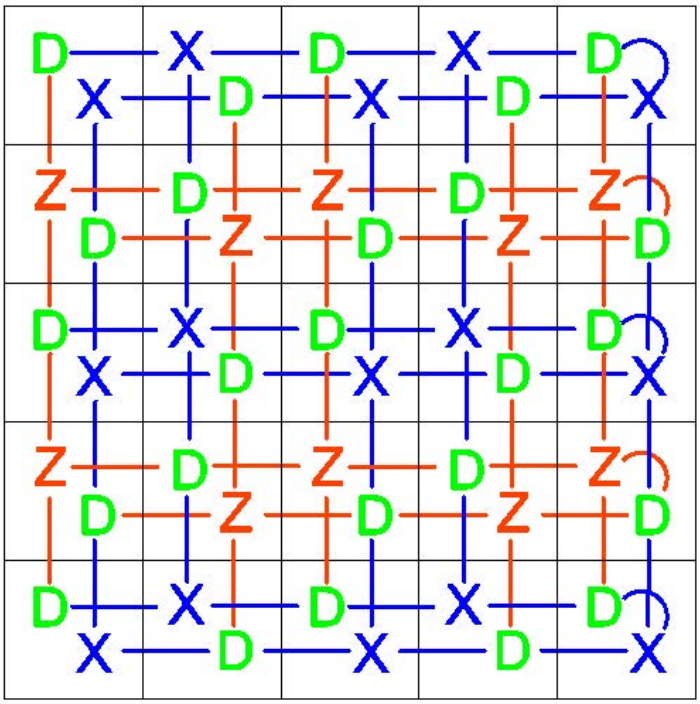

Figure 6.2: The robust surface code topology layout. Capital letter D stands for a data qubit; X means a measure-X qubit; Z denotes a measure-Z qubit. Each unit cell is a complete graph K_2 consisting of two physical qubits. Intra-cell couplings on the far right side connect the two otherwise independent qubit layers into a folded topology.

To implement the surface codes more successfully, we introduce a robust topology against failed physical qubits. Our defect-tolerant circuit is designed on a two-dimensional array of unit cells as shown in Figure 6.2. Capital letter **D** stands for a data qubit; **X** means a measure-X qubit, and **Z** denotes a measure-Z qubit. For simplicity, each unit cell is a complete graph K_2 consisting of two physical qubits. Both qubits in a cell are connected with each other by intracell couplings. Each qubit is further connected to four same-type qubits located in the four nearest-neighbor cells by intercell couplings. The couplings can be turned off to isolate the two qubits from each other. By switching on every intercell coupling and turning off all the intra-cell couplings except the ones at the right-side boundary of the array Figure 6.2, the topology can be viewed as a disk folded in two.

The coordinate of a physical qubit is denoted by (i, j, k), where i and j represent the position of the qubit's unit cell within the array, and k is the qubit's layer number within the cell. For example, the qubit from the second layer in the top left cell of the topology is labeled (1,1,2). Let (m, n) be the coordinate of a qubit in a planar square lattice for the surface codes. In addition, we denote X, Y as the planar square lattice structure and the folded structure for the surface codes, respectively. We can easily find a function $f : X(i, j) \to Y(i, j, k)$, where f is a bijection, continuous over X and f^{-1} is continuous over Y. Thereby our folded structure is homeomorphic to the planar square lattice structure. All logical qubits and operations defined in the folded structure are the same as those in the planar structure.

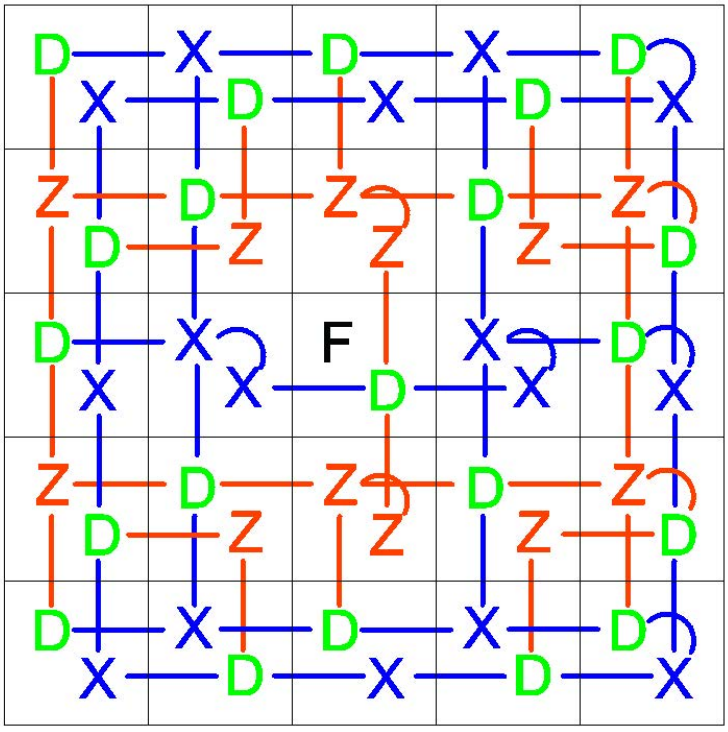

Figure 6.3: A faulty data qubit indicated by a black 'F' is isolated from the rest of the array. It is replaced by another functional qubit in the same cell.

A defective qubit can be replaced by another functional qubit in the same cell. Suppose that a data qubit in the first layer (3,3,1) is defective as shown in Figure 6.3. To prevent the failed qubit from affecting other qubits in the array, we turn off all the couplings connected to it. The intra-cell couplings between the two qubits in the four nearest-neighbor cells should be turned on. In Figure 6.3, we switch on the couplings between the qubits (2,3,1) and (2,3,2), (4,3,1) and (4,3,2), (3,2,1) and (3,2,2), and (3,4,1) and (3,4,2). Each pair of qubits coupled by the intracell couplings correspond to either a measure-*Z* qubit or a measure-*X* qubit, and together they are used as bridges to connect the qubits in the first layer of the surrounding cells and the replacement qubit in the second layer. This spare qubit replaces the failed one in the first layer and now functions as a data qubit. After the replacement, there is a cross-shaped empty area left behind in the second layer. The benefit of this robust topology is that all the faulty qubits in one layer can be swapped to other layers and preserve an intact layer of qubits for quantum error correction. Furthermore, when all the defect qubits are collected into one designated defect layer (readily achievable as long as the defect density is ≤ 1 per unit cell), the rest layers remain defect-free and can be coupled to form a large folded lattice structure so that the functional units are well utilized.

6.3 $\hat{Z}$ and $\hat{X}$ stabilizer circuits

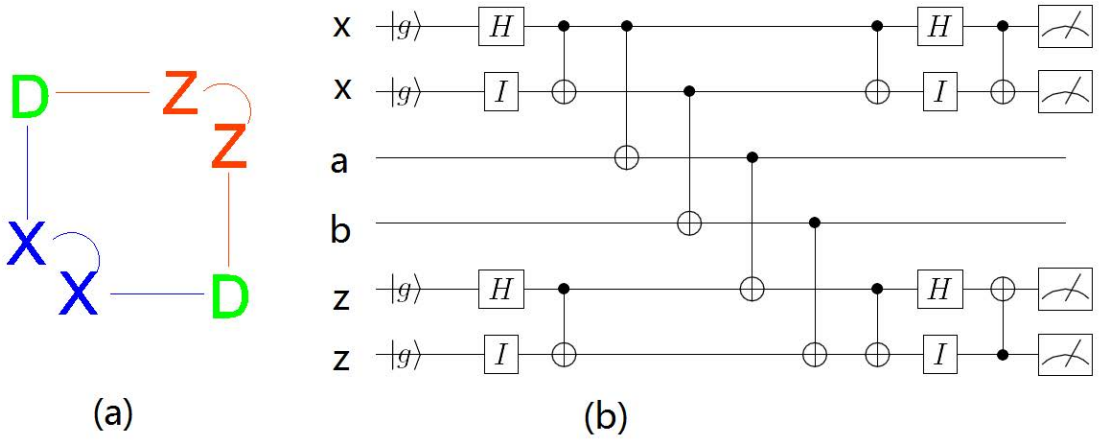

Figure 6.4: (a) The schematic graph of a unit cell consisting of two data qubits, one measure-*X* qubit, and one measure-*Z* qubit. (b) The quantum circuits for one stabilization cycle for the unit cell.

To further explain the operations of the *Z* and *X* stabilizers in the case of logical measure qubits coupled by quantum circuits, we walk through the quantum circuits of a system with just two data qubits, *a* and *b*, stabilized by one logical measure-*Z* and one logical measure-*X*. Its generalization to the full four-qubit stabilization is straightforward. The simplified layout and corresponding stabilizer circuits are shown in Fig. 6, which now involve two CNOT gates for each logical measure-*X* and logical measure-*Z*.

The circuit stabilizes the two data qubits *a* and *b* in a simultaneous eigenstate of $\hat{X}_a\hat{X}_b$ and $\hat{Z}_a\hat{Z}_b$, which is one of the four Bell states. The measurement outcomes from the same pair of measure qubits are the same as each other and correspond to the eigenvalues ± 1. We use an arbitrary entangled state of the two data qubits as an input to the circuit. The two qubits corresponding to a logical measure-*X* will be entangled during the first stage, as well as the two corresponding to a logical measure-*Z*. The next four CNOT gates will entangle all the qubits together. We denote the quantum states in the form $|\Psi_{x1}\Psi_{x2}\rangle \otimes |\Psi_a\Psi_b\rangle \otimes |\Psi_{z1}\Psi_{z2}\rangle$: the first two elements are the state of the measure-*X* qubits, the third and fourth are the states of data qubits *a* and *b*, respectively, and the last two are the states of the measure-*Z* qubits.

The input state to the circuit is in the form:

$$|\Psi_1\rangle = |gg\rangle \otimes (A|gg\rangle + B|ge\rangle + C|eg\rangle + D|ee\rangle) \otimes |gg\rangle. \tag{6.1}$$

After the first stage, the state of all the qubits becomes

$$|\Psi_2\rangle = (|gg\rangle + |ee\rangle) \otimes (A|gg\rangle + B|ge\rangle + C|eg\rangle + D|ee\rangle) \otimes (|gg\rangle + |ee\rangle). \tag{6.2}$$

Four CNOT gates are performed subsequently between the measure qubits and data qubits. Two CNOTs have the measure-*X* as the control qubits and the data qubits as the target qubits. The other two have the data qubits as the control qubits and the measure-*Z* as the target qubits. After the second stage, the state of this small system evolves to

$$\begin{aligned} |\Psi_3\rangle = {} & |gg\rangle \otimes (A|gg\rangle + D|ee\rangle) \otimes (|gg\rangle + |ee\rangle) \\ & + |gg\rangle \otimes (B|ge\rangle + C|eg\rangle) \otimes (|eg\rangle + |ge\rangle) \\ & + |ee\rangle \otimes (A|ee\rangle + D|gg\rangle) \otimes (|gg\rangle + |ee\rangle) \\ & + |ee\rangle \otimes (B|eg\rangle + C|ge\rangle) \otimes (|eg\rangle + |ge\rangle). \end{aligned} \tag{6.3}$$

Before we conduct the final projective measurement, we apply the final stage operations on the measure qubits. The state of the six physical qubits before the final measurement is

$$\begin{aligned}|\Psi_4\rangle = &(A+D)|gg\rangle\otimes(|gg\rangle+|ee\rangle)\otimes|gg\rangle \\ &+(A-D)|ee\rangle\otimes(|gg\rangle-|ee\rangle)\otimes|gg\rangle \\ &+(B+C)|gg\rangle\otimes(|ge\rangle+|eg\rangle)\otimes|ee\rangle \\ &+(B-C)|ee\rangle\otimes(|ge\rangle-|eg\rangle)\otimes|ee\rangle.\end{aligned} \tag{6.4}$$

6.4 Realization of the robust topology

6.4.1 Two schemes

The key to success lies in the fine-tuned operation of the logical measure qubits. We consider two schemes of coupling two physical qubits as one logical measure qubit bridging two different layers.

An array of scalable compound-compound Josephson junction (CCJJ) flux qubits [154] coupled by inductively tunable couplers [155, 156] is one option. It is possible to continuously tune the induced coupling from anti-ferromagnetic to ferromagnetic. Two physical flux qubits located in the same cell are coupled by ferromagnetic coupling J_{ij} and form a logical qubit. The Hamiltonian is $H=\sigma_{z1}+\sigma_{z2}+J_{12}\sigma_{z1}\sigma_{z2}$, where $J_{12}=-1$. By making use of ferromagnetic coupling between qubits, the proposed topology composed of an array of the complete graph K_4 can be readily mapped onto a square lattice structure of complete bipartite graphs $K_{4,4}$. Each unit cell of $K_{4,4}$ consists of four logical qubits, which can be used to realize our robust surface code topology.

A chain of Xmon qubits [157] coupled with direct capacitors have been shown to satisfy the error correction code threshold [3]. By replacing the direct capacitive coupling with fast tunable coupler [158], a logical measure qubit can be defined with quantum gates including Hadamard and CNOT gates. The complete stabilization cycles have to be modified for a logical measure-*X* qubit and a logical measure-*Z* qubit as shown in Figure 6.5. Every stabilization cycle consists of three stages. The first stage includes step 1 to step 3. Two physical qubits corresponding to a logical qubit are initialized in their ground state $|gg\rangle$, and then the pair is entangled into the Bell state

$\frac{1}{\sqrt{2}}(|gg\rangle+|ee\rangle)$ with a Hadamard gate and a CNOT gate (where $|g\rangle$ and $|e\rangle$ are the computational bases for the qubit). Step 4 to step 6 are the second stage. The two physical qubits require four CNOT operations to be coupled to their four nearest-neighbor data qubits. For the measure-*X* stabilization, each of the four CNOT gates targets one of the four data qubits with one of the two measure qubits as the control. For the measure-*Z* operation, every CNOT operation targets one of the two measure qubits with one of the four data qubits as the control. It is noted that step 6 includes two simultaneous CNOT operations on two different pairs of qubits. Before the final projective measurement, we apply two CNOTs and a Hadamard gate to ensure that the two physical measure qubits do act as one logical qubit, of which the readouts are the same; the projective measurement yields an eigenstate of $\hat{X}_a\hat{X}_b\hat{X}_c\hat{X}_d$ for the case of $\hat{X}$ stabilizer and an eigenstate of $\hat{Z}_a\hat{Z}_b\hat{Z}_c\hat{Z}_d$ for the case of $\hat{Z}$ stabilizer. Hence, after the projective measurement of all the measure qubits in the array, the state $|\Psi\rangle$ of all the data qubits simultaneously satisfies $\hat{Z}_a\hat{Z}_b\hat{Z}_c\hat{Z}_d|\Psi\rangle = Z_{abcd}|\Psi\rangle$, with eigenvalues $Z_{abcd}=\pm1$, and $\hat{X}_a\hat{X}_b\hat{X}_c\hat{X}_d|\Psi\rangle = X_{abcd}|\Psi\rangle$ with eigenvalues $X_{abcd}=\pm1$. It should be noted that two data qubits of different layers cannot be directly coupled by quantum gates to bridge the first layer and the second layer. In case a measure qubit happens to fail, the bridges connecting physical qubits across layers should be placed at the four next-nearest-neighbor cells instead of the four nearest-neighboring cells.

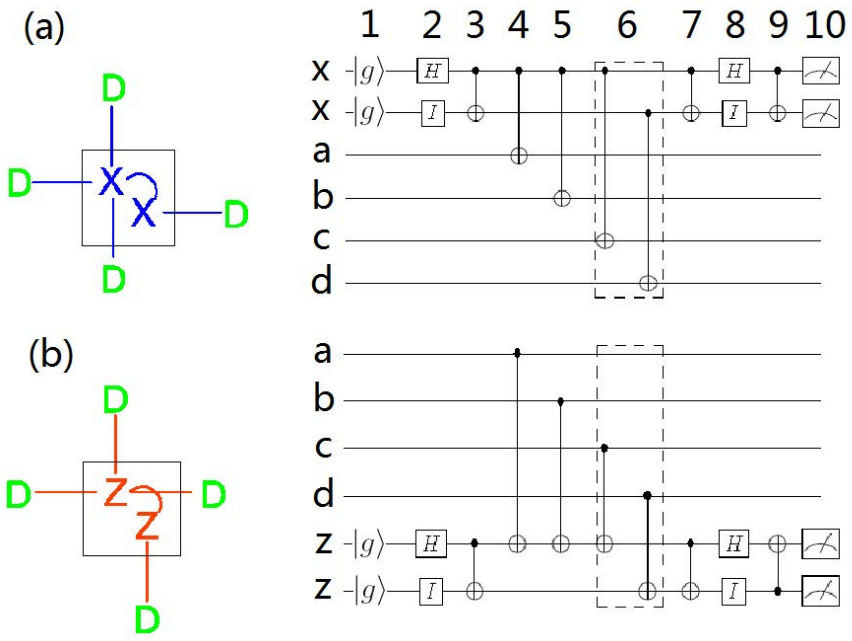

Figure 6.5: (a) The schematic graph of a logical measure-*X* qubit connected with four nearest-neighbor data qubits. The corresponding quantum circuits for one stabilization cycle are shown on the right. (b) The schematic graph and the corresponding quantum circuits for the case of a logical measure-*Z* qubit connected with four nearest-neighbor data qubits.

6.4.2 Comparison of error thresholds

Next, we compare the per-operation error threshold for an array of flux qubits with an array of Xmon qubits. For measure qubits coupled by ferromagnetic coupling, the measurement circuits do not need modification. Therefore, the per-operation error threshold for the surface code is not different from that of the planar square-lattice. Meanwhile, logical measurement qubits with nonferromagnetic coupling require additional CNOT and Hadamard gates to finish the stabilizer measurement circuits. Involving more steps will surely lower the per-step error threshold. Using the minimum weight perfect matching algorithm [159, 160], we can calculate the different per-step error thresholds of these two types of coupling. We consider the following errors:

(1). To perform a data qubit identity $\hat{I}$, but instead applied one of the single-qubit operations $\hat{X}$, $\hat{Y}$, or $\hat{Z}$, each occurring with probability $p/3$;

(2). To initialize a qubit to $|g\rangle$, but instead prepared $|e\rangle$ with probability *p*;

(3). To perform a measure qubit Hadamard operation $\hat{H}$, but in addition performed one of the single-qubit operations $\hat{X}$, $\hat{Y}$, or $\hat{Z}$, each occurring with probability $p/3$;

(4). To perform a measure qubit-data qubit CNOT or a measure qubit-measure qubit CNOT, but instead performed one of the two-qubit operations $\hat{I}\otimes\hat{X}$, $\hat{I}\otimes\hat{Y}$, $\hat{I}\otimes\hat{Z}$, $\hat{X}\otimes\hat{I}$, $\hat{X}\otimes\hat{X}$, $\hat{X}\otimes\hat{Y}$, $\hat{X}\otimes\hat{Z}$, $\hat{Y}\otimes\hat{I}$, $\hat{Y}\otimes\hat{X}$, $\hat{Y}\otimes\hat{Y}$, $\hat{Y}\otimes\hat{Z}$, $\hat{Z}\otimes\hat{I}$, $\hat{Z}\otimes\hat{X}$, $\hat{Z}\otimes\hat{Y}$, $\hat{Z}\otimes\hat{Z}$, each with probability $p/15$.

(5). Performing a measure qubit $\hat{Z}$ measurement, but reported a wrong value and projected to the wrong state with probability p.

The errors are assumed to be not intercorrelated and occur randomly during the simulation. The probability *p* is the per-step error in the surface code cycle. There are totally 10 steps in a cycle of error correction (Figure 6.5), so the overall error rate per cycle of the surface code is approximately 10*p* for the logical measure qubit case.

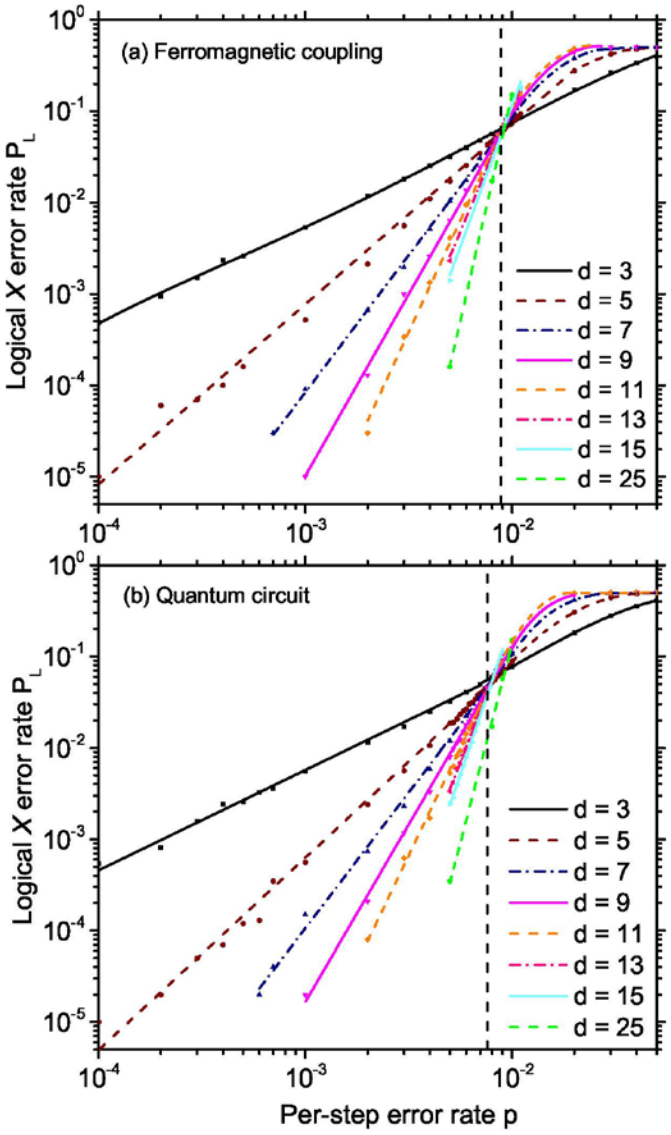

Figure 6.6: Numerical simulation of surface code error rates and how these error rates scale with the distance *d* of the array. The dashed vertical line shows the per-step threshold error rate. The dots represent the calculated results, while the curves are the fitting results. For a given per-step error rate *p* less than the per-step threshold error rate, the lines from top to bottom are for distances *d* from 3 to 25, which means that the surface code logical error rate P_L vanishes rapidly with increasing *d*. (a) In the case of logical measure qubits with ferromagnetic coupling, the per-step

threshold error rate is p_{th} = 0.88% (dashed vertical line). (b) Numerical simulation of surface code error rates for the case of logical measure qubits coupled with quantum circuits. The per-step threshold error rate is p_{th} = 0.76%.

Numerical simulation of surface code error rates and the dependence of the per-step threshold on the distance *d* of the array are shown in Figure 6.6. Note that the distance *d* of the surface code, the minimum weight of the set of nonidentity logical Pauli operators, is determined by the width or height (whichever is smaller) of the qubits array. The measurement circuit for both cases are considered. For the case with ferromagnetic coupling, the per-step threshold error rate is found to be p_{th} = 0.88%, which is close to the threshold of 0.9% in Ref. [148]. When the actual per-step error rate *p* is less than the per-step threshold error rate, the surface code logical error rate P_L rapidly vanishes with increasing *d*. After considering more steps in each cycle of measurement for the entangled two measure qubits, we can get the calculated per-step threshold error rate p_{th} = 0.76%. This threshold is only around 0.1% smaller than the single measure qubit case. When the logical measure qubits coupled with quantum gate circuits are measured during each stabilization cycle, in case any decoupling processes happened to the logical measure qubit, we should choose the measurement value from the qubit on which three CNOT gates are applied. In this way, the error induced by the decoupling of the two measure qubits is similar to the CNOT gate error in the single measure qubit case, where the expected measure qubit-data qubit CNOT is wrongly replaced with one of the two-qubit operations such as $\hat{X} \otimes \hat{Y}$. Therefore, larger threshold error rate similar to the single measure qubit case can be realized.

6.4.3 Realizable circuit layouts

The proposed robust topology is readily achievable for both flux qubits and Xmon qubits on the circuit level. One advantage of the CCJJ flux qubits scheme is the number of fan-outs. The fan-outs of each qubit not only permit single qubit operations and readouts, but also enable the all-to-all connections in each cell. It has been demonstrated that one qubit can be successfully coupled to six other qubits with direct couplers [152]. An architecture composed of over 1000 CCJJ flux qubits has already been demonstrated in the superconducting annealing processor D-Wave 2x made by

D-Wave Inc. [161]. However, the quantum annealing processor cannot be used for universal quantum computing because it is designed for cracking a very specific type of optimization problems.

A universal quantum computer composed of Xmon qubits is more promising and attractive for realizing the surface codes error correction because Xmon qubits have comparatively longer coherence time and higher gate operation fidelity [141]. A complete graph consisting of nonlocal interactions for more than dozens of superconducting qubits is nearly impossible to achieve with current technology. However, a complete graph for a small number of qubits is technically feasible. To realize the robust folded lattice structure, we can adopt the fast tunable couplers developed by Chen *et al*. [158] for Xmon qubits and replace the direct electrical connection of each Xmon qubit to a coupler circuit wire with an inductive coupling to the wire [162]. The inductive coupler wiring is similar to those used in the quantum annealing processor made by D-Wave Inc. [163]. Thereby the intersecting connections of couplers can be realized by adding several Nb wiring layers separated by planarized plasma enhanced chemical vapor deposited (PECVD) SiO_2. Meanwhile, due to the large footprints of the dispersive measurement circuits and *X*, *Z* control lines [3, 142], it is not easy to design a purely planar circuit layout for the Xmon qubits array without causing intersecting connections. The obstacle may also be overcome by adding several Nb wiring layers. Therefore, the proposed topology can be realized on a planar square-lattice structure with several additional wiring layers.

6.5 Summary

Here we propose a defect-tolerant surface code topology which is resistant to sparse fabrication defects. The circuit layout is a two-dimensional array of unit cells which is equivalent to a disk folded into *N* layers. Each unit cell is a complete graph K_N consisting of *N* physical qubits. In this architecture, a physically defective qubit can be replaced with another physical qubit in the same cell from a different layer. Thereby sparse fabrication errors can be collected into one sacrificial layer and isolated from the working layers by turning off their controllable couplers. We propose two schemes to realize this robust topology. One is to use flux qubits, and the other is based on Xmon qubits. For an array of Xmon qubits, we develop a modified quantum circuit for the stabilization cycle. The per-step error threshold of this scheme is estimated to be 0.76%, which is

close to the value for the unmodified quantum circuit. A possible way to implement the intersecting connections between different Xmon qubits on the circuit level is also provided.

Chapter 7
Quantum annealing with four-body interactions and error corrections through stabilizer codes

7.1 Introduction

Among all the non-universal quantum computation schemes, quantum annealing (QA) [164, 165] is one of the most promising approaches to demonstrate quantum speed-up shortly [166]. Since QA is easier to be realized on quantum hardware [167] than other schemes such as quantum circuit model and adiabatic quantum annealing, it has attracted substantial academic and industrial interest and inspired a rich body of literature on QA theories [164, 166, 168-170], applications [171-175], and experiments [152, 167, 176, 177]. The general paradigm of quantum annealing is to encode an optimization problem onto an objective Hamiltonian function of the *K*-spin model $H_P(\sigma)$. Its general form is

$$H_P(\sigma) = -\sum_{k=1}^{K} \sum_{j_1,\cdots,j_k=1}^{N} J_{j_1,\cdots,j_k} \sigma_z^{(j_1)} \cdots \sigma_z^{(j_k)}, \tag{7.1}$$

where N is the problem size, $\sigma_z^{(j)}$ is the Pauli-Z matrix associated with the j_{th} spin and the couplings $J_{j_1,\cdots,j_k}$ are real scalars. The task of finding the optimal solution to this optimization problem is converted into finding the ground state of H_P. If the evolution is sufficiently slow, quantum annealing can smoothly transfer an experimental qubits system from a trivial initial state, for example, the ground state of $H_I = \sum_{j=1}^{N} \sigma_x^{(j)}$, to the ground state of the objective Hamiltonian H_P. The whole time-dependent Hamiltonian of the system is

$$H(t) = \alpha(t/T)H_I + \beta(t/T)H_P \quad (0 \le t \le T), \tag{7.2}$$

where *t* is the time, *T* is the total time of the sweep, and $\alpha(t/T)$, $\beta(t/T)$ could be any functions with $\alpha(0) = 1, \beta(0) = 0$, and $\alpha(1) = 0, \beta(1) = 1$. Under adiabatic evolution, a programmable

quantum annealer eventually reaches the ground state of H_P with the aid of quantum tunneling, and one has thus found the desired result of the optimization problem.

Quantum tunneling can help QA penetrate high and narrow barriers which SA can hardly overcome, thereby exponential speedup may be achieved for certain types of problems. Among the numerous hard problems, K^{th} order binary optimization problem with $K > 2$ is perhaps the best example problem to which quantum annealing offers a runtime advantage [161]. K^{th} order optimization problem is NP-hard and has many real-world applications in engineering and computational tasks. Its energy landscape gets more rugged with higher K. There are many concerns over the implementation of QA on a practical quantum system.

One of the key challenges to map a K^{th} order optimization problem onto an analog quantum annealer is to realize the K-body coupling terms. The quantum annealing hardware to-date is built from superconducting qubits [154], and couplers [155, 156], and only supports pairwise qubit couplings ($K = 2$). Therefore, it is difficult to lay out K local couplers on a two-dimensional chip or in a three-dimensional architecture for $K > 2$. Lechner *et al.* [178] have proposed a scalable architecture with all-to-all connectivity for two-qubit interactions. Although it can be extended to four-body and higher-order K-body interaction terms, it is impossible to arrange the constraints in three-dimensional space. Even for three-qubit interaction terms, the qubits have to be arranged in an infinite three-dimensional architecture. The superconducting researchers usually try to avoid three-dimensional implementations because there are many problems that need to be addressed, such as the placement of measurement circuitry, etc., let alone the requirement for infinite space along z-axis.

Another major concern is its lack of an elaborate theory of fault-tolerant QA with a clearly-defined noise threshold for fault tolerance. There are several proposed ways to tackle the error correction for QA, such as adding a penalty term in a problem Hamiltonian and encoding qubits with repetition codes [179, 180].

In the chapter, we first propose a two-dimensional architecture implementing a Hamiltonian for the 4^{th} order optimization problem including four-qubit coupling terms formed with only local pairwise couplings. All possible four-body interactions for an N-qubit system can be encoded into this architecture and are realizable with existing programmable quantum annealers. The four-spin

model studied in this chapter was firstly proposed by F.Wegner in the context of statistical physics in 1971, which is called “Ising gauge model” [181, 182]. There exist a profound result that yields the equivalence between the two-dimensional Ising gauge model and one-dimensional Ising model. This architecture may provide an opportunity to study open challenges in quantum annealing such as the role of the two-dimensional nature of the plaquette constraints during the sweep, and the scaling of quantum fluctuations on an existing programmable quantum annealer. The detailed implementation of this architecture is introduced in the next section, followed by the comparison between the energy spectrum of the problem Hamiltonian and the executable Hamiltonian.

Second, we propose a quantum annealing protocol which can correct runtime errors during a sweep process with stabilizer codes. A quantum annealing architecture with all-to-all connectivity is first described by Lechner, Hauke, and Zoller (LHZ) [178]. *N* logical spins and their interaction terms in an annealing problem are translated to a larger spin array with only on-site energies and local constraints. Our proposal is based on the fact that the constraints of the above quantum annealing construction correspond to a set of stabilizers [183]. In this case, each stabilizer is a tensor product of pauli-z operators. Stabilizer codes [184] append measure qubits to data qubits. When the measurement outcome changes, one or more bit-flip or phase-flip errors have occurred. With the help of proper decoding algorithms, one can further determine which data qubits have errors. Checking the stabilizers with weak measurements [185, 186] has provided a viable way to extract average state information without fully collapsing the system. It has been demonstrated that with gentle measurements, one can measure the maximally entangled Bell state with minimal entanglement collapse [187], by violating the Bell-Leggett-Garg inequality (BLGI) [188]. Integrating weak measurements of stabilizers into a quantum annealer would correct most errors while offering an alternative source of quantum fluctuations in addition to the driver Hamiltonian. Sec.7.3 is organized as follows: The first subsection introduces the quantum circuits for implementing the weak measurements of stabilizer operators with an ancilla spin on each plaquette. The next subsection is to demonstrate how to extract the syndromes of stabilizers through weak measurements with the help of Lindblad master equation and the stochastic equation of motions. The following subsection shows that a jump from the instantaneous ground state to low-lying excited states can be identified through stabilizer measurements by adopting a modest constraint

strength. The last subsection introduces the processes to correct the flip errors caused by error channels as well as the accidental jumps to excited states.

7.2 2D implementation of fourth order binary optimization problems

The 4th order binary optimization problem can be mapped onto an objective Hamiltonian of a four-spin model consisting of arbitrary four-qubit interaction terms $H_P = -\sum_{j_1,\cdots,j_4=1}^{N} J_{j_1 j_2 j_3 j_4} \sigma_z^{(j_1)} \sigma_z^{(j_2)} \sigma_z^{(j_3)} \sigma_z^{(j_4)}$, where $\sigma_z^{(j)}$ is the Pauli-Z matrix of j_{th} qubit. The solution to the optimization problem is then transformed to finding the ground state of the objective Hamiltonian. Since their off-diagonal matrix elements in the standard product basis are all zero, it is easy to find that the i_{th} eigenstate $|\psi_i\rangle$ to this kind of stochastic Hamiltonian is a separable state. It takes the form $|\psi_i\rangle = |\phi_1\rangle \otimes \cdots \otimes |\phi_j\rangle \otimes \cdots \otimes |\phi_N\rangle$, and $|\phi_j\rangle$ is one of the two computational bases of single qubit. Thus, $|\psi_i\rangle$ is also the eigenstate to every four-qubit coupling term $h_P = -J\sigma_z^{(j_1)} \sigma_z^{(j_2)} \sigma_z^{(j_3)} \sigma_z^{(j_4)}$. We have $h_P |\psi_i\rangle = \pm J |\psi_i\rangle$. The main insight is that the contribution of a four-qubit coupling term to the energy of the whole problem Hamiltonian is determined by the product of the eigenvalues to the four single-qubit states in the computational basis $\sigma_z^{(j)} |\phi_j\rangle = \lambda_j |\phi_j\rangle$, where $\lambda_j = \pm 1$. The energy change applied by each coupling term to the whole system is thus $+J$ if $\lambda_{j_1} \lambda_{j_2} \lambda_{j_3} \lambda_{j_4}$ contains odd numbers of -1; otherwise, the energy change should be $-J$.

Inspired by Lechner *et al.* [178], we use $M = N(N+1)/2$ physical qubits from gauge constraints to represent N logical qubits and any pair of them in the problem Hamiltonian, where the eigenvalue of each physical qubit encodes the eigenvalues of $\sigma_z^{(j_1)} \sigma_z^{(j_2)}$ in the computational bases. Thus, a four-qubit interaction term h_P is encoded with a two-qubit coupling term $\tilde{h}_P = -J\tilde{\sigma}_z^{(j_1, j_2)} \tilde{\sigma}_z^{(j_3, j_4)}$. When one of the two physical qubits represents a single logical qubit, we can also encode a three-qubit interaction term into a two-qubit coupling term. All possible three- and four-qubit interactions for an *N*-qubit system can be mapped onto two-qubit interactions and

realized with existing quantum circuit technologies. The Hamiltonian of the four-spin model H_P is encoded in the executable Hamiltonian

$$\tilde{H}_P = -\sum_{j_1,\cdots,j_4=1}^{N} J_{j_1 j_2 j_3 j_4} \tilde{\sigma}_z^{(j_1,j_2)} \tilde{\sigma}_z^{(j_3,j_4)} + \sum_{l=1}^{M-N} C_l. \tag{7.3}$$

where M is the number of physical qubits and C_l is the local constraint that keeps the energy spectrum of the executable Hamiltonian consistent with the original problem Hamiltonian.

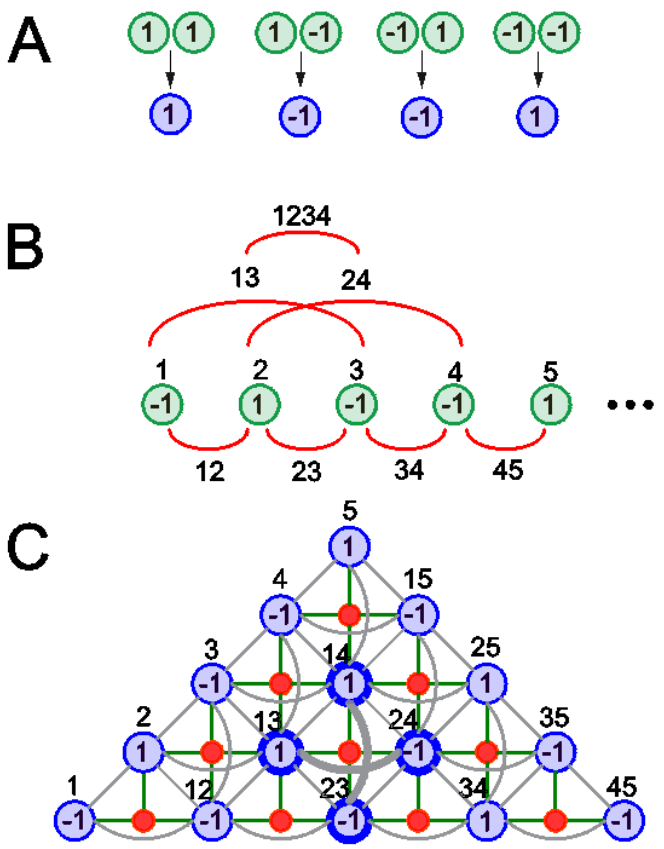

Figure 7.1: Illustration of the two-dimensional architecture. (A) New encoding qubit variables are introduced for each of the N logical qubits and each of the $N(N\text{-}1)/2$ interactions, which take the value 1 if the two connected logical spins point in the same direction and -1 otherwise. **(B)** The aim is to encode a system of N logical spins consisting of three- and four-qubit interactions. A part of the interactions is shown with solid lines. **(C)** The two-dimensional architecture corresponds to five logical qubits consisting of four-qubit interactions. The blue circles are physical qubits; red

dots are ancillary qubits for each plaquette. Solid bonds between two qubits are the pairwise couplings to realize the local constraints. The bold solid bond between qubits 14, 23 represents the sum of the couplings for the local constraints and a four-qubit interaction term $\sigma_z^{(1)}\sigma_z^{(2)}\sigma_z^{(3)}\sigma_z^{(4)}$. The four-qubit interaction term can also be realized by the coupling between qubits 13, 24.

7.2.1 Local constraints

The successful transformation from four-qubit coupling terms into two-qubit interactions relies on the consistency of the spin values among all physical qubits. We encode two connected spins pointing in the same direction as 1, and -1 otherwise (Figure 7.1A). The spin direction of a single qubit is also encoded as ± 1. Thus the relative spin directions of a pair of encoding qubits should be equal to any other ways of pairing the same four logical qubits. For example, the relative alignment of $\sigma_z^{(1,2)}\sigma_z^{(3,4)}$ should be equal to $\sigma_z^{(1,3)}\sigma_z^{(2,4)}$ and $\sigma_z^{(1,4)}\sigma_z^{(2,3)}$. This constraint should cover all encoding qubits and demands either none, two, or all four encoding qubits in a closed loop to be antiparallel. That is, the number of -1's in the four encoding qubits $\tilde{\sigma}_z^{(1,3)}$, $\tilde{\sigma}_z^{(2,3)}$, $\tilde{\sigma}_z^{(1,4)}$, $\tilde{\sigma}_z^{(2,4)}$ has to be even (bold circles in Figure 7.1C).

The consistency is achieved by introducing a configuration space in which a set of consistent qubit states are specified. Similar state subspace is also relevant in the context of the gauge-invariant subspace in lattice gauge theories [189]. The subspace is generated by applying local constraints on each plaquette of four qubits in a two-dimensional array, which is an individual tile enclosed by a set of edges - here a square of four physical qubits.

In order to realize the local constraints with existing superconducting qubits and couplers, we propose to use an ancillary qubit for each plaquette in the qubits array. The form of the constraint is

$$C_l = +C(\sum_{m=w,n,e} \tilde{\sigma}_z^{(l,m)} - \tilde{\sigma}_z^{(l,s)} - 2\sigma_z^{(l)})^2, \tag{7.4}$$

where C denotes the energy scale for the constraint term, and the letters *w*, *n*, and *e* represent the qubits on the west, north, east. The sum runs over any three members of each plaquette and then subtracts the spin value of the last one. $\sigma_z^{(l)}$ is an ancillary qubit for the l_{th} constraint.

Next, the boundaries of the architecture have to be taken care of. We introduce a separate constraint on the hypotenuse of the triangle array (Fig. 1C) which consists of triangles instead of squares. The constraint enforces the condition that the number of 1's in each of these triangles is odd and its form is

$$C_l = +C(\sum_{m=w,n,e} \tilde{\sigma}_z^{(l,m)} - 2\sigma_z^{(l)} - \mathrm{I})^2, \tag{7.5}$$

The sum runs over all three members of each triangle and I is an identity matrix. Only one ancillary qubit is used. Note that the constraint also involves local fields of physical qubits in each triangle. These two forms of constraints can be readily implemented by existing pairwise couplers and superconducting qubits.

7.2.2 Implement the required four-qubit interactions

As a final step, encoding all possible four-qubit interactions with two-qubit coupling terms in the physical qubits array needs long-range interactions that cannot be realized with the current technology. For the case of five logical qubits, to implement one of the four-qubit interaction terms $\sigma_z^{(1)}\sigma_z^{(2)}\sigma_z^{(3)}\sigma_z^{(5)}$ requires a coupling such as $\tilde{\sigma}_z^{(1,2)}\tilde{\sigma}_z^{(3,5)}$. The needed physical qubits are not neighboring to each other (Figure 7.1C). To realize the four-qubit interactions required by the optimization problem, we have two proposals to overcome the challenge.

First, since both four-qubit interactions and all local constraints are implemented by pairwise couplings, we can treat the resultant one as a new problem Hamiltonian and encode the physical qubits with a set of new physical qubits. With the same architecture, a second-time encoding can allow all four-qubit couplings required in the original problem Hamiltonian to be realized by the local fields of new physical qubits. The overhead of physical qubits is $O(N^4)$, which is on the same order as the previously proposed architecture in four-dimensional space [178]. Every logical qubit and every two-qubit interaction term are encoded N times, while every three- or four-qubit interaction term is encoded 3 times. Although this kind of repetition coding alleviates the error rate and makes the annealing process more robust against spin flips from decoherence, there are also a large portion of physical qubits which not only encode the ancillary qubits in the first-time encoding architecture but also all four-qubit interactions repeatedly, which decreases the minimal

energy gap on the spectrum of the final Hamiltonian. Furthermore, The O(N^4) overhead of physical qubits places a limit on the problem scale of the real applications which can be solved.

Second, many real optimization problems will necessitate only L=O(N) coupling terms. Thus not all possible high-order interactions are needed. We can split the final encoding Hamiltonian into several executable parts, and implement each part with a triangle array and concatenate them along their catheti with ferromagnetic couplings. For example, all possible four-qubit interactions in a Hamiltonian of five qubits can be split into two part: $H_{p1} = -J_1\sigma_z^1\sigma_z^2\sigma_z^3\sigma_z^4 - J_2\sigma_z^1\sigma_z^2\sigma_z^4\sigma_z^5 - J_3\sigma_z^2\sigma_z^3\sigma_z^4\sigma_z^5$ and $H_{p2} = -J_4\sigma_z^1\sigma_z^2\sigma_z^3\sigma_z^5 - J_5\sigma_z^1\sigma_z^3\sigma_z^4\sigma_z^5$. Each part is embedded into a triangle array, and two arrays are combined with ferromagnetic couplings (Fig. 2). The permutation of physical qubits can transform a long-range interaction of one array into a nearest-neighbor interaction in the other. Each triangle qubit array can be coupled on either of its catheti because either chain of qubits is a determining solution to the objective Hamiltonian. Thus this architecture is suitable for any required four-qubit couplings.

This architecture can be scaled up to K^{th} order multi-qubit interactions for $K > 4$ and K is even. The overall overhead of physical qubits is O(N^K). With increasing order of the coupling terms, the requirement for implementation precision surges because the energy scale of local constraints will dominate the problem Hamiltonian. Both the qubits cost and the demanding constraints energy scale pose challenges for the required programmable quantum annealer. However, future technology development on qubit, coupler designs, and superconducting materials can eventually overcome these obstacles.

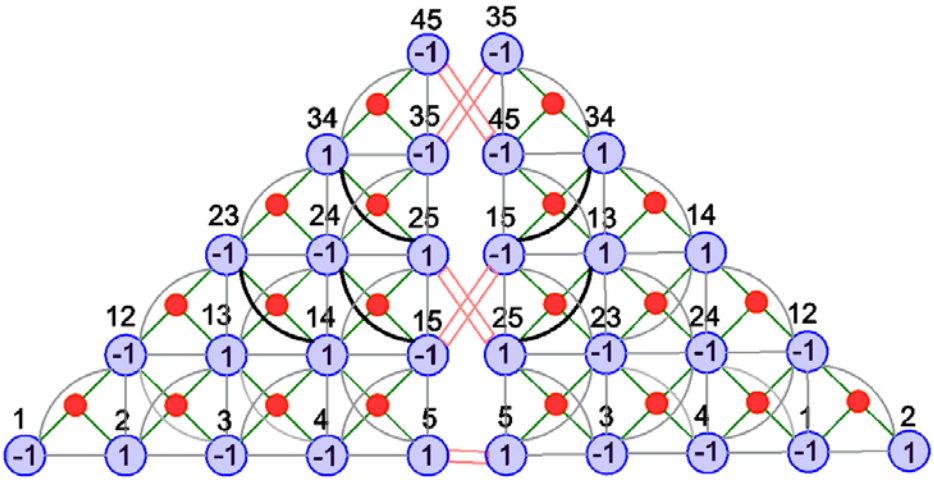

Figure 7.2: Scalable scheme. The scheme can be scaled to realize any four-qubit interactions in a 4^{th} order binary optimization problem. The problem consists of five qubits. The big blue circles represent the physical qubits; the small red circles denote ancillary qubits in each plaquette. The required four-qubit interactions are implemented by bold bonds between physical qubits. The two triangle arrays are coupled through ferromagnetic couplings (double lines) among physical qubits on one of the two catheti.

7.2.3 Readouts

The two schemes need different ways of readouts. For the first scheme, an appropriate way of decoding the encoded results is to make use of repetition codes and a majority-vote method. For simplicity, we focus on decoding the physical qubits representing single logical qubits and two-qubit interactions. Both are repeatedly encoded N times. First, we decode spin values of the single logical qubit and state configurations of two-qubit interactions out of the N-repetition codes. We can have robust readouts by decoding each N-repetition code. Second, we make use of a majority-vote method to obtain the final spin configuration for the original problem Hamiltonian.

After the first step of decoding, there are $N(N+1)/2$ spin values. The solution of the optimization can be fully determined by reading out an adequate choice of N among the $N(N+1)/2$ spin values. For example, in the case of N=5, one of the straightforward choices of readouts is the spin values for each logical qubit 1, 2, 3, 4, and 5. Other chains of relative configurations of pairs such as 5, 15, 25, 35, and 45, also hold the same information. A majority-vote method can be used among all

possible combinations of $N(N+1)/2$ spin values to improve the accuracy. For the second scheme, each triangle array holds $N(N+1)/2$ spin values. We can get the readout of each triangle block and apply a majority-vote method afterward.

7.2.4 Fault tolerance

The 2D architecture can be interpreted as a standard error-correcting code because of its redundant encoding of the logical qubits information in the physical qubits [190]. Thus it is highly robust against weakly correlated bit-flip noise. We use the product of $P_a P_b$ to determine the probability of retrieving errors from reading out all physical qubits when some spins are flipped as a result of decoherence. P_a is the probability that an erroneous readout of a spin value is obtained after the adiabatic sweep. P_b is the probability that a measurement indicates an erroneous solution due to this error.

For the first scheme, we do not take into account the ancillary qubits used in the first-time encoding because their readouts do not affect the solution. With N-repetition codes, the error rates for the readouts of the single logical qubit and two-qubit interaction terms are $P_r = \sum_{i=\lceil N/2 \rceil}^{N} \binom{N}{i} P_e^i (1-P_e)^{N-i}$, where $P_e = \Gamma \mathrm{T}$ is the probability for a spin flip of a physical qubit due to decoherence, and Γ is the decoherence rate, and T is the total time of the adiabatic sweep. We have $N(N+1)/2$ robust readouts and get $P_a = P_r N(N+1)/2$. The information content of a single readout of a spin value is given by the ratio between the determining solutions that contain the given readout, N_g, and the total number of possible determining solutions N_{all}, $P_b = N_g/N_{all} = 2/N$. The product $P_a P_b = (N+1)P_r$ is the probability for errors (dashed lines in Figure 7.3). A majority-vote method on the $N(N+1)/2$ robust readouts will give the correct answer as long as less than $N/4$ readouts from the N-repetition codes are faulty.

In the second scheme, each triangle array can be decoded independently. Suppose there are M triangle arrays combined, then $P_a = \Gamma T MN(N+1)/2$ and $P_b = 2/MN$. Thus the error rate scales linearly with the problem size N: $P_a P_b = (N+1)\Gamma T$ (solid lines in Figure 7.3). Applying a majority-vote method on all $MN(N+1)/2$ readouts can give the correct answer as long as less than $MN/4$ readouts are compromised.

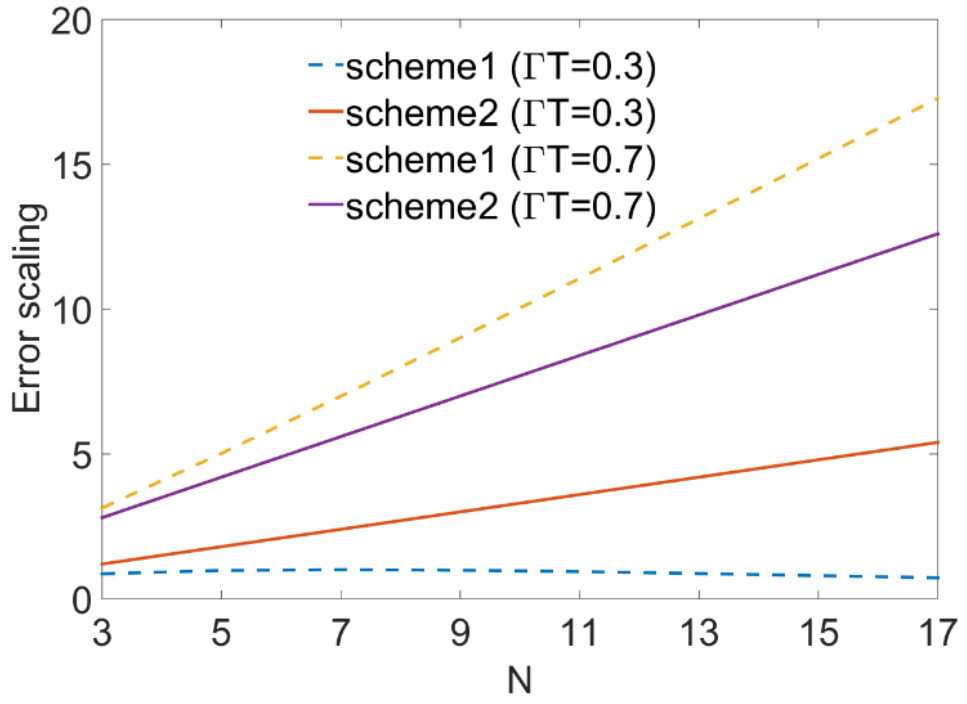

Figure 7.3: Error tolerance. For the first scheme, the total error depends on $P_e = \Gamma T$, the probability for a spin flip due to decoherence. When $P_e < 0.5$, the *N*-repetition codes for single logical qubit and two-qubit interactions decrease the error of the final decoding, and the total error decreases with increasing *N* (dashed blue). When $P_e \geq 0.5$, the total error rises with increasing *N* (dashed orange). For the second scheme, the total errors in both schemes scale linearly with *N* (solid red and solid purple).

7.2.5 Energy spectrum

The protocol to find the ground state of an executable Hamiltonian is the same as in the original *K*-spin quantum annealing described in Eq. (7.2). We choose the ground state of a simple

Hamiltonian that can be adiabatically transformed into Eq. (7.3). The simplest form of illustration could be

$$\tilde{H}_I = \sum_{m=1}^{M} h_m \tilde{\sigma}_x^{(m)}, \tag{7.6}$$

where $M = N^2$ is the number of all qubits including the ancillary qubits for the constraints. The adiabatic sweep is described by the time-dependent Hamiltonian

$$\tilde{H}_{sweep}(t) = \alpha(t/T)\tilde{H}_I + \beta(t/T)\tilde{H}_P \quad (0 \le t \le T). \tag{7.7}$$

In this architecture, the constraints should be modulated by $\beta(t/T)$. Otherwise, the low-energy levels are so closed to each other that the minimal gap is almost zero at the beginning of the sweep. In the second scheme of combining several triangle arrays, the three- and four-qubit interactions are realized through the couplers which also implement the couplings for the constraints. Those couplings will be dominated by the energy terms from the constraints. Usually, the couplings have to be normalized by a factor to within the range [-1,1], which is the operational range in current annealer chips. Thus the couplers must be able to achieve high precision when implementing the interaction terms.

The new time-dependent Hamiltonian is embedded in a larger Hilbert space and restricted in a gauge invariant subspace by the local constraints. It has a different spectrum, and the sweep is associated with a different quantum path compared to the adiabatic optimization in Eq. (7.2). The difference between the two sweeps is illustrated in Figure 7.4. The lowest states in the final Hamiltonian are identical in both representations of the optimization problem. However, the minimal gap in the direct implementation using interacting logical qubits is larger than the minimal gap in the executable architecture, and the ratio between these gaps increases with the energy scale C/J, see Figure 7.5. The calculated gap ratio is larger than what is obtained in [178] because we use ancillary qubits instead of four-qubit interactions to realize the local constraints.

Instead of calculating the energy levels of the second scheme, we compare the spectrum of the executable architecture implemented by single triangle array with an ideal sweep realized by logical qubits. Due to the limited technical progress on superconducting couplers at the moment, no other realistic way to tackle a Hamiltonian with high-order interactions on a large scale has been proposed, so this comparison should only serve as a benchmark. The second scheme uses more

physical qubits, but it is supposed to be applied to sparse high-order interactions. In this scenario, only several times more qubits are consumed. Compared with the architecture consisting of a single triangle array, the second scheme should lead to smaller but comparable energy gaps.

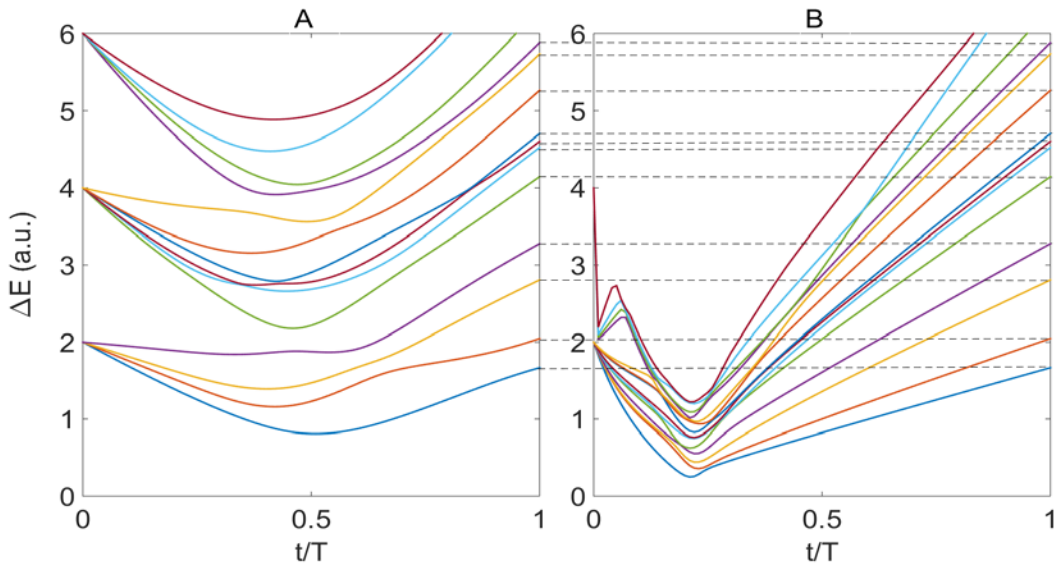

Figure 7.4: Time-dependent spectrum. (A) The energy spectrum of a typical adiabatic passage with N=4 logical qubits with four-qubit interactions in a fictitious implementation of the logical qubits. **(B)** The evolution of the executable Hamiltonian for the same problem implemented with ancillary qubits. Here, t is the time, and T is the total time of the sweep. Instantaneous eigenenergy E_i is measured with respect to the ground state, $\Delta E = E_i - E_0$. The coupling strengths for two-, three-, and four-qubit interactions and the local field of every logical qubit are random numbers uniformly taken from the interval [-J, J], and the constraint strength is C/J = 2. At the end of the evolution, an exact correspondence is achieved between the lowest levels of the two-dimensional architecture and the original model of classical spins (dashed lines).

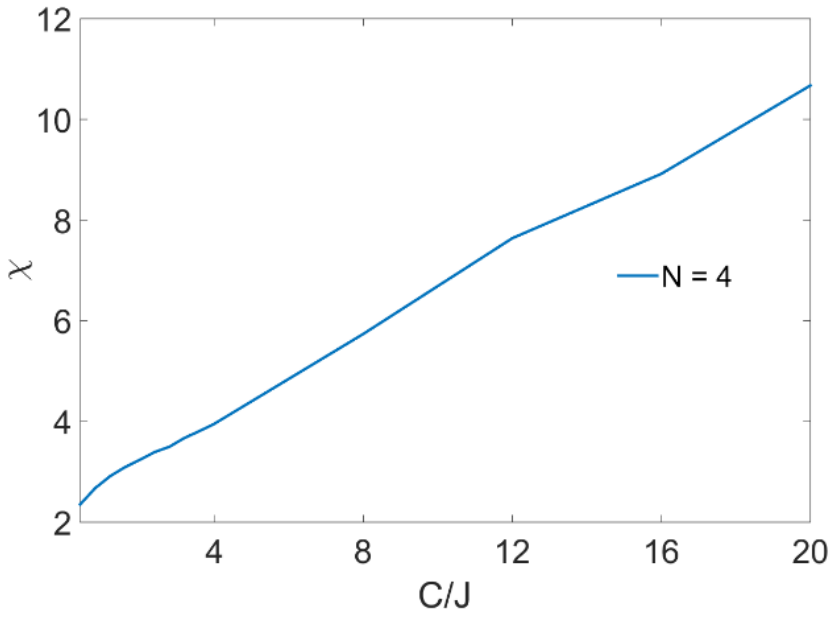

Figure 7.5: Ratio of energy gap. The ratio χ of the minimal gap during the adiabatic optimization between the logical system and the executable architecture, as a function of C/J, for N=4.

7.2.6 Optimal energy scale

The role of the energy scale $\beta = C/J$ is important for the successful implementation of the quantum annealing procedure. When $\beta \ll 1$, the constraints have no effect. When $\beta \gg 1$ the constraint dominates the problem scale and the comparatively small interaction terms implemented by the couplers can be easily affected by noises. Thus, there should be an optimal β for different problem Hamiltonian, which we denote as β_{opt}. We expect β_{opt} to be around 2. To understand the role of β_{opt}, consider first how increasing β affects the size and position of the gap ΔE. The excitations relevant to our local constraints are from the first excited state and above. In Figure 7.6A, we show that the relevant gap dwindles with increasing β when $\beta \leq 2$, and remains unchanged when β is increased further. The minimum gap position also develops over a shorter time, which is advantageous since it leaves less time for thermal excitations to act while the

transverse field dominates. However, the role of β is more subtle than suggested by considering only the gap. The energy states outside the gauge invariant subspace may also emerge in the low-energy spectrum. These additional energy levels are also determined by β. More impurity states may emerge in the low-energy spectrum with decreasing β. Figure 7.6B shows the dependence of the lowest impurity state on β, which encourages us to choose a larger β. On the other hand, Figure 7.5 shows the ratio of the minimal gap during the adiabatic optimization between the logical system and the executable architecture grows with increasing β. The real optimal value should be determined by experiments, with the above considerations in mind.

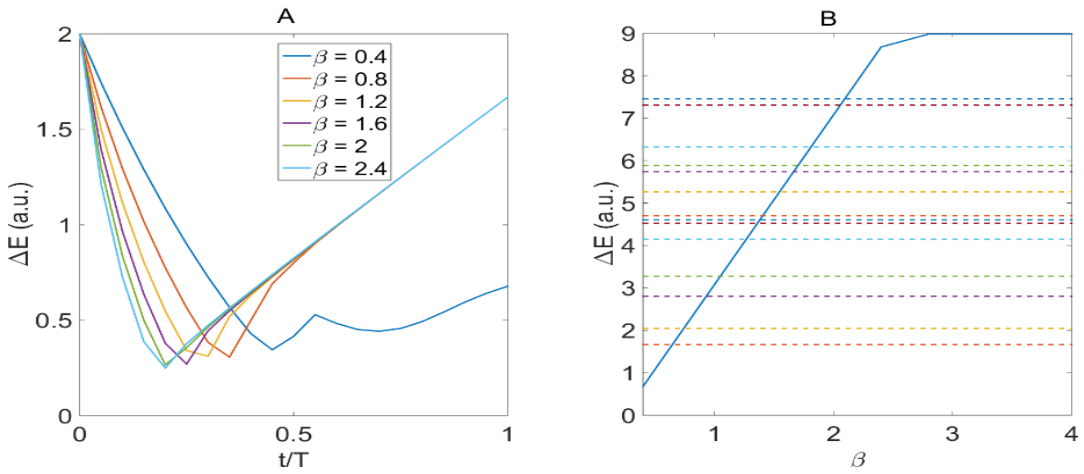

Figure 7.6: Effect of the energy scale of local constraints. (A) The relative first excited state varies with increasing β. (B) The dependence of the lowest impurity state (induced by constraint terms) on β. The energy of the impurity state increases with increasing beta and surpasses all energy levels of the problem Hamiltonian (dashed lines) at $\beta = 2.2$

7.2.7 Potential barrier for encoding Hamiltonian

There is a concern on the role of ancillary qubits over the energy landscape of the Hamiltonian [161]. In quantum annealing, spin tunneling can be described in mean field spin models using the path integral over spin-coherent states [191-193]. The dynamics are dominated by the paths

through the mean field energy landscape that has the highest transition probabilities. The mean-field potential is of the form

$$V(\hat{m}) = \langle \Psi_{\hat{m}} | \tilde{H}(t) | \Psi_{\hat{m}} \rangle, \tag{7.8}$$

where $\tilde{H}(t)$ is the time-dependent QA Hamiltonian (6) and $| \Psi_{\vec{m}} \rangle$ is a product state

$$| \Psi_{\hat{m}} \rangle = \bigotimes_j [\cos\frac{\theta_j}{2} | 0 \rangle + e^{-i\phi_j} \sin\frac{\theta_j}{2} | 1 \rangle]. \tag{7.9}$$

The coherent state of the j_{th} spin is defined by a vector on the Bloch sphere

$$\mathbf{n}_j = (\sin\theta_j \cos\phi_j, \sin\theta_j \sin\phi_j, \cos\theta_j), \tag{7.10}$$

moreover, the corresponding state of the N-qubit system is defined by the tensor $\hat{\mathbf{m}} = (\mathbf{n}_1, \mathbf{n}_2, \cdots, \mathbf{n}_N)$.

The mean-field potential can be split into two parts $V_1(\hat{m}) = \langle \Psi_{\hat{m}} | \tilde{H}(t) - \beta(t) \sum_l C_l | \Psi_{\hat{m}} \rangle$ and $V_2(\hat{m}) = \beta(t) \sum_l \langle \Psi_{\hat{m}} | C_l | \Psi_{\hat{m}} \rangle$. Each ancillary qubit appears only in one term of $V_2(\hat{m})$. We rewrite each constraint term as $C_l = C_l^{(1)} + C_l^{(2)} + 8\mathrm{I}$, where $C_l^{(1)} = -4C(\sum_{m=w,n,e} \tilde{\sigma}_z^{(l,m)} - \tilde{\sigma}_z^{(l,s)}) \sigma_z^{(l)}$ is the part involving an ancillary qubit, $C_l^{(2)}$ is the rest part of the constraint term. The form of $C_l^{(1)}$ is similar to the energy penalty terms used in the quantum annealing error correction codes [179, 180]. Both the constraints and the energy penalty terms are to restrict the whole system into a specified code space and to punish the states outside this space.

The effect of the two-dimensional local constraints on the energy landscape of an *N*-qubit system is an open question. The width of a potential barrier is measured with the change of the state of an *N*-qubit system between two local minima. For a rugged energy landscape, a narrow barrier means small changes of the state of the *N*-qubit system. Since every ancillary qubit is only coupled with three- or four-nearest neighbor qubits, small changes of the *N*-qubit states may leave most of the ancillary qubits unvaried.

7.3 Error correction for quantum annealing

7.3.1 LHZ annealer

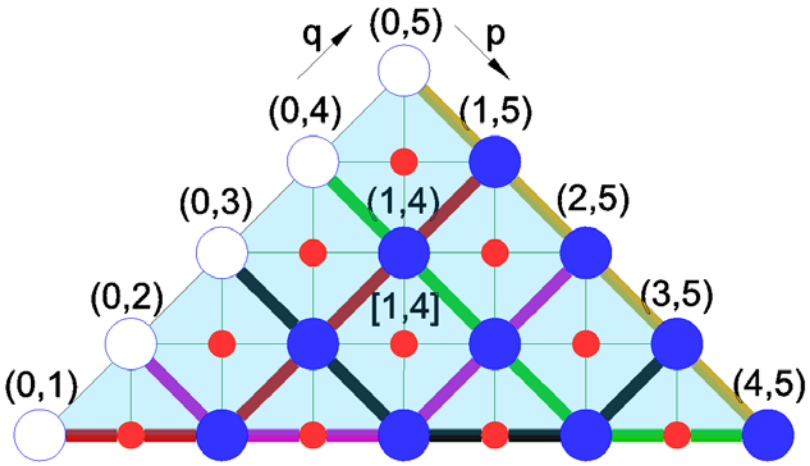

Figure 7.7: The topology for a 5-logical-spin LHZ annealer with stabilizers (azure patches). The lattices of $N = n(n+1)/2$ physical spins are used to encode the all-to-all connected two-body interactions for *n* logical spins. The open and solid circles are the physical spins; each open circle corresponds to the local field acting on a logical spin, whereas the spin at each solid circle corresponds to a two-body coupling between logical spins. The round bracket of indices (*p*, *q*) is used to denote the position of each physical spin while the bracket [*p*, *q*] labels the position of a stabilizer acting on three or four adjacent data spins. Red dots represent ancillary spins for stabilizer measurements.

The topology for a 5-logical-qubit LHZ annealer is shown in Figure 7.7. The spins located on the cathetus of the triangle array represent the logical spins. The rest spins denote the two-body terms. The topology is designed as follows [183]: if a physical spin represents a two-body term in a logical Hamiltonian, then the lines representing the two associated logical x operators must cross.

Each chain with the same color is a logical x operator $\sigma_X^k = \prod_i \tilde{\sigma}_X^{(i,k)} \prod_j \tilde{\sigma}_X^{(k,j)}$, where *k*=1,2, …, *N*, and the logical σ_X^k operator is the product of Pauli operators of the set of data spins with a label of either *i*= *k* or *j* = *k*. The spin located at the intersect of two logical x chains represents the

two-body term for the two logical spins. Each logical x operator should commute with all stabilizers represented by azure plaquette.

Let's consider a quantum system Q that evolves slowly according to the Hamiltonian $H(t)=[1-f(t)]H_0+f(t)H_f$, where $f(0)=0$, $f(\tau)=1$, and τ is the final time. Our target optimization problem $H_T=\sum_{q=1}^{n}h_q\sigma_Z^q+\sum_{p=1}^{n-1}\sum_{q=p+1}^{n}J_{pq}\sigma_Z^p\sigma_Z^q$ can be mapped onto a new problem Hamiltonian $H_f=\sum_{q=1}^{n}\tilde{h}_q\tilde{\sigma}_Z^{(0,q)}+\sum_{p=1}^{n-1}\sum_{q=p+1}^{n}\tilde{J}_{pq}\tilde{\sigma}_Z^{(p,q)}+H_C$. $\tilde{\sigma}_Z$ is the Pauli-Z operator for each physical spin in Figure 7.7. $\boldsymbol{H}_C$ is the constraint Hamiltonian that forces the physical spins to evolve in the subspace defined by the stabilizers. A simple form of $\boldsymbol{H}_C$ is chosen as $H_C=\frac{C}{2}\sum_{[p,q]}(1-\nu_{pq}S_Z^{[p,q]})$, where C is the constraint strength, $S_k^{[p,q]}$ is the stabilizer for each plaquette,

$$S_k^{[p,q]}=\begin{cases}\tilde{\sigma}_k^{(p,q)}\tilde{\sigma}_k^{(p,q-1)}\tilde{\sigma}_k^{(p-1,q)}\tilde{\sigma}_k^{(p-1,q-1)} & \text{if } p+2\le q\\ \tilde{\sigma}_k^{(p,q)}\tilde{\sigma}_k^{(p-1,q-1)}\tilde{\sigma}_k^{(p-1,q)} & \text{if } p+2>q\end{cases},\ (k=X,Z) \qquad (7.11)$$

and $\nu_{pq}=\pm1$, also known as parity value, is the expected eigenvalue of $S_Z^{[p,q]}$ for the final ground state. Given a certain form of $\boldsymbol{H}_C$, $\tilde{h}_p$ and $\tilde{J}_{pq}$ are equal to h_p and J_{pq} up to ±1, respectively. The initial Hamiltonian H_0 has to be carefully chosen because it should not commute with H_f. We design the initial Hamiltonian as $H_0=-\sum_{p=0}^{n-1}\sum_{q=p+1}^{n}\tilde{\sigma}_X^{(p,q)}$.

7.3.2 Quantum feedback control

Our protocol combines weak measurements of the stabilizers with feedback control to implement continuous error correction in an LHZ quantum annealer. The weak measurements will have unobtrusive effects on the physical system and give error specific information when the state of the system is not in the code space. Also, the filtering process is introduced to smooth out some of the noise in the measurement currents. Such filtering makes the noise in the feedback signal at

time *t* is dependent on the system state at time *t*. Thus, smoothing procedure results in the quantum Bayesian feedback, instead of Markovian feedback. One reason for the feasibility of the continuous error detection through stabilizer measurement is that whether the state of the system is inside or outside the code space can be determined by the signatures of the stabilizer measurements (whether they are plus or minus one). Such a quantity is robust under the influence of noise.

The stochastic master equation (SME) describing the evolution of a system with feedback under the error control protocol is [194]:

$$\begin{aligned} d\rho_c(t) = & -i\left[H(t), \rho_c(t)\right]dt \\ & + \sum_k \sum_{(p,q)} \frac{\gamma}{3} \mathcal{D}[E_k^{(p,q)}]\rho_c(t)dt \\ & + \sum_{k=X,Z} \sum_{[p,q]} \kappa \mathcal{D}[S_k^{[p,q]}]\rho_c(t)dt + \sqrt{\kappa}\mathcal{H}[S_k^{[p,q]}]\rho_c(t)dW_k^{[p,q]} \\ & - i\sum_k \sum_{(p,q)} G_k^{(p,q)}(t)[F_k^{(p,q)}, \rho_c(t)]dt \end{aligned} \tag{7.12}$$

where ρ_c is the system density operator conditioned on the measurement records of $\{S_k^{[p,q]}\}$, $E_k^{(p,q)} = \{\sigma_k^{(p,q)}\}_{k=X,Y,Z}$ is a collection of generic balanced depolarizing error channels for *N* physical spins, γ is the per-spin error rate which corresponds to a per time step error rate of γdt, κ is the measurement strength (assumed to be the same for all measurements $S_k^{[p,q]}$, $\mathcal{D}$ and $\mathcal{H}$ are the superoperators for decoherence and stochastic process, respectively, and given by

$$\mathcal{D}[A]\rho = A\rho A^\dagger - \frac{1}{2}(A^\dagger A\rho + \rho A^\dagger A), \tag{7.13}$$

$$\mathcal{H}[A]\rho = A\rho + \rho A^\dagger - \rho \mathrm{tr}[A\rho + \rho A^\dagger], \tag{7.14}$$

for any operator A, $dW_k^{[p,q]}$ are the Weiner increments (Gaussian distributed random variables with zero mean and autocorrelation $\langle dW(s)dW(t)\rangle = \delta(s-t)dt$) [195], $F_k^{(p,q)}$ $(k = X, Z)$ are the correcting feedback Hamiltonian acting on the physical spin at (p,q) corresponding to $\tilde{\sigma}_X$ and $\tilde{\sigma}_Z$ terms in $H(t)$, respectively, and $G_k^{(p,q)}$ is the corresponding conditional function of the

signatures of all the smoothed stabilizer measurement, $\{S_k^{[p,q]}\}$. The measurement current for $\{S_k^{[p,q]}\}$ has the form: $dQ_k^{[p,q]} = 2\kappa \left\langle S_k^{[p,q]} \right\rangle_c dt + \sqrt{\kappa} dW_k^{[p,q]}(t)$, where $\left\langle a \right\rangle_c = \mathrm{tr}(\rho_c a)$. The simple filter we choose to smooth out the noise on the measurement current is a convolution in time between the measurement signal and an exponentially decaying signal:

$$R(t) = \frac{1}{\mathcal{N}} \int_{t-T}^{t} e^{-r(t-t')} dQ(t') . \tag{7.15}$$

In frequency space, this acts as a low pass filter, and thus the output of the operation is a smoothed version of the measurement current with high-frequency oscillations removed. The filter parameters r and T determine the decay rate and length of the filter, respectively, and $\mathcal{N} = \frac{2\kappa}{r}(1 - e^{-rT})$ serves to normalize $R(t)$ such that it is centered around ± 1.

7.3.3 Detection of bit-flip and phase-flip errors

The phase-flip (Z) errors can be detected by S_X measurements alone, and the bit-flip (X) errors can be detected by S_Z measurements alone, while the Y errors are to be detected by both S_X and S_Z measurements. The signatures of the stabilizer measurements can be used to identify the error chains with the standard algorithms such as Edmonds' minimum-weight perfect matching algorithm [159], which has been used in other error correction methods such as surface codes [151].

The difference in the measurement stages between the surface codes and our error correction proposal is the arrangement of measurements. In the surface codes, each plaquette is measured by either S_X or S_Z. The two kinds of the stabilizers have a staggered arrangement on a square lattice. In our scheme, every plaquette (which is equivalent to the combination of plaquettes and vertices in the surface codes) should be weakly measured by both S_Z and S_X stabilizers. This measurement scheme is based on the following considerations. First, the parity value ν_{pq} in each plaquette's constraint Hamiltonian should be determined by the corresponding S_Z measurement, while S_X is needed to correct the Z errors on each plaquette. Second, measuring every plaquette with two kinds

of stabilizers can eliminate the 1-cycles inside the triangular spin array. These 1-cycles lead to the ambiguity when identifying an error chain in the surface codes because the syndromes for an error chain are not changed by adding a 1-cycle to the existing error chain. Although this ambiguity does not have effects on the correction in the surface codes, it will hamper successful error corrections in quantum annealing since any irrelevant corrections may deviate the quantum system from its instantaneous ground state. The remaining 1-cycles which cannot be removed are the chains of logical X operators. All of these chains run through the whole array and have the lengths of the number of logical spins. As the size of spins array grows, the possibility of such a long error chain will be exponentially small. Thus, there may be no ambiguity for determining error chains through the measurement signatures when long chains of errors do not show up during an annealing process. Figure 7.8 shows a typical X-error chain with its syndromes around it.

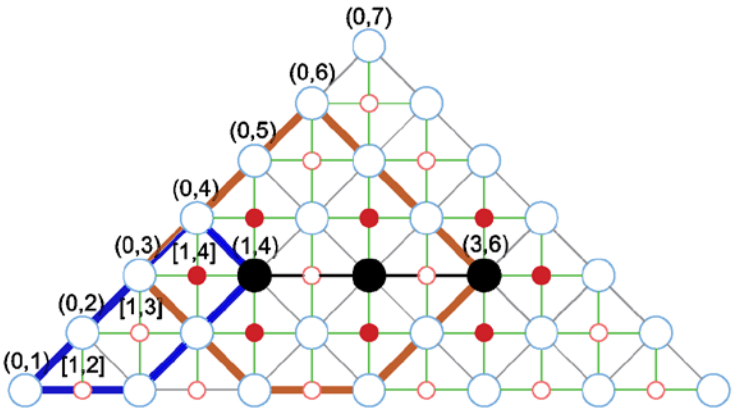

Figure 7.8: A bit-flip error chain detected by the syndromes. Black circles represent wrongly flipped data qubits, and red dots are the signatures from the S_Z measurements. The plaquettes encircled by blue lines are relevant to the X error correction at spin (1,4). The brown lines enclose an area in which the stabilizers' signatures are responsible for correcting the error at spin (3,6).

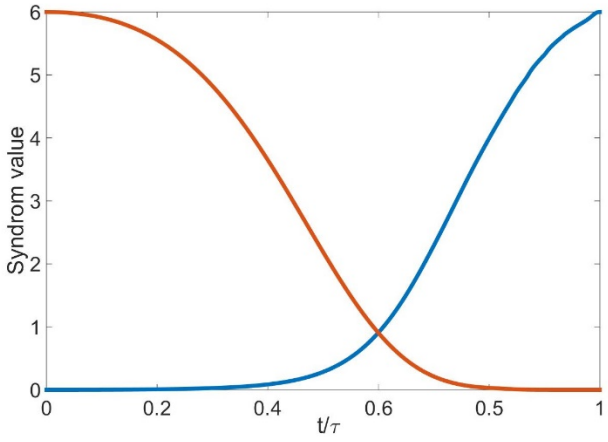

Figure 7.9: The time dependence of $\sum_{[p,q]}\left|\left\langle S_X^{[p,q]}\right\rangle_c\right|^2$ and $\sum_{[p,q]}\left|\left\langle S_Z^{[p,q]}\right\rangle_c\right|^2$ averaged over 1000 simulations on four logical spins with random couplings *h* and *J* which are uniformly distributed within the interval [-1,1].

It has to be noted that the expectation values of S_X and S_Z are not constants during the sweep. Given the initial state as the ground state of H_0, $\left\langle S_X^{[p,q]}\right\rangle_c$ changes from 1 at the beginning of the sweep to 0 at the end of the sweep, while $\left\langle S_Z^{[p,q]}\right\rangle_c$ changes from 0 to 1. Correspondingly, the sum of the square of every stabilizer's expectations in the instantaneous ground state changes between 0 and $n(n\text{-}1)/2$ (n is the number of logical spins) as shown in Figure 7.9. At a given moment *t*, if the change of expectations $2\left|\left\langle S\right\rangle_c\right|$ induced by error channels is bigger than that induced by measuring errors and noises, it is possible to identify these errors through stabilizer measurements. The error syndromes are determined by the difference between the signatures of the measured currents and the expected values. The expected signatures for $\left\langle S_X^{[p,q]}\right\rangle_c$ and $\left\langle S_Z^{[p,q]}\right\rangle_c$ are determined by choice of H_0 and parity values ν_{pq} at the beginning of the annealing protocol. Further, the system is robust against X errors at the start of a sweep when $H_0 \gg H_f$, because X errors do not alter the eigenstates of H_0; similarly, Z errors have negligible effects on the system

when the sweep approaches the end. Since the measurement itself will induce errors, we do not want the measurements to destroy the systems' state. Thus, we apply S_X measurements from the beginning to $t/\tau = 0.6$, while S_Z stabilizers are measured from $t/\tau = 0.4$ to the end. The start time and end time of S_Z and S_X measurements can be adjusted according to specific logical problem and error rate.

7.3.4 Detection of low-lying excited states

Whether a jump from the ground state to an excited state during a sweep is detectable depends on the parity values of the low-lying excited states. Let $R = C/J$. As discussed by Rocchetto *et al.* [183], if R is too large, it will appear that the low-lying excited states have the same parity values as the ground state, therefore, jumps from the ground state to these excited states are undetectable via parity. On the other hand, a small R makes the spectra of the several parity subspaces overlap and may permit the low-lying excited states to violate the parity constraints and conceivably allow us to detect them using weak measurements. However, such a change to the energy levels may decrease the smallest gap between the ground state and the excited states during a sweep. Hence the overlap of the spectra of several parity subspaces may come at the cost of a smaller energy gap, as shown in Fig. 4 (a). A modest R value is thus best suitable to serve our purpose.

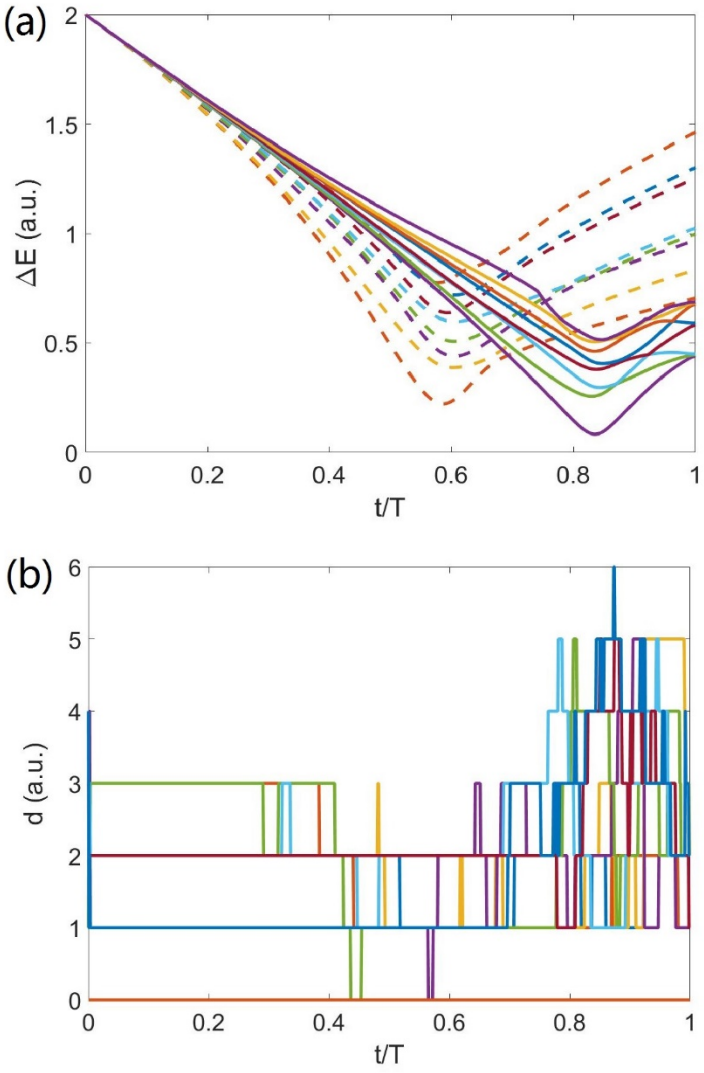

Figure 7.10: (a) Energy spectra of the low-lying excited states for constraint strengths R = 0.6 (solid lines) and R = 2 (dashed lines) in a typical adiabatic sweep with N=4 logical qubits. The instantaneous excited energy E_i is measured in the instantaneous ground state, and the plotted $\Delta E = E_i - E_0$. The elements of the $\tilde{h}_q$ and $\tilde{J}_{pq}$ matrix are numbers randomly taken from the interval [-J, J]. (b) The differences between the signatures of eight lowest-energy excited states and the ground state are tracked during the same annealing process with R = 0.6 in (a). The distance d is defined in the main body.

To illustrate the idea of detecting erroneous excited states during a sweep through weak measurements on stabilizers, we define a parameter d_m for the m_{th} level (zeroth level is the ground state) $d_m(t) = \sum_{[p,q]} \left| x_m^{[p,q]}(t) - x_0^{[p,q]}(0) \right| + \left| z_m^{[p,q]}(t) - z_0^{[p,q]}(\tau) \right|$ to distinguish the instantaneous ground state from the low-lying excited states. $x_m^{[p,q]}(t) = \text{sgn}\left(\left\langle S_X^{[p,q]} \right\rangle_m (t) \right)$ and $z_m^{[p,q]}(t) = \text{sgn}\left(\left\langle S_Z^{[p,q]} \right\rangle_m (t) \right)$ are the signatures of the measurements of the stabilizers for the m_{th} level at a given time t. $x_0^{[p,q]}(0)$ and $z_0^{[p,q]}(\tau)$ are the signatures of $\left\langle S_X^{[p,q]} \right\rangle$ for the initial state and of $\left\langle S_Z^{[p,q]} \right\rangle$ for the final state, respectively, which are determined by choice of initial Hamiltonian H_0 and parity values ν_{pq}. The calculated results are shown in Figure 7.10(b) for R = 0.6. The distance d for the ground state remains zero throughout the annealing sweep. Hence, we can monitor the signatures from both operators $S_X^{[i,j]}$ and $S_Z^{[i,j]}$ at successive measurements to identify a jump from the instantaneous ground state. If the state of the system deviates from its instantaneous ground state, the measured signatures will change. It is possible that the signatures of some excited states overlap with that of the instantaneous ground state during a sweep, which is shown in Figure 7.10(b) as two dips of $d(t)$. It is caused by the overlaps of several parity subspaces. As R increases, there will be more low-lying excited states staying in the same subspace as the ground state does, which makes it impossible to distinguish them from the ground state through this method. However, if R is a modest value, a part of the transition from the ground state to excited states can be identified, which is an advancement over the existing quantum annealing.

7.3.5 Error corrections

Bit-flip and phase-flip errors can be corrected by performing physical gate operations on the data spins; however, applying such gates will take a long time and pause the quantum annealing sweep, thus causing a higher error rate. There are two requirements for a successful correction of X or Z errors. The corrections should keep the instantaneous state in the ground state of the system while making the final Hamiltonian still represent a correct map of the logical Hamiltonian. To restore the erroneously bit-flipped state to the instantaneous ground state, we can change the sign of the

on-site energy $\tilde{J}'_{pq} = -\tilde{J}_{pq}$ or $\tilde{h}'_q = -\tilde{h}_q$ in the following time of the same annealing process. Suppose $\psi_0(t)$ is the instantaneous ground state of the total Hamiltonian $H(t) = [1 - f(t)]H_0 + f(t)H_f$ at time *t*. We can have:

$$\sigma_X^{(p,q)} H(t)\psi_0(t) = H'(t)\sigma_X^{(p,q)}\psi_0(t) = E_0(t)\sigma_X^{(p,q)}\psi_0(t), \tag{7.16}$$

where

$$H'(t) = [1 - f(t)]H_0 + f(t)H'_f, \tag{7.17}$$

$$H'_f = \sum_{q'=1}^{n} \tilde{h}_{q'}\tilde{\sigma}_Z^{(0,q')} + \sum_{(p',q')\neq(p,q)} \tilde{J}_{p'q'}\tilde{\sigma}_Z^{(p',q')} + \tilde{J}'_{pq}\tilde{\sigma}_Z^{(p,q)} + H'_C. \tag{7.18}$$

Since H_C includes the stabilizer $S_Z^{[i,j]}$, the parity values ν_{pq} for the affected stabilizer terms also have to be changed according to the measured signatures. Then it is evident that $\sigma_X^{(i,j)}\psi_0(t)$ becomes the ground state of the new evolving Hamiltonian.

The Ising interaction $J_{pq}\sigma_Z^p\sigma_Z^q$ in the logical Hamiltonian is mapped to $\tilde{J}_{pq}\tilde{\sigma}_Z^{(p,q)}$ in the model up to a sign determined by the values of stabilizers,

$$\tilde{J}_{pq} = J_{pq}\prod_{p'=1}^{p}\prod_{q'=p'+1}^{q}\nu_{p'q'}. \tag{7.19}$$

All the plaquettes corresponding to the signs of spin (*i*, *j*) are within the area enclosed by logical operators σ_X^p and σ_X^q. In Figure 7.8, the on-site energy for the data spin $\tilde{\sigma}_Z^{(1,4)}$ is $\tilde{J}_{14} = \nu_{12}\nu_{13}\nu_{14}J_{14}$. The affected plaquettes are enclosed by blue lines. Therefore, if we change the signs of ν_{12}, ν_{13}, ν_{14} and $\tilde{J}_{14}$ at the same time, we can still keep the final Hamiltonian as a true map of the logical Hamiltonian. As long as there exists a chain of *n* spins which can be used as a readout sequence free from errors, the two requirements can be met simultaneously by flipping the on-site energies of the affected spins and the corresponding parity values in the constraint Hamiltonian. The number of possible readout sequences of spin chains that can be used for this purpose exponentially increases with *N*. Hence; there is a significant possibility that the way of correction is effective.

The same procedure may be easily adapted to also correct Z errors. Instead of applying a Z gate on the affected spin, we change the sign of the corresponding energy term $\tilde{\sigma}_X^{(p,q)}$ in H_0. Thus, the wrongly flipped state should be the ground state of the new evolving Hamiltonian while the map from logical problem to physical Hamiltonian remains the same. Recovering a detected deviation from the instantaneous ground state is the same as that for correcting X and Z errors since the erroneous excited state is identified through the difference of the signatures between the measured values and the expected values.

7.3.6 Simulation results

We simulate the dynamics of Eq. (7.12) by way of an associated stochastic Schrodinger equation (SSE) as it is less computationally intensive and allows us to look at individual trajectories of the system. The form of this associated SSE is as follows:

$$\begin{aligned} d\left|\psi_c(t)\right\rangle = &+\sum_k \sum_{(p,q)} \left(E_k^{(p,q)}\left|\psi_c(t)\right\rangle - \left|\psi_c(t)\right\rangle\right) dM_k^{(p,q)}(t) \\ &- \sum_{k=X,Z} \sum_{[p,q]} \frac{\kappa}{2}\left(1 - \left\langle S_k^{[p,q]}\right\rangle(t) S_k^{[p,q]}\right)^2 \left|\psi_c(t)\right\rangle dt \\ &+ \sum_{k=X,Z} \sum_{[p,q]} \sqrt{\kappa}\left(S_k^{[p,q]} - \left\langle S_k^{[p,q]}\right\rangle(t)\right)\left|\psi_c(t)\right\rangle dW_k^{[p,q]}(t) \\ &- iH'(t)\left|\psi_c(t)\right\rangle dt \end{aligned}, \qquad (7.20)$$

where $dM(t)$ is a point process increment (in the number of errors) described by $dM(t)^2 = dM(t)$, and $E\left[dM(t)\right] = \frac{\gamma}{3}dt$. Thus, $dM(t)$ is a random variable that is either 0 or 1 at each time step and is distributed according to the error rate $\gamma/3$. A graph of the process $dM(t)$ would be a sequence of Poisson distributed (with parameter $\gamma/3$) spikes. $H'(t)$ is the corrected Hamiltonian defined in Eq. (7.17) according to the smoothed measurements $\left\{R_k^{[p,q]}(t)\right\}$.

In the continuous feedback based error correction scheme, the information of stabilizer measurements is obtained at a finite rate. To protect a fragile quantum state in the surface codes, the finite duration of the detection and correction window means that we must choose the parameter T in Eq. (7.15) small enough that the probability of an error we cannot correct is negligible. On

the contrary, we may still get improvements in the success rate for quantum annealing even if errors occur during the finite window T since quantum annealing is more robust against the X and Z errors. Therefore, it is possible to do the error corrections when the rate at which we gain information (characterized by measurement strength κ) is about the same as or lower than the rate γ at which errors happen.

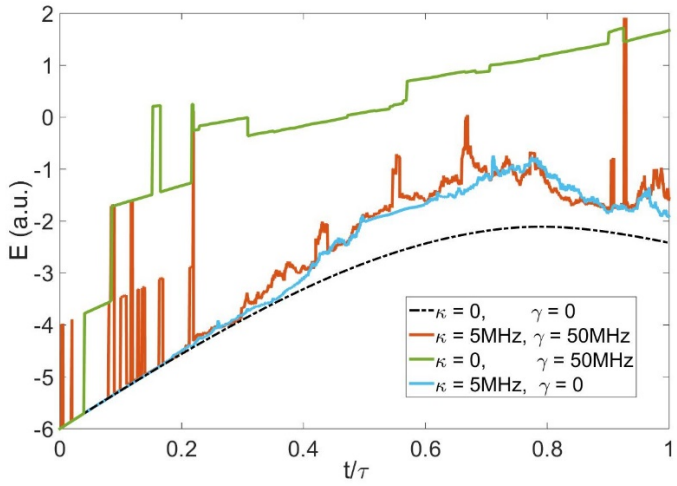

Figure 7.11: The trajectories for 3 logical spins are computed with stochastic evolution equation under different measurement strengths κ and error rates γ. The dark red curve shows the time evolution of the system with $\kappa = 5\text{MHz}$ and $\gamma = 50\text{MHz}$, while the light green curve is the time evolution with the same error rate but no feedback control. The blue curve illustrates the time evolution with $\kappa = 5\text{MHz}$ without errors. The dashed curve shows the whole evolution without errors and feedbacks.

A sample simulation run for a realistic noise process, also known as a trajectory, is calculated using the stochastic evolution Eq. (7.20) for 3 logical spins. The energy evolutions of the system under different κ and γ are shown in Figure 7.11. The stochastic differential equation was solved using Euler numerical integration with time step 2×10^{-4} ns. The total annealing time is $40/\Delta_{\min}$. The qubit transition frequency $\omega_q/2\pi = 0.5$ GHz and $R = 1$. The filtering window time is $T = 2$ ns, $r = 5$ GHz. γ is chosen much larger than κ for the purpose of demonstrating error corrections

during the annealing process. The red curve shows the smooth trend at the beginning as S_X has little effects on the system. The spikes are resulted from the error-induced transitions but corrected by the control feedback. At last, the system which is protected by the error correction scheme is still close to the ideal final state which is shown by the dashed curve. On the contrary, under the same error rate, the system deviates from the ideal ground state more and more as time passes. In contrast, the measurements will affect the evolution of the system as shown by the blue curve. It almost overlaps with the red curve except for the correction-induced spikes.

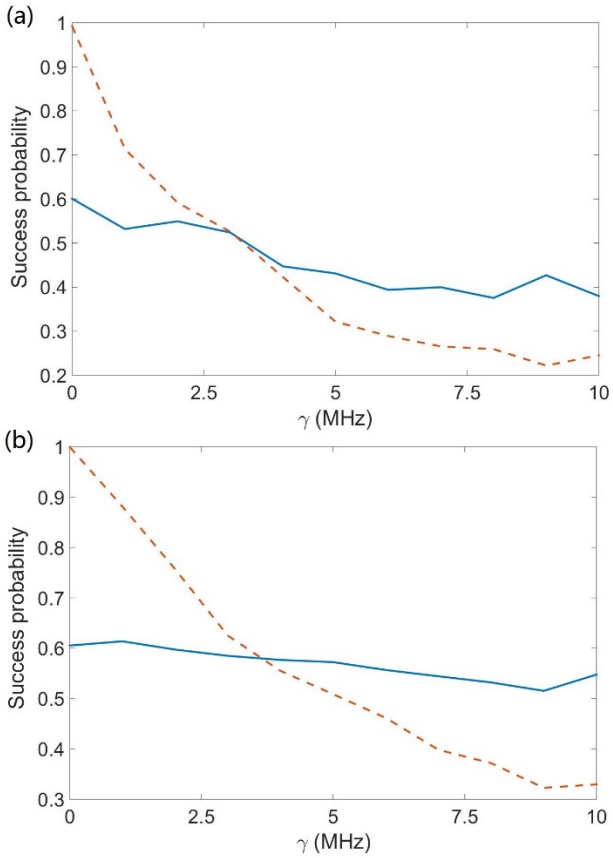

Figure 7.12: Comparison of the success probabilities for 3 logical spins problems with and without error corrections. The red dashed curves are the calculated results without error corrections, while the blue solid curves are applied with error correction method. (a) and (b) are computed for two randomly chosen logical problems by averaging over 500 trajectories. The parameters of the two problems are randomly taken from the interval [-*J*, *J*].

Figure 7.12 shows the comparison of the success probabilities for 3 logical spins problems with and without error corrections. All parameters except the error rate are the same as for Figure 7.11. The measurement strength κ and error rate γ are taken from the experimental parameters [194]. The success probability is computed as the probability of occupation of the correct ground state at $t = \tau$. From both of (a) and (b), the curves with and without error corrections cross each other at $\gamma \approx 3.5$ MHz. For $\gamma < 3.5$ MHz, the average success rate for the annealing protocol without error correction method is higher than that with error corrections. This is due to the errors induced by continuous weak measurements. The finite measurement strength κ will result in unexpected errors and degrade the final readouts. Decreasing κ can reduce the unwanted errors but will lead to longer information-collecting time. When $\gamma > 3.5$ MHz the control feedback method surpasses the one without error corrections and higher averaged success probability can be obtained. As the error rate is larger than the information-collecting rate, both curves exhibit decreasing success probabilities as the error rate grows. However, the results from the error correction method are much better and more stable than the other one, which shows the superiority of the error correction method.

7.3.7 Discussions

Besides the driver Hamiltonian, the back-action brought by the measurements may offer an alternative source of quantum fluctuations for the system to escape local minima and find the global minimum of a given objective function. The effect of the finite measurement strength on enhancing the probability of jumping out of local minima is still an open question. More relevant work is expected to take the effects of weak measurements into considerations for quantum annealing. Further, we do not use other error correction methods during the readout stage as suggested by Fernando Pastawski and John Preskill [196]. With the help of the post-processing method, we can make quantum annealing more robust against errors.

7.3.8 Methods

Realization of continuous weak measurements of stabilizers. There are two ways to realize weak measurements for stabilizers. One way is to use ancillary-based weak measurements [197] which require a quantum circuit composed of several Controlled-NOT and Controlled-Z gates.

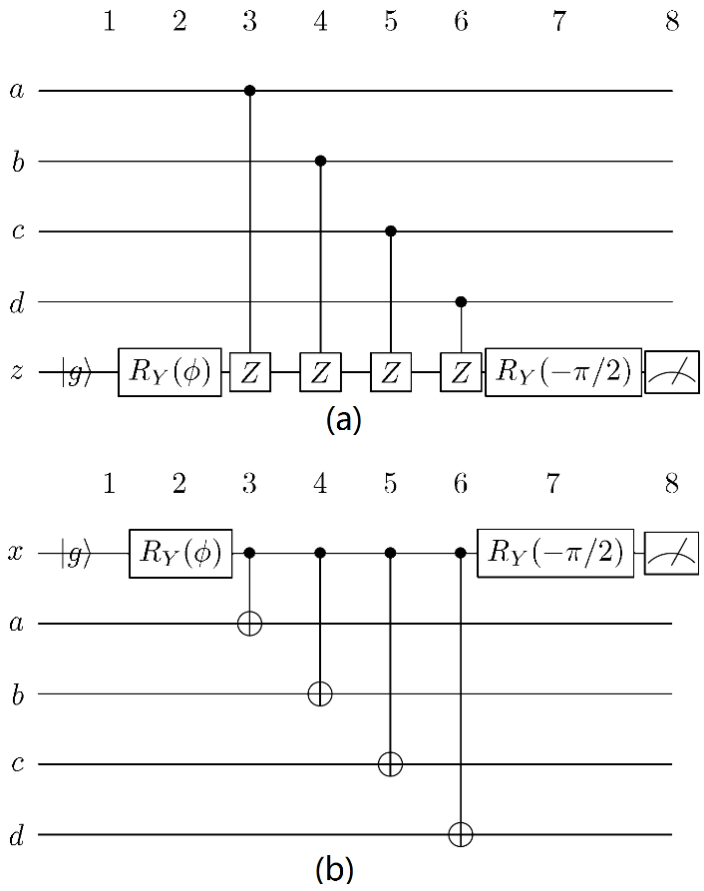

Figure 7.13: The quantum circuit for the ancillary-based weak measurements of (a) $\tilde{\sigma}_Z\tilde{\sigma}_Z\tilde{\sigma}_Z\tilde{\sigma}_Z$ and (b) $\tilde{\sigma}_X\tilde{\sigma}_X\tilde{\sigma}_X\tilde{\sigma}_X$ on neighboring four data qubits. The measurement consists of a variable-amplitude Y rotation by an angle ϕ, which controls the strength of the measurement. The following four CZ gates or CNOTs entangle the ancilla spin with the data spins. Finally, the ancilla is rotated by an angle − π/2, bringing it into the desired measurement basis.

The ancilla measurement protocol is shown in Figure 2. Initially, an ancilla qubit is Y-rotated at an angle $0 \le \phi \le \pi/2$ from its ground state to set the measurement strength. For a weak measurement of S_Z, four control phase gates are performed between the measure spin and data

spins, causing a Z rotation of $\pi/2$ in the ancilla qubit depending on the target qubits' state. We define the operator $S_X^{[i,j]}$ for each plaquette as:

$$S_X^{[i,j]} = \begin{cases} \sigma_X^{(i,j)} \sigma_X^{(i,j-1)} \sigma_X^{(i-1,j)} \sigma_X^{(i-1,j-1)} & \text{if } i+2 \le j \\ \sigma_X^{(i,j)} \sigma_X^{(i-1,j-1)} \sigma_X^{(i-1,j)} & \text{if } i+2 > j \end{cases}. \tag{7.21}$$

Four CNOTs are applied between the measure spin and data spins if a weak measurement of S_X is desired. Finally, a Y rotation of $-\pi/2$ is performed on the ancilla qubit to rotate it into the correct measurement basis. The "visibility" of this measurement is then proportional to the distance of the ancilla state vector from the equator of the Bloch sphere. For $\phi = \pi/2$, this operation implements a projective measurement. As $\phi \to 0$, the ancilla states become degenerate and no information is extracted. As the final position of the ancilla state is dependent on the measurement strength, the ancilla readout is imperfectly correlated with the target qubit. The visibility of an ancilla Z-average, $\langle Z \rangle_\alpha \simeq \sin(\phi) \langle S_Z^{[i,j]} \rangle$ or $\langle Z \rangle_\alpha \simeq \sin(\phi) \langle S_X^{[i,j]} \rangle$ is compressed from the expectation value of the target stabilizer by a factor of approximately $\sin(\phi)$.

The other way to implement the continuous weak measurement of stabilizers is to measure the multi-qubit parity in circuit quantum electrodynamics directly, such as the scheme proposed by David P DiVincenzo and Firat Solgun [198]. In the proposal, coupling four qubits to a common resonator which holds three closely spaced resonances enables us to extract the parity information about the four qubits through the reflected phase function $\theta_S(\omega)$. Thus, directly measuring the parity operator can simplify the process of error correction, and improve its error robustness without the need of ancilla qubits and quantum circuits.

Computation of success probability: In the simulations, the success probability is computed as the probability of occupation of the correct ground state in the reduced density matrix $\hat{\rho}_r(\tau)$ at $t = \tau$. We choose the spins located at (0,1), (0,2), and (0,3) as the readout chain and obtain the reduced density matrix $\hat{\rho}_r(\tau)$ from the final density matrix $\hat{\rho}(\tau)$ of the physical spins array. The correct ground state which is computed from the target optimization problem

$H_T = \sum_{q=1}^{n} h_q \sigma_Z^q + \sum_{p=1}^{n-1} \sum_{q=p+1}^{n} J_{pq} \sigma_Z^p \sigma_Z^q$ will be modified according to the flipped sign of the on-site energy $\tilde{h}_1$, $\tilde{h}_2$, and $\tilde{h}_3$.

In this work, we propose to use weak measurements on stabilizer codes to monitor the sweep of the LHZ quantum annealer with all-to-all connectivity. Bit-flip and phase-flip error chains occurring during an annealing sweep can be determined by decoders and then corrected by changing the following evolving Hamiltonian. By applying a proper constraint strength *R*, it is also possible to distinguish and remedy the jumps from the instantaneous ground state to low-lying excited states. Simulated results are computed with stochastic Schrodinger equations with experimental parameters.

7.4 Summary

We propose a two-dimensional quantum annealing architecture to solve the 4th order binary optimization problem by encoding four-qubit interactions within the coupled local fields acting on a set of physical qubits. All possible four-body coupling terms for an *N*-qubit system can be implemented through this architecture and are readily realizable with the existing superconducting circuit technologies. The overhead of the physical qubits is O(N^4), which is the same as previously proposed architectures in four-dimensional space. The optimization problem is encoded in local fields acting on the qubits and the interactions between them. This allows one to implement an objective Hamiltonian for a high-order binary optimization problem, whose solution is encoded in the topology of the physical qubits. The equivalence between the optimization problem Hamiltonian and the executable Hamiltonian is ensured by a gauge invariant subspace of the experimental system. A scheme to realize local gauge constraint by single ancillary qubit is proposed. This architecture may be used to solve a valuable class of NP-hard problems - the K^{th} order binary optimization problems.

We also propose a method to implement quantum annealing with error correction through stabilizer codes. The stabilizers are realized with weak measurements for real-time, in-run monitoring of spins, to minimize or control the back-action. X and Z error chains occurred during an annealing sweep and jump to low-lying excited states from the instantaneous ground state can

both be identified by decoders and corrected. Furthermore, back-action offers an alternative source of quantum fluctuations in addition to the driver Hamiltonian.

References

[1] Ofek, N., et al., *Extending the lifetime of a quantum bit with error correction in superconducting circuits.* Nature, 2016. **536**(7617): p. 441-445.

[2] Kelly, J., et al., *State preservation by repetitive error detection in a superconducting quantum circuit.* Nature, 2015. **519**(7541): p. 66-69.

[3] Barends, R., et al., *Superconducting quantum circuits at the surface code threshold for fault tolerance.* Nature, 2014. **508**(7497): p. 500-503.

[4] Wallraff, A., et al., *Strong coupling of a single photon to a superconducting qubit using circuit quantum electrodynamics.* Nature, 2004. **431**(7005): p. 162-167.

[5] O□Connell, A.D., et al., *Microwave dielectric loss at single photon energies and millikelvin temperatures.* Applied Physics Letters, 2008. **92**(11): p. 112903.

[6] DiCarlo, L., et al., *Preparation and measurement of three-qubit entanglement in a superconducting circuit.* Nature, 2010. **467**(7315): p. 574-578.

[7] Neeley, M., et al., *Generation of three-qubit entangled states using superconducting phase qubits.* Nature, 2010. **467**(7315): p. 570-573.

[8] Sillanpää, M.A., J.I. Park, and R.W. Simmonds, *Coherent quantum state storage and transfer between two phase qubits via a resonant cavity.* Nature, 2007. **449**(7161): p. 438-442.

[9] DiCarlo, L., et al., *Demonstration of two-qubit algorithms with a superconducting quantum processor.* Nature, 2009. **460**(7252): p. 240-244.

[10] Reed, M.D., et al., *Realization of three-qubit quantum error correction with superconducting circuits.* Nature, 2012. **482**(7385): p. 382-385.

[11] Blais, A., et al., *Cavity quantum electrodynamics for superconducting electrical circuits: An architecture for quantum computation.* Physical Review A, 2004. **69**(6): p. 062320.

[12] Baselmans, J.J.A., S.J.C. Yates, and D.P. Korte, *Development of high-Q superconducting resonators for use as kinetic inductance detectors.* Development of high-Q superconducting resonators for use as kinetic inductance detectors, 2007.

[13] Mazin, B.A., et al., *Position sensitive x-ray spectrophotometer using microwave kinetic inductance detectors.* Applied physics letters, 2006. **89**(22): p. 222507.

[14] McDermott, R., et al., *Simultaneous state measurement of coupled Josephson phase qubits.* Science, 2005. **307**(5713): p. 1299-1302.

[15] Sigillito, A.J., et al., *Fast, low-power manipulation of spin ensembles in superconducting microresonators.* Applied Physics Letters, 2014. **104**(22): p. 222407.

[16] Ranjan, V., et al., *Probing dynamics of an electron-spin ensemble via a superconducting resonator.* Physical review letters, 2013. **110**(6): p. 67004.

[17] Benningshof, O.W., et al., *Superconducting microstrip resonator for pulsed ESR of thin films.* Journal of Magnetic Resonance, 2013. **230**: p. 84-87.

[18] Wallace, W.J. and R.H. Silsbee, *Microstrip resonators for electron‐spin resonance.* Review of Scientific Instruments, 1991. **62**(7): p. 1754-1766.

[19] Narkowicz, R., D. Suter, and R. Stonies, *Planar microresonators for EPR experiments.* Journal of Magnetic Resonance, 2005. **175**(2): p. 275-284.

[20] Sigillito, A.J., et al., *Fast, low-power manipulation of spin ensembles in superconducting microresonators.* Applied Physics Letters, 2014. **104**(22): p. 222407.

[21] Artzi, Y., Y. Twig, and A. Blank, *Induction-detection electron spin resonance with spin sensitivity of a few tens of spins.* Applied Physics Letters, 2015. **106**(8): p. 084104.

[22] Benningshof, O.W.B., et al., *Superconducting microstrip resonator for pulsed ESR of thin films.* Journal of Magnetic Resonance, 2013. **230**: p. 8487.

[23] Bienfait, A., et al., *Reaching the quantum limit of sensitivity in electron spin resonance.* Nature Nanotechnology, 2016. **11**(3): p. 253-257.

[24] Borneman, T.W., C.E. Granade, and D.G. Cory, *Parallel Information Transfer in a Multinode Quantum Information Processor.* Physical Review Letters, 2012. **108**(14): p. 140502.

[25] Leuenberger, M.N. and D. Loss, *Quantum computing in molecular magnets.* Nature, 2001. **410**(6830): p. 789-793.

[26] Lloyd, S., *A Potentially Realizable Quantum Computer.* Science, 1993. **261**(5128): p. 1569-1571.

[27] Kane, B.E., *A silicon-based nuclear spin quantum computer.* Nature, 1998. **393**(6681): p. 133-137.

[28] Harneit, W., et al., *Architectures for a Spin Quantum Computer Based on Endohedral Fullerenes.* physica status solidi (b), 2002. **233**(3): p. 453-461.

[29] Twamley, J., *Quantum-cellular-automata quantum computing with endohedral fullerenes.* Physical Review A, 2003. **67**(5): p. 052318.

[30] Mehring, M. and J. Mende, *Spin-bus concept of spin quantum computing.* Physical Review A, 2006. **73**(5): p. 052303.

[31] Cappellaro, P., et al., *Coherence and Control of Quantum Registers Based on Electronic Spin in a Nuclear Spin Bath.* Physical Review Letters, 2009. **102**(21): p. 210502.

[32] Wood, C.J., T.W. Borneman, and D.G. Cory, *Cavity cooling of an ensemble spin system.* Cavity cooling of an ensemble spin system, 2014.

[33] Wallraff, A., et al., *Quantum dynamics of a single vortex.* Nature, 2003. **425**(6954): p. 155-158.

[34] Song, C., et al., *Microwave response of vortices in superconducting thin films of Re and Al.* Physical Review B, 2009. **79**(17): p. 174512.

[35] Saito, K., *Critical field limitation of the niobium superconducting RF cavity.* Critical field limitation of the niobium superconducting RF cavity, 2001.

[36] Quateman, J.H., *T c suppression and critical fields in thin superconducting Nb films.* Physical Review B, 1986. **34**(3): p. 1948.

[37] Tinkham, M., *Introduction to Superconductivity: (Dover Books on Physics)(Vol i).* Introduction to Superconductivity: (Dover Books on Physics)(Vol i), 2004.

[38] Baselmans, J., et al., *Noise and sensitivity of aluminum kinetic inductance detectors for sub-mm astronomy.* Journal of Low Temperature Physics, 2008. **151**(1-2): p. 524-529.

[39] Gao, J., et al., *Experimental evidence for a surface distribution of two-level systems in superconducting lithographed microwave resonators.* Applied Physics Letters, 2008. **92**(15): p. 152505.

[40] Healey, J.E., et al., *Magnetic field tuning of coplanar waveguide resonators.* Applied Physics Letters, 2008. **93**(4): p. 43513.

[41] Barends, R. and J.J.A. Baselmans, *Niobium and tantalum high Q resonators for photon detectors.* Niobium and tantalum high Q resonators for photon detectors, 2007.

[42] Wang, H., et al., *Improving the coherence time of superconducting coplanar resonators.* Applied Physics Letters, 2009. **95**(23): p. 233508.

[43] Vissers, M.R., et al., *Low loss superconducting titanium nitride coplanar waveguide resonators.* Applied Physics Letters, 2010. **97**(23): p. 232509.

[44] Megrant, A., et al., *Planar superconducting resonators with internal quality factors above one million.* Applied Physics Letters, 2012. **100**(11): p. 113510.

[45] Cory, D.G., A.F. Fahmy, and T.F. Havel, *Ensemble quantum computing by NMR spectroscopy.* Proceedings of the National Academy of Sciences, 1997. **94**(5): p. 1634-1639.

[46] Gershenfeld, N.A. and I.L. Chuang, *Bulk Spin-Resonance Quantum Computation.* Science, 1997. **275**(5298): p. 350-356.

[47] Jones, J.A., *NMR Quantum Computation: A Critical Evaluation.* Fortschritte der Physik, 2000. **48**(9-11): p. 909-924.

[48] Warren , W.S., *The Usefulness of NMR Quantum Computing.* Science, 1997. **277**(5332): p. 1688-1690.

[49] Braunstein, S.L., et al., *Separability of Very Noisy Mixed States and Implications for NMR Quantum Computing.* Physical Review Letters, 1999. **83**(5): p. 1054-1057.

[50] Cory, D.G., et al., *NMR Based Quantum Information Processing: Achievements and Prospects.* Fortschritte der Physik, 2000. **48**(9-11): p. 875-907.

[51] Beton, P.H., A.W. Dunn, and P. Moriarty, *Manipulation of C60 molecules on a Si surface.* Applied Physics Letters, 1995. **67**(8): p. 1075-1077.

[52] Schofield, S.R., et al., *Atomically Precise Placement of Single Dopants in Si.* Physical Review Letters, 2003. **91**(13): p. 136104.

[53] Tyryshkin, A.M., et al., *Electron spin relaxation times of phosphorus donors in silicon.* Physical Review B, 2003. **68**(19): p. 193207.

[54] Tyryshkin, A.M., et al., *Coherence of spin qubits in silicon.* Journal of Physics: Condensed Matter, 2006. **18**(21): p. S783.

[55] Morton, J.J.L., et al., *Solid-state quantum memory using the 31P nuclear spin.* Nature, 2008. **455**(7216): p. 1085-1088.

[56] McCamey, D.R., et al., *Fast Nuclear Spin Hyperpolarization of Phosphorus in Silicon.* Physical Review Letters, 2009. **102**(2): p. 027601.

[57] Morley, G.W., et al., *The initialization and manipulation of quantum information stored in silicon by bismuth dopants.* Nat Mater, 2010. **9**(9): p. 725-729.

[58] Simmons, S., et al., *Entanglement in a solid-state spin ensemble.* Nature, 2011. **470**(7332): p. 69-72.

[59] Witzel, W., et al., *Quantum control of hybrid nuclear-electronic qubits.* Nature, 2011: p. Medium: X; Size: 21 p.

[60] Harneit, W., *Fullerene-based electron-spin quantum computer.* Physical Review A, 2002. **65**(3): p. 032322.

[61] Suter, D. and K. Lim, *Scalable architecture for spin-based quantum computers with a single type of gate.* Physical Review A, 2002. **65**(5): p. 052309.

[62] Popov, A.A., *Endohedral Fullerenes: Electron Transfer and Spin*. 2017, Springer.

[63] Bardeen, J., L.N. Cooper, and J.R. Schrieffer, *Microscopic Theory of Superconductivity.* Physical Review, 1957. **106**(1): p. 162-164.

[64] Bardeen, J., L.N. Cooper, and J.R. Schrieffer, *Theory of Superconductivity.* Physical Review, 1957. **108**(5): p. 1175-1204.

[65] Bogoliubov, N., *New method in the theory of superconductivity. III.* Sov. Phys. JETP, 1958. **7**: p. 51.

[66] De Gennes, P.G., *Superconductivity of metals and alloys*. 1989: Addison-Wesley.

[67] Landau, L.D. and V. Ginzburg, *On the theory of superconductivity.* Zh. Eksp. Teor. Fiz., 1950. **20**: p. 1064.

[68] Gor'kov, L.P., *Microscopic derivation of the Ginzburg-Landau equations in the theory of superconductivity.* Sov. Phys. JETP, 1959. **9**(6): p. 1364-1367.

[69] Gorkov, L., *On the energy spectrum of superconductors.* Sov. Phys. JETP, 1958. **7**(505): p. 158.

[70] Eilenberger, G., *Transformation of Gorkov's equation for type II superconductors into transport-like equations.* Zeitschrift für Physik A Hadrons and nuclei, 1968. **214**(2): p. 195-213.

[71] Larkin, A. and Y.N. Ovchinnikov, *Quasiclassical method in the theory of superconductivity*. Sov Phys JETP, 1969. **28**(6): p. 1200-1205.

[72] Abrikosov, A. and L. Gorkov, *On the theory of superconducting alloys. 1. The electrodynamics of alloys at absolute zero.* Sov. Phys. JETP, 1959. **8**: p. 1090-1098.

[73] Usadel, K.D., *Generalized Diffusion Equation for Superconducting Alloys.* Physical Review Letters, 1970. **25**(8): p. 507-509.

[74] Golubov, A.A., et al., *Proximity effect in superconductor-insulator-superconductor Josephson tunnel junctions: Theory and experiment.* Physical Review B, 1995. **51**(2): p. 1073-1089.

[75] Abrikosov, A.A., L.P. Gorkov, and I.E. Dzyaloshinski, *Methods of quantum field theory in statistical physics*. 2012: Courier Corporation.

[76] Brammertz, G., et al., *Generalized proximity effect model in superconducting bi- and trilayer films.* Journal of Applied Physics, 2001. **90**(1): p. 355-364.

[77] Meissner, H., *Superconductivity of Contacts with Interposed Barriers.* Physical Review, 1960. **117**(3): p. 672-680.

[78] Schmidt, V.V.e., *The physics of superconductors: Introduction to fundamentals and applications*. 2013: Springer Science & Business Media.

[79] Rammer, J. and H. Smith, *Quantum field-theoretical methods in transport theory of metals.* Reviews of Modern Physics, 1986. **58**(2): p. 323-359.

[80] Zaitsev, A., *Quasiclassical equations of the theory of superconductivity for contiguous metals and the properties of constricted microcontacts.* Zh. Eksp. Teor. Fiz, 1984. **86**: p. 1742-1758.

[81] Larkin, A. and Y. Ovchinnikov, *Nonlinear conductivity of superconductors in the mixed state.* Sov. Phys. JETP, 1975. **41**(5): p. 960-965.

[82] Larkin, A. and Y. Ovchinnikov, *Non-linear effects during the motion of vortices in superconductors.* Zh. Eksp. Teor. Fiz., 1977. **73**(1): p. 7.

[83] Eliashberg, G., *Inelastic electron collisions and nonequilibrium stationary states in superconductors.* SOV PHYS JETP, 1972. **34**(3): p. 668-676.

[84] Schmid, A. and G. Schön, *Linearized kinetic equations and relaxation processes of a superconductor near T c.* Journal of Low Temperature Physics, 1975. **20**(1): p. 207-227.

[85] Andreev, A., *Thermal conductivity of the intermediate state of superconductors.* Zh. Eksperim. i Teor. Fiz., 1964. **46**.

[86] Klapwijk, T.M., *Proximity Effect From an Andreev Perspective.* Journal of Superconductivity, 2004. **17**(5): p. 593-611.

[87] Likharev, K. and L. Iakobson, *Steady-state properties of superconducting bridges.* Soviet Physics Technical Physics, 1976. **20**: p. 950-954.

[88] Pippard, A.B. *The surface impedance of superconductors and normal metals at high frequencies. II. The anomalous skin effect in normal metals*. in *Proceedings of the Royal Society of London A: Mathematical, Physical and Engineering Sciences*. 1947.

[89] Kajfez, D., *Q factor measurements using Matlab*. 2011: Artech House.

[90] Matick, R.E., *Transmission lines for digital and communication networks: an introduction to transmission lines, high-frequency and high-speed pulse characteristics and applications*. 1969: McGraw-Hill.

[91] Kerr, A., *Surface impedance of superconductors and normal conductors in EM simulators.* MMA Memo, 1999. **21**(245): p. 1-17.

[92] Ward, J., et al. *SuperMix: A flexible software library for high-frequency circuit simulation, including SIS mixers and superconducting elements*. in *Proceedings, Tenth International Symposium on Space Terahertz Technology*. 1999.

[93] Zimmermann, W., et al., *Optical Conductivity of Bcs Superconductors with Arbitrary Purity.* Physica C-Superconductivity and Its Applications, 1991. **183**(1-3): p. 99-104.

[94] Noguchi, T., T. Suzuki, and T. Tamura, *Subgap tunneling current at low temperature in Nb/Al-AlN/Nb SIS junctions.* Applied Superconductivity, IEEE Transactions on, 2011. **21**(3): p. 756-759.

[95] Lee, W., D. Rainer, and W. Zimmermann, *Holstein effect in the far-infrared conductivity of high Tc superconductors.* Physica C: Superconductivity, 1989. **159**(5): p. 535-544.

[96] Gao, J., *The physics of superconducting microwave resonators*. 2008, California Institute of Technology.

[97] Noguchi, T., M. Naruse, and Y. Sekimoto, *Contribution of Quasiparticles in the Subgap States to the Surface Impedance of Superconductors.* IEEE Trans. Appl. Supercond., 2013. **23**(3).

[98] Kawakami, A., et al., *Estimation of surface resistance for epitaxial NbN films in the frequency range of 0.1-1.1 THz.* Applied Superconductivity, IEEE Transactions on, 2003. **13**(2): p. 1147-1150.

[99] Kawakami, A., Z. Wang, and S. Miki, *Fabrication and characterization of epitaxial NbN/MgO/NbN Josephson tunnel junctions.* Journal of Applied Physics, 2001. **90**(9): p. 4796-4799.

[100] Juang, J.Y., et al., *Effects of ion irradiation on the normal state and superconducting properties of NbN thin films.* Phys. Rev. B, 1988. **38**: p. 2354-2361.

[101] Tu, M.P., et al., *rf characterization of thermally diffused superconducting niobium nitride.* Journal of applied physics, 1988. **63**(9): p. 4586-4590.

[102] Noguchi, T., et al., *Contribution of the imaginary part of the superconducting gap energy on the SIS tunneling current.* Physica C: Superconductivity, 2009. **469**(15): p. 1585-1588.

[103] Mattis, D.C. and J. Bardeen, *Theory of the anomalous skin effect in normal and superconducting metals.* Physical Review, 1958. **111**(2): p. 412.

[104] Gu\'e, r., S., et al., *Superconducting proximity effect probed on a mesoscopic length scale.* Physical review letters, 1996. **77**(14): p. 3025.

[105] Mohebbi, H.R., et al., *Composite arrays of superconducting microstrip line resonators.* Journal of Applied Physics, 2014. **115**(9): p. 094502.

[106] Kihlstrom, K.E., R.W. Simon, and S.A. Wolf, *Tunneling Î±2F(Ï‰) on high Tc A15} and B1} compounds.* Physica B+C, 1985. **135**(1â€?3): p. 198 - 202.

[107] Poole, C.K., H.A. Farach, and R.J. Creswick, *Handbook of superconductivity.* Handbook of superconductivity, 1999.

[108] Leduc, H.G., et al., *Titanium nitride films for ultrasensitive microresonator detectors.* Applied Physics Letters, 2010. **97**(10): p. 102509.

[109] Creedon, D.L., et al., *High Q-factor sapphire whispering gallery mode microwave resonator at single photon energies and millikelvin temperatures.* Applied Physics Letters, 2011. **98**(22): p. 222903.

[110] McMillan, W.L., *Tunneling Model of the Superconducting Proximity Effect.* Physical Review, 1968. **175**(2): p. 537-542.

[111] Cherkez, V., et al., *Proximity Effect between Two Superconductors Spatially Resolved by Scanning Tunneling Spectroscopy.* Physical Review X, 2014. **4**(1): p. 011033.

[112] Quirion, D., F. Lefloch, and M. Sanquer, *Proximity Effect in Planar TiN-Silicon Junctions.* Journal of Low Temperature Physics, 2000. **120**(5): p. 361-380.

[113] Pracht, U.S., et al., *Direct observation of the superconducting gap in a thin film of titanium nitride using terahertz spectroscopy*. Physical Review B, 2012. **86**(18): p. 184503.

[114] Jin, B.Y. and J.B. Ketterson, *Artificial metallic superlattices.* Advances in Physics, 1989. **38**(3): p. 189-366.

[115] Aarts, J., et al., *Interface transparency of superconductor/ferromagnetic multilayers.* Physical Review B, 1997. **56**(5): p. 2779-2787.

[116] Cirillo, C., et al., *Proximity effect in superconductor/highly paramagnetic Nb/Pd systems.* Physica C: Superconductivity, 2004. **404**(1–4): p. 95-98.

[117] Schöck, M., C. Sürgers, and H. Löhneysen, *Superconducting and magnetic properties of Nb/Pd 1-xFex/Nb triple layers.* The European Physical Journal B- …, 2000.

[118] Medlin, D.L., et al., *Orientation relationships in heteroepitaxial aluminum films on sapphire.* Thin Solid Films, 1997. **299**(1–2): p. 110-114.

[119] Lloyd, S.J., et al., *Growth of niobium nitride/aluminium nitride trilayers and multilayers.* Philosophical Magazine A, 2001. **81**(10): p. 2317-2335.

[120] Tang, Y.C. and O.W.B. Benningshof, *Evaluation of quality factors in superconductor microresonators with proximity enhancement.* Evaluation of quality factors in superconductor microresonators with proximity enhancement, 2014.

[121] Barends, R., et al., *Contribution of dielectrics to frequency and noise of NbTiN superconducting resonators.* Applied Physics Letters, 2008. **92**(22): p. 223502.

[122] Miller, P.B., *Penetration Depth in Impure Superconductors.* Physical Review, 1959. **113**(5): p. 1209-1212.

[123] Eliashberg, G.M., G.V. Klimovitch, and A.V. Rylyakov, *On the temperature dependence of the London penetration depth in a superconductor.* Journal of Superconductivity, 1991. **4**(5): p. 393-396.

[124] Ohya, S., et al., *Room temperature deposition of sputtered TiN films for superconducting coplanar waveguide resonators.* Superconductor Science and Technology, 2014. **27**(1): p. 015009.

[125] Ljungcrantz, H., et al., *Nanoindentation studies of single - crystal (001) - , (011) - , and (111) - oriented TiN layers on MgO.* Journal of Applied Physics, 1996. **80**(12): p. 6725-6733.

[126] Kaplan, S.B., et al., *Quasiparticle and phonon lifetimes in superconductors.* Physical Review B, 1976. **14**(11): p. 4854.

[127] Lutchyn, R., L. Glazman, and A. Larkin, *Quasiparticle decay rate of Josephson charge qubit oscillations.* Physical Review B, 2005. **72**(1): p. 014517.

[128] Martinis, J.M., M. Ansmann, and J. Aumentado, *Energy Decay in Superconducting Josephson-Junction Qubits from Nonequilibrium Quasiparticle Excitations.* Physical Review Letters, 2009. **103**(9): p. 097002.

[129] Dynes, R.C., V. Narayanamurti, and J.P. Garno, *Direct Measurement of Quasiparticle-Lifetime Broadening in a Strong-Coupled Superconductor.* Phys. Rev. Lett., 1978. **41**: p. 1509-1512.

[130] Mitrovi\'c, Bo\vz,,idar and L.A. Rozema, *On the correct formula for the lifetime broadened superconducting density of states.* Journal of Physics: Condensed Matter, 2007. **20**(1): p. 015215.

[131] Scalapino, D.J., *Superconductivity: Part 1 (In Two Parts)*, R.D. Parks, Editor. 1969, Taylor \& Francis. p. 449.

[132] Eliashberg, G.M., *Interactions between Electrons and Lattice Vibrations in a Superconductor.* Soviet Physics Jetp-Ussr, 1960. **11**(3): p. 696-702.

[133] Arnold, G.B. and M. Menon, *The Local Phonon Density of States and Its Influence on Superconducting Properties.* Journal De Physique, 1981. **42**(Nc6): p. 377-379.

[134] Rothwarf, A., *Size Effects in Quasiparticle Lifetimes and Phonon Generation in Superconductors.* Physical Review Letters, 1969. **23**(9): p. 468-&.

[135] Pokatilov, E.P., D.L. Nika, and A.A. Balandin, *Phonon spectrum and group velocities in AlN/GaN/AlN and related heterostructures.* Superlattices and Microstructures, 2003. **33**(3): p. 155-171.

[136] Virieux, J., *P-SV wave propagation in heterogeneous media: Velocity - stress finite - difference method.* GEOPHYSICS, 1986. **51**(4): p. 889-901.

[137] Vallin, J., et al., *Elastic constants of aluminum.* Journal of Applied Physics, 1964. **35**(6): p. 1825-1826.

[138] Brammertz, G., et al., *Critical temperature of superconducting bilayers: Theory and experiment.* Applied Physics Letters, 2002. **80**(16): p. 2955-2957.

[139] Tang, Y.-C., et al., *Superconducting Resonators Based on TiN/Tapering/NbN/Tapering/TiN Heterostructures.* Advanced Engineering Materials, 2016. **18**(10): p. 1816-1822.

[140] Tang, Y.-C., et al. *Evaluation of quality factors in superconductor microresonators with proximity enhancement*. in *14th IEEE International Conference on Nanotechnology*. 2014.

[141] Kelly, J., et al., *State preservation by repetitive error detection in a superconducting quantum circuit.* Nature, 2015. **519**(7541): p. 66-69.

[142] Córcoles, A.D., et al., *Demonstration of a quantum error detection code using a square lattice of four superconducting qubits.* Nature Communications, 2015. **6**: p. 6979.

[143] Bravyi, S.B. and A.Y. Kitaev, *Quantum codes on a lattice with boundary.* arXiv preprint quant-ph/9811052, 1998.

[144] Freedman, M.H., *Quantum Computation and the Localization of Modular Functors.* Foundations of Computational Mathematics, 2001. **1**(2): p. 183-204.

[145] Dennis, E., et al., *Topological quantum memory.* Journal of Mathematical Physics, 2002. **43**(9): p. 4452-4505.

[146] Wang, C., J. Harrington, and J. Preskill, *Confinement-Higgs transition in a disordered gauge theory and the accuracy threshold for quantum memory.* Annals of Physics, 2003. **303**(1): p. 31-58.

[147] Wang, D.S., A.G. Fowler, and L.C.L. Hollenberg, *Surface code quantum computing with error rates over 1%.* Physical Review A, 2011. **83**(2): p. 020302.

[148] Fowler, A.G., A.C. Whiteside, and L.C.L. Hollenberg, *Towards Practical Classical Processing for the Surface Code.* Physical Review Letters, 2012. **108**(18): p. 180501.

[149] Spedalieri, F.M. and V.P. Roychowdhury, *Latency in local, two-dimensional, fault-tolerant quantum computing.* Quantum Info. Comput., 2009. **9**(7): p. 666-682.

[150] Svore, K.M., D.P. Divincenzo, and B.M. Terhal, *Noise threshold for a fault-tolerant two-dimensional lattice architecture.* Quantum Info. Comput., 2007. **7**(4): p. 297-318.

[151] Fowler, A.G., et al., *Surface codes: Towards practical large-scale quantum computation.* Physical Review A, 2012. **86**(3): p. 032324.

[152] Boixo, S., et al., *Evidence for quantum annealing with more than one hundred qubits.* Nat Phys, 2014. **10**(3): p. 218-224.

[153] Ghosh, J. and A.G. Fowler, *Leakage-resilient approach to fault-tolerant quantum computing with superconducting elements.* Physical Review A, 2015. **91**(2): p. 020302.

[154] Harris, R., et al., *Experimental demonstration of a robust and scalable flux qubit.* Physical Review B, 2010. **81**(13): p. 134510.

[155] Harris, R., et al., *Compound Josephson-junction coupler for flux qubits with minimal crosstalk.* Physical Review B, 2009. **80**(5): p. 052506.

[156] Alec Maassen van den, B., A.J. Berkley, and M. Yalowsky, *Mediated tunable coupling of flux qubits.* New Journal of Physics, 2005. **7**(1): p. 230.

[157] Barends, R., et al., *Coherent Josephson Qubit Suitable for Scalable Quantum Integrated Circuits.* Physical Review Letters, 2013. **111**(8): p. 080502.

[158] Chen, Y., et al., *Qubit Architecture with High Coherence and Fast Tunable Coupling.* Physical Review Letters, 2014. **113**(22): p. 220502.

[159] Edmonds, J., *Maximum matching and a polyhedron with 0, 1-vertices.* Journal of Research of the National Bureau of Standards B, 1965. **69**(125-130): p. 55-56.

[160] Edmonds, J., *Paths, trees, and flowers.* Canadian Journal of mathematics, 1965. **17**(3): p. 449-467.

[161] Denchev, V.S., et al., *What is the Computational Value of Finite-Range Tunneling?* Physical Review X, 2016. **6**(3): p. 031015.

[162] Geller, M.R., et al., *Universal quantum simulation with prethreshold superconducting qubits: Single-excitation subspace method.* Physical Review A, 2015. **91**(6): p. 062309.

[163] Harris, R., et al., *Experimental investigation of an eight-qubit unit cell in a superconducting optimization processor.* Physical Review B, 2010. **82**(2): p. 024511.

[164] Brooke, J., et al., *Quantum annealing of a disordered magnet.* Science, 1999. **284**(5415): p. 779-781.

[165] Farhi, E., et al., *Quantum computation by adiabatic evolution.* arXiv preprint quant-ph/0001106, 2000.

[166] R\o, n., Troels F., et al., *Defining and detecting quantum speedup.* Science, 2014. **345**(6195): p. 420-424.

[167] Johnson, M.W., et al., *Quantum annealing with manufactured spins.* Nature, 2011. **473**(7346): p. 194-198.

[168] Santoro, G.E., et al., *Theory of quantum annealing of an Ising spin glass.* Science, 2002. **295**(5564): p. 2427-2430.

[169] Lidar, D.A., *Towards fault tolerant adiabatic quantum computation.* Physical Review Letters, 2008. **100**(16): p. 160506.

[170] Boixo, S., et al., *Computational multiqubit tunnelling in programmable quantum annealers.* Nature communications, 2016. **7**.

[171] Farhi, E., et al., *A quantum adiabatic evolution algorithm applied to random instances of an NP-complete problem.* Science, 2001. **292**(5516): p. 472-475.

[172] Marto\vn, \'a,k, Roman, G.E. Santoro, and E. Tosatti, *Quantum annealing of the traveling-salesman problem.* Physical Review E, 2004. **70**(5): p. 057701.

[173] Perdomo-Ortiz, A., et al., *Finding low-energy conformations of lattice protein models by quantum annealing.* Scientific reports, 2012. **2**.

[174] Bian, Z., et al., *Experimental determination of Ramsey numbers.* Physical review letters, 2013. **111**(13): p. 130505.

[175] Babbush, R., P.J. Love, and A.a. Aspuru-Guzik, n, *Adiabatic quantum simulation of quantum chemistry.* Scientific reports, 2014. **4**.

[176] Dickson, N.G., et al., *Thermally assisted quantum annealing of a 16-qubit problem.* Nature communications, 2013. **4**: p. 1903.

[177] Boixo, S., et al., *Experimental signature of programmable quantum annealing.* Nature communications, 2013. **4**.

[178] Lechner, W., P. Hauke, and P. Zoller, *A quantum annealing architecture with all-to-all connectivity from local interactions.* Science advances, 2015. **1**(9): p. e1500838.

[179] Pudenz, K.L., T. Albash, and D.A. Lidar, *Error-corrected quantum annealing with hundreds of qubits.* Nature communications, 2014. **5**.

[180] Pudenz, K.L., T. Albash, and D.A. Lidar, *Quantum annealing correction for random Ising problems.* Physical Review A, 2015. **91**(4): p. 042302.

[181] Wegner, F.J., *Duality in Generalized Ising Models and Phase Transitions without Local Order Parameters.* Journal of Mathematical Physics, 1971. **12**(10): p. 2259-2272.

[182] Kogut, J.B., *An introduction to lattice gauge theory and spin systems.* Reviews of Modern Physics, 1979. **51**(4): p. 659-713.

[183] Rocchetto, A., S.C. Benjamin, and Y. Li, *Stabilizers as a design tool for new forms of the Lechner-Hauke-Zoller annealer*. Science Advances, 2016. **2**(10).

[184] Lidar, D.A. and T.A. Brun, *Quantum error correction*. 2013: Cambridge University Press.

[185] Aharonov, Y., D.Z. Albert, and L. Vaidman, *How the result of a measurement of a component of the spin of a spin-1/2 particle can turn out to be 100.* Physical Review Letters, 1988. **60**(14): p. 1351-1354.

[186] Hatridge, M., et al., *Quantum Back-Action of an Individual Variable-Strength Measurement.* Science, 2013. **339**(6116): p. 178-181.

[187] White, T.C., et al., *Preserving entanglement during weak measurement demonstrated with a violation of the Bell–Leggett–Garg inequality.* Npj Quantum Information, 2016. **2**: p. 15022.

[188] Dressel, J. and A.N. Korotkov, *Avoiding loopholes with hybrid Bell-Leggett-Garg inequalities.* Physical Review A, 2014. **89**(1): p. 012125.

[189] Kogut, J. and L. Susskind, *Hamiltonian formulation of Wilson's lattice gauge theories.* Physical Review D, 1975. **11**(2): p. 395.

[190] Pastawski, F. and J. Preskill, *Error correction for a proposed quantum annealing architecture, arXiv preprint.* arXiv preprint arXiv:1511.00004, 2015.

[191] Coleman, S., *Fate of the false vacuum: Semiclassical theory.* Physical Review D, 1977. **15**(10): p. 2929-2936.

[192] Vaĭnshteĭn, A.I., et al., *ABC of instantons.* Soviet Physics Uspekhi, 1982. **25**(4): p. 195.

[193] Nagaosa, N., *Quantum field theory in condensed matter physics*. 2013: Springer Science & Business Media.

[194] Sarovar, M., et al., *Practical scheme for error control using feedback.* Physical Review A, 2004. **69**(5): p. 052324.

[195] Gardiner, C.W., *Handbook of stochastic methods for physics, chemistry and the natural sciences, vol. 13 of.* Springer series in synergetics, 1985.

[196] Pastawski, F. and J. Preskill, *Error correction for encoded quantum annealing.* Physical Review A, 2016. **93**(5): p. 052325.

[197] Cramer, J., et al., *Repeated quantum error correction on a continuously encoded qubit by real-time feedback.* Nature Communications, 2016. **7**: p. 11526.

[198] David, P.D. and S. Firat, *Multi-qubit parity measurement in circuit quantum electrodynamics.* New Journal of Physics, 2013. **15**(7): p. 075001.

[199] Facchi, P. and S. Pascazio, *Quantum Zeno Subspaces.* Physical Review Letters, 2002. **89**(8): p. 080401.

[200] Facchi, P. and S. Pascazio, *Quantum Zeno dynamics: mathematical and physical aspects.* Journal of Physics A: Mathematical and Theoretical, 2008. **41**(49): p. 493001.

[201] Suzuki, S. and M. Okada, *Simulated Quantum Annealing by the Real-time Evolution*, in *Quantum Annealing and Other Optimization Methods*, A. Das and B. K. Chakrabarti, Editors. 2005, Springer Berlin Heidelberg: Berlin, Heidelberg. p. 207-238.

Appendix A
Effective constraint Hamiltonian

A unitary encoding circuit rotates the state of the spins array into a subspace of a larger Hilbert space, which is equivalent to an effective constraint Hamiltonian applied on all of the data qubits. Using quantum Zeno dynamics (QZD) [199, 200], we may realize an effective constraint Hamiltonian with infinite strength with repetitive stabilizer measurements on a square-lattice spins array topology. The infinite-strength constraints can ensure that the low energy spectrum of the Hamiltonian of the mapped all-to-all connectivity is the same as the original logical Hamiltonian.

The time-evolution of a state $|\psi(t)\rangle$ is governed by the Schrodinger equation. In particular, an evolution during a short time Δt is written using a single time-evolution operator as $|\psi(t+\Delta t)\rangle \cong e^{-i\mathcal{H}(t)\Delta t}|\psi(t)\rangle$. If we consider a period from $t=0$ to $t=T$, the evolution is described by the unitary operator $U(T) \cong \mathcal{T}\{\prod_{k=0}^{N-1}\exp[-i\mathcal{H}(k\Delta t)\Delta t]\}$, where the Trotter number N satisfies $N\Delta t = T$, $\mathcal{T}$ denotes time ordering. Denote $\mathscr{H}$ as the Hilbert space of $\mathcal{H}(t)$ and $\mathscr{H}_P = P\mathscr{H}P$ is the subspace spanned by the eigenstates of P. Let the density matrix $\rho_0 = |\psi_0\rangle\langle\psi_0|$ belongs to $\mathscr{H}_P$ at $t=0$. To be noted here, the projection operator P is multi-dimensional. We perform a series of observations P at times $t_k = k\Delta t$ $(\mathrm{k}=0,\cdots,N-1)$. The state of Q after the N measurements reads $\rho(T) = V_N(T)\rho_0 V_N^+(T)$, where $V_N(T) = \mathcal{T}\{\prod_{k=0}^{N-1}[Pe^{-i\mathcal{H}(t_k)\Delta t}P]\}$. The probability to find the system in $\mathscr{H}_P$ is given by $p_N(T) = \mathrm{Tr}[V_N(T)\rho_0 V_N^+(T)]$, which is the probability that the system remains in $\mathscr{H}_P$. There is a likelihood $1-p_N$ that the system has made a transition outside $\mathscr{H}_P$, and its state has changed into $\rho'(T)$. The state $\rho(T)$ and $\rho'(T)$ together make up a block diagonal matrix: The initial density matrix is reduced to a mixture, and any possibility of interference between the states inside and outside $\mathscr{H}_P$ is destroyed (complete decoherence). It is shown that repeated observations in succession modify the dynamics of the quantum system; under general conditions, if N is

sufficiently large, all transitions outside $\mathscr{H}_P$ are inhibited. It should be noted that the dynamics are not reversible. To consider the $N \to \infty$ limit ('continuous observation'), we assume that $t_\infty = T$ and the limit $\mathscr{V}(T) \equiv \lim_{N\to\infty} V_N(T)$ exists. The final state of Q is then $\rho(T) = \mathscr{V}(T)\rho_0\mathscr{V}^+(T)$, and the probability to find the system in $\mathscr{H}_P$ is $\mathscr{P}(T) \equiv \lim_{N\to\infty} P^{(N)}(T) = \mathrm{Tr}[\mathscr{V}(T)\rho_0\mathscr{V}^+(T)]$. By time-reversal invariance $\mathscr{V}^+(T) = \mathscr{V}(-T)$, so that $\mathscr{V}^+(T)\mathscr{V}(T) = P$. This implies that $\mathscr{P}(T) = \mathrm{Tr}[\rho_0\mathscr{V}^+(T)\mathscr{V}(T)] = \mathrm{Tr}[\rho_0 P] = 1$. The equations show that Q is evolving in the subspace $\mathscr{H}_P$, instead of evolving in the total Hilbert space $\mathscr{H}$.

The evolution of Q in Schrodinger equations is transformed to Feynman integral. The propagator from a state $|\Phi\rangle$ to another $|\Psi\rangle$ at the time t_k , when a measurement is carried out, reads $\tilde{G}_k(\Psi, \Delta t; \Phi) = \sum_{\varphi,\phi} K_\varphi^* C_\phi G_k(\varphi, \Delta t; \phi)$, where $\varphi, \phi \in \{0,1\}^N$ are the chosen spin basis, the state $|\Phi\rangle = \sum_\phi C_\phi |\phi\rangle$ and $|\Psi\rangle = \sum_\varphi K_\varphi |\varphi\rangle$. Then we have

$$G_k(\varphi, \Delta t; \phi) \equiv \langle\varphi| E e^{-i\mathcal{H}(t_k)\Delta t} |\phi\rangle = \chi_P(\varphi)\langle\varphi| e^{-i\mathcal{H}(t_k)\Delta t} |\phi\rangle, \tag{A.1}$$

where χ_P is the characteristic function,

$$\chi_P(\varphi) = \begin{cases} 1 & \text{for } |\varphi\rangle \in \mathscr{H}_P \\ 0 & \text{otherwise} \end{cases} . \tag{A.2}$$

For an imaginary time $\tau = i\Delta t$, we get the Green function $\langle\varphi| e^{-i\mathcal{H}(t_k)\Delta t} |\phi\rangle = \langle\varphi| \exp(-\tau\mathcal{H}(t_k)) |\phi\rangle$. So, the propagator for a single 'step' reads

$$W_k(\varphi, \tau; \phi) \equiv G_k(\varphi, -i\tau; \phi) = \chi_P(\varphi)\langle\varphi| \exp(-\tau\mathcal{H}(t_k)) |\phi\rangle. \tag{A.3}$$

The resulting propagator for total time T is $G_N(\varphi_f, T; \varphi_i) = \langle\varphi_f| V_N(T) |\varphi_i\rangle$. For imaginary $\mathscr{T} = iT$, this becomes

$$W_N(\varphi_f,\mathcal{T};\varphi_i)\equiv G_N(\varphi_f,-i\mathcal{T};\varphi_i)$$
$$=\sum_{\varphi_1,\ldots,\varphi_{N-1}} W_{N-1}(\varphi_f,\tau;\varphi_{N-1})\cdots W_0(\varphi_1,\tau;\varphi_i)\chi_E(\varphi_i), \tag{A.4}$$

whose relationship with Wiener integration is manifest. We apply a trick that is often used when one endeavor to relate probability and potential theory [148]. We first rewrite the characteristic function regarding a potential, which is infinite outside $\mathscr{H}_P$, so that the Brownian paths of the Wiener process can never leak out of $\mathscr{H}_P$:

$$\chi_P(\varphi)=\exp(-\tau V_P(\varphi)) \text{ with } V_P(\varphi)=\begin{cases}0 & \text{for } |\varphi\rangle\in\mathscr{H}_P\\ +\infty & \text{otherwise}\end{cases}, \tag{A.5}$$

Hence, the one-step propagator becomes $W_k(\varphi,\tau;\phi)=\langle\varphi|\mathrm{e}^{-\tau V_P}\,\mathrm{e}^{-\tau\mathcal{H}(t_k)}|\phi\rangle$. As $V_P(\varphi)$ is equivalent to $\mathcal{H}_C=\frac{\Delta}{2}\sum_{[i,j]}(1-S_{[i,j]})$ with $\Delta=+\infty$, we can get $W_k(\varphi,\tau;\phi)=\langle\varphi|\mathrm{e}^{-\tau\mathcal{H}_C}\,\mathrm{e}^{-\tau\mathcal{H}(t_k)}|\phi\rangle$, and return to real time

$$G_k(\varphi,\Delta t;\phi)=W_k(\varphi,i\Delta t;\phi)=\langle\varphi|\mathrm{e}^{-i\mathcal{H}_C\Delta t}\,\mathrm{e}^{-i\mathcal{H}(t_k)\Delta t}|\phi\rangle. \tag{A.6}$$

Consider now the limit of continuous observation $N\to\infty$. The limiting propagator reads

$$G(x_f,T;x_i)=\lim_{N\to\infty}G_N(\varphi_f,T;\varphi_i)$$
$$=\lim_{N\to\infty}\langle\varphi_f\,|\,\mathcal{T}\{\prod_{k=0}^{N-1}(\mathrm{e}^{-i\mathcal{H}_C T/N}\,\mathrm{e}^{-i\mathcal{H}(t_k)T/N})\}P|\varphi_i\rangle \tag{A.7}$$

which, by using the Trotter product formula, yields

$$\mathscr{G}(x_f,T;x_i)=\langle\varphi_f|\lim_{N\to\infty}\mathcal{T}\{\prod_{k=0}^{N-1}(\mathrm{e}^{-i(\mathcal{H}(t_k)+\mathcal{H}_C)T/N})\}P|\varphi_i\rangle+O((\frac{T}{N})^2)$$
$$=\langle\varphi_f|\mathscr{V}(T)|\varphi_i\rangle+O((\frac{T}{N})^2), \tag{A.8}$$

where the evolution operator is $\mathscr{V}(T)=\lim_{N\to\infty}\mathcal{T}\{\prod_{k=0}^{N-1}\exp(-i\tilde{\mathcal{H}}(t_k)T/N)\}P$ with $\tilde{\mathcal{H}}(t)=\mathcal{H}(t)+\mathcal{H}_C$.

The above formula shows that the dynamics within Zeno subspace $\mathscr{H}_P$ is governed by the operators $\mathscr{V}(T)$ and $\tilde{\mathcal{H}}(t)$. In the above derivation, we have implicitly assumed the validity of the Trotter product formula. The constraint $\mathcal{H}_C$ which contains four-body interactions is in the

same form of the constraint Hamiltonian as proposed by Lechner *et al.* [178], and it is now generated by repeated projective measurement *P*.

Next, we try to write down the real-time evolution of quantum annealing when considering the tunneling effect. Let $\tilde{\mathcal{H}}(t)=\mathcal{H}(t)+\mathcal{H}_C(t)$, where $t\in[0,T]$. $\{E_j(t)\}$ is the set of eigenvectors of $\mathcal{H}(t)$ and $\{\tilde{E}_m(t)\}$ is the set of eigenvectors of $\tilde{\mathcal{H}}(t)$, in which the subscripts j and m denote the energy levels. $\mathcal{H}(t)=\sum_j \varepsilon_j(t)E_j(t)$, and $\tilde{\mathcal{H}}(t)=\sum_j \tilde{\varepsilon}_j(t)\tilde{E}_j(t)$. The time-evolution operator for $\mathcal{H}(t)$ is written as [201]:

$$U_T(t)\sim A(t)V_T^A(t)\exp[i\sum_{j,k}F_{Tjk}(t)] \tag{A.9}$$

where $V_T^A(t)=\sum_j e^{-i\phi_j(s)}E_j(0)$, $E_j(t)=A(t)E_j(0)A^{\dagger}(t)$, $F_{Tjm}(t)=\int_0^t d\sigma e^{i(\phi_j(\sigma)-\phi_m(\sigma))}K_{jm}^A(\sigma)$, $\phi_j(t)=\int_0^t d\sigma\varepsilon_j(\sigma)$. $K_{jm}^A(t)$ is the matrix element of $K^A(t)$ which is defined by $i\frac{d}{dt}A(t)=K(t)A(t)$. Rewrite the evolution operator as a series of single-time operators:

$$U_T(t)\sim \mathcal{T}\{\prod_{k=0}^{N-1}[A(t_k)V_T^A(t_k)\exp(i\sum_{j,k}F_{Tjk}(t_k))]\}, \tag{A.10}$$

where $A(t)=\mathcal{T}\{\prod_{k=0}^{N-1}(A(t_k))\}$, $V_T^A(t)=\mathcal{T}\{\prod_{k=0}^{N-1}(V_T^A(t_k))\}=\mathcal{T}\{\prod_{k=0}^{N-1}(\sum_j e^{-i\varepsilon_j(t_k)\Delta t}E_j(0))\}$, and

$$\exp(i\sum_{j,m}F_{Tjm}(t))=\mathcal{T}\{\prod_{k=0}^{N-1}\exp(i\sum_{j,m}F_{Tjm}(t_k))\}=\mathcal{T}\{\prod_{k=0}^{N-1}\exp(i\sum_{j,m}e^{i(\phi_j(t_k)-\phi_m(t_k))}K_{jm}^A(t_k)\Delta t)\}.$$

By making repeated measurements *P*, the evolution operator is expressed as

$$\tilde{U}_T(t)\sim \mathcal{T}\{\prod_{k=0}^{N-1}(PA(t_k)V_T^A(t_k)\exp(i\sum_{j,m}F_{Tjm}(t_k))P)\}, \tag{A.11}$$

We define $\tilde{A}(t)=\mathcal{T}\{\prod_{k=0}^{N-1}(PA(t_k)P)\}$, $\tilde{V}_T^A(t)=\mathcal{T}\{\prod_{k=0}^{N-1}(PV_T^A(t_k)P)\}=\mathcal{T}\{\prod_{k=0}^{N-1}(\sum_j e^{-i\tilde{\varepsilon}_j(t_k)\Delta t}\tilde{E}_j(0))\}$

and $\exp(i\sum_{j,m}\tilde{F}_{Tjm}(t))=\mathcal{T}\{\prod_{k=0}^{N-1}(P\exp(i\sum_{j,m}F_{Tjm}(t_k)P)\}=\mathcal{T}\{\prod_{k=0}^{N-1}\exp(i\sum_{j,m}e^{i(\tilde{\phi}_j(t_k)-\tilde{\phi}_m(t_k))}\tilde{K}_{jm}^A(t_k)\Delta t)\}$. It

is noted that the phase $\tilde{\phi}_j(t_k)=\int_0^{t_k} d\sigma\tilde{\varepsilon}_j(\sigma)$ corresponds to the eigenvalues of $\tilde{\mathcal{H}}(t)$ since the initial state is one of the eigenstates of $\tilde{\mathcal{H}}(t)$ and the system would be kept in the space of $\tilde{\mathcal{H}}(t)$ by repeated measurements. $\tilde{U}_T(t) \sim \tilde{A}(t)\tilde{V}_T^A(t)\exp(i\sum_{j,k}\tilde{F}_{Tjk}(t))$ is the real-time operator for $\tilde{\mathcal{H}}(t)$.

It is concluded that repeated projective measurements can be equivalent with a constraint Hamiltonian $\mathcal{H}_C(t)$ applied on the physical spin system and the system will stay in the ground state of the effective Hamiltonian $\tilde{\mathcal{H}}(t)$ if the total annealing time meets the criterion of the validity of adiabatic approximation.

Appendix B
Stochastic process

It is not possible to perform a time evolution on the data qubit array alone without referring to the state of the measure qubits. The data qubits evolve into mixed states which are the average over all possible measurement outcomes. Since the interaction between the data qubits and measure qubits has a simple form and the initial states of measure qubits are defined, one can find some effective evolution equations for the data spins alone. We consider a Markovian process: the evolution of the qubit array is solely determined by its state at present, with no retarded contributions. In the limit of small $\phi \ll 1$, an approximate Lindblad master equation can be written down for the qubit array:

$$\begin{aligned}\frac{\rho'-\rho}{\delta t} &= -\frac{i}{\hbar}[H,\rho]+\frac{1}{2}\sum_n([L_{S_n}\rho, L_{S_n}^\dagger]+[L_{S_n}, \rho L_{S_n}^\dagger]) \\ &+\frac{1}{2}\sum_m([L_{E_m}\rho, L_{E_m}^\dagger]+[L_{E_m}, \rho L_{E_m}^\dagger])\end{aligned} \tag{B.1}$$

where δt is the time between interactions of successive environment qubits, $\rho = \rho(t)$, $\rho' = \rho(t+\delta t)$, L_S and L_E are two separate groups of channels. L_S is a collection of stabilizer channels. From the ancilla measurement protocol, we can get L_S with equal coupling strength determined by ϕ: $L_S = \sqrt{\phi^2/4\delta t}\{S_m^{[i,j]}\}_{m=X,Z}$, where $[i,j]$ is for each plaquette. L_E is a collection of error channels which depend on the chosen error model. For generic balanced depolarizing channels, the error coupling vector for a collection of N data qubits with a per-spin error rate of γ is: $L_E = \sqrt{\gamma/3}\{\sigma_m^{(j)}\}_{m=X,Y,Z}^{j\in[1,N]}$, this corresponds to a per time step error rate of $\gamma\delta t$ for each data qubit.

The Lindblad operator L_S can be obtained with simple calculations. Let $|E_0\rangle$ and $|E_1\rangle$ be the computation basis for a single spin, $|E_0\rangle = [1,0]^T$ and $|E_1\rangle = [0,1]^T$. We have two projective operators $P_0 = |E_0\rangle\langle E_0|$ and $P_1 = |E_1\rangle\langle E_1|$. The unitary evolution in Figure 7.13(a) can be written as $U = U_3U_2U_1$, where:

$$U_1 = (I \otimes I \otimes I \otimes I \otimes R_y(\theta)),$$

$$\begin{aligned} U_2 = & (I \otimes I \otimes I \otimes P_0 \otimes I + I \otimes I \otimes I \otimes P_1 \otimes \sigma_Z) \\ & \cdot (I \otimes I \otimes P_0 \otimes I \otimes I + I \otimes I \otimes P_1 \otimes I \otimes \sigma_Z) \\ & \cdot (I \otimes P_0 \otimes I \otimes I \otimes I + I \otimes P_1 \otimes I \otimes I \otimes \sigma_Z) \\ & \cdot (P_0 \otimes I \otimes I \otimes I \otimes I + P_1 \otimes I \otimes I \otimes I \otimes \sigma_Z) \end{aligned}, \tag{B.2}$$

$$U_3 = (I \otimes I \otimes I \otimes I \otimes R_y(-\frac{\pi}{2})).$$

The evolution operator U can be rewritten as $U = \sum_{i=1}^{4} A_i \otimes B_i$, where

$$\begin{aligned} A_1 &= \cos(\theta/2) \sum_{\{\text{even number of } P_1\}} \otimes_{m=1}^{4} P_m, \quad B_1 = \frac{\sqrt{2}}{2}(I + i\sigma_Y), \\ A_2 &= \cos(\theta/2) \sum_{\{\text{odd number of } P_1\}} \otimes_{m=1}^{4} P_m, \quad B_2 = \frac{\sqrt{2}}{2}(\sigma_Z - \sigma_X), \\ A_3 &= \sin(\theta/2) \sum_{\{\text{even number of } P_1\}} \otimes_{m=1}^{4} P_m, \quad B_3 = \frac{\sqrt{2}}{2}(I - i\sigma_Y), \\ A_4 &= \sin(\theta/2) \sum_{\{\text{odd number of } P_1\}} \otimes_{m=1}^{4} P_m, \quad B_4 = \frac{\sqrt{2}}{2}(-\sigma_Z - \sigma_X), \ P_m \in \{P_0, P_1\}. \end{aligned} \tag{B.3}$$

The state of the system after the unitary transformation is

$$\begin{aligned} \rho_S' &= \mathrm{Tr}_{\text{env}}\{U \left|\Psi\right\rangle\left\langle\Psi\right| U^{\dagger}\} \\ &= \sum_{j,j'} \mathrm{Tr}_{\text{env}}\{(A_j \left|\psi\right\rangle\left\langle\psi\right| A_{j'}^{\dagger}) \otimes (B_j \left|E_0\right\rangle\left\langle E_0\right| B_{j'}^{\dagger})\} \\ &= \sum_{j,j'} A_j \left|\psi\right\rangle\left\langle\psi\right| A_{j'}^{\dagger} \left\langle E_0\right| B_{j'}^{\dagger} B_j \left|E_0\right\rangle. \end{aligned} \tag{B.4}$$

The self-adjoint matrix $M_{jj'} \equiv \langle E_0 \mid B_{j'}^{\dagger} B_j \left|E_0\right\rangle$ has a set of orthonormal eigenvectors $\vec{\mu}_k = \{\mu_{kj}\}$ with real eigenvalues λ_k such that

$$\sum_{j'} M_{jj'} \mu_{kj'} = \lambda_k \mu_{kj} \Rightarrow M_{jj'} = \sum_k \lambda_k \mu_{kj} \mu_{kj'}^{*}. \tag{B.5}$$

We get $\lambda_{1,2} = 0$ and $\lambda_{3,4} = 2$. For non-zero eigenvalues $\lambda_{3,4}$, we have $\vec{\mu}_3 = [0, 0, -1/\sqrt{2}, 1/\sqrt{2}]^T$ and $\vec{\mu}_4 = [1/\sqrt{2}, 1/\sqrt{2}, 0, 0]^T$. We define new operators

$$O_1 \equiv \sqrt{\lambda_3} \sum_j \mu_{3j} A_j = -A_3 + A_4 = -\sin(\theta/2)\sigma_Z \otimes \sigma_Z \otimes \sigma_Z \otimes \sigma_Z,$$

$$O_2 \equiv \sqrt{\lambda_4}\sum_j \mu_{4j} A_j = A_1 + A_2 = \cos(\theta/2) I \otimes I \otimes I \otimes I \,. \tag{B.6}$$

The expression in Eq. (B.4) then simplifies to

$$\begin{aligned} \rho_S' &= \mathrm{Tr}_{\mathrm{env}}\{U|\Psi\rangle\langle\Psi|U^\dagger\} = \sum_{k=1}^{2} O_k |\psi\rangle\langle\psi| O_k^\dagger \\ &= \cos^2(\theta/2)|\psi\rangle\langle\psi| + \sin^2(\theta/2)\sigma_Z^1\sigma_Z^2\sigma_Z^3\sigma_Z^4 |\psi\rangle\langle\psi|\sigma_Z^1\sigma_Z^2\sigma_Z^3\sigma_Z^4 \\ &\approx (1-\theta^2/4)|\psi\rangle\langle\psi| + \theta^2/4\sigma_Z^1\sigma_Z^2\sigma_Z^3\sigma_Z^4 |\psi\rangle\langle\psi|\sigma_Z^1\sigma_Z^2\sigma_Z^3\sigma_Z^4, \end{aligned} \tag{B.7}$$

where the tensor product $\otimes$ is neglected. Let $\rho_0 = |\psi\rangle\langle\psi|$, we then have

$$\frac{\rho_S' - \rho_0}{\delta t} = \frac{1}{2}([L\ \rho_0, L^\dagger] + [L\ , \rho_0 L^\dagger]) \,, \tag{B.8}$$

where

$$L = \sqrt{\frac{\theta^2}{4\delta t}}\sigma_Z^1\sigma_Z^2\sigma_Z^3\sigma_Z^4 \,. \tag{B.9}$$

For the quantum circuits in Figure 7.13(b), we can have

$$L = \sqrt{\frac{\theta^2}{4\delta t}}\sigma_X^1\sigma_X^2\sigma_X^3\sigma_X^4 \,. \tag{B.10}$$